# EXPERIMENTAL INVESTIGATION
# OF
# HETEROGENEOUS COMPRESSIBLE SHEAR LAYERS

Thesis by
Dimitri Papamoschou

In Partial Fulfillment
of the Requirements for the Degree of
Doctor of Philosophy

California Institute of Technology
Pasadena, California

1987

(Submitted 14 November 1986)

Dedicated to my parents

## ACKNOWLEDGMENTS

I am indebted to Professor Anatol Roshko for suggesting and supervising this interesting project. During the course of this research, I have seen him not only as an advisor but also as a friend.

I have had fruitful discussions with many members of the GALCIT faculty, for which I am thankful. I am particularly grateful to the late Professor Lester Lees, as well as Professors Toshi Kubota and Paul Dimotakis for the interest they have shown in the subject, their helpful comments, and the motivation they inspired in me.

The suggestions of Drs. Godfrey Mungal, Mory Gharib, and Jim Hermanson on various aspects of the design of the facility are greatly appreciated. I am thankful for the expert technical assistance of Mr. George Lundgren and the Aero Machine Shop in fabricating the facility. Mr. Marty Gould's exceptional machining skills were instrumental for the timely and accurate construction of the apparatus. Some of the thesis figures display the artistic talents of Mrs. Betty Wood.

Among my fellow graduate students, I would like to thank Greg Smedley and Jeff Hall for their contribution in the making of the centerbodies; Drs. Lorenz Sigurdson and Harry Robey for their help in setting up the microprocessor.

This research project has been supported by a research grant from the Rockwell International Corporation Trust, which we gratefully acknowledge.

Last, but not least, I thank my wife, Quan, for having taken good care of me when I was pretending to work hard.

## ABSTRACT

The compressible, two-dimensional shear layer is investigated experimentally in a novel facility. In this facility, it is possible to flow similar or dissimilar gases of different densities and to select different Mach numbers for each stream over a wide range of Reynolds numbers. In the current experiments, ten combinations of gases and Mach numbers are studied in which the freestream Mach numbers range from 0.2 to 4, the density ratio varies from 0.2 to 9.2, and the velocity ratio varies from 0.13 to 1. The growth of the turbulent region of the layer is measured by means of pitot pressure profiles obtained at several streamwise locations. The resulting growth rate is estimated to be about 80% of the visual growth rate. The transition from laminar to turbulent flow, as well as the structure of the turbulent layer, are observed with Schlieren photographs of 20 nanosecond duration. Streamwise pressure distribution and total pressures are measured by means of a Scanivalve-pressure transducer system.

An underlying objective of this investigation was the definition of a compressibility-effect parameter that correlates and consolidates the experimental results, especially the turbulent growth rates. A brief analytical investigation of the vortex sheet suggests that such a parameter is the Mach number in a frame of reference moving with the phase speed of the disturbance, called here the convective Mach number. In a similar manner, the convective Mach number of a turbulent shear layer is defined as the one seen by an observer moving with the convective velocity of the dominant waves and structures. It happens to have about the same value for each stream. In the current experiments, it ranges from 0 to 1.9.

The correlations of the growth rate with convective Mach number fall approximately onto one curve when the growth rate is normalized by its incompressible value at the same velocity and density ratios. The normalized growth rate, which is unity for incompressible flow, decreases gradually with increasing convective Mach number, reaching an asymptotic value of about 0.25 for supersonic convective Mach numbers. The above behavior is in qualitative agreement with results of linear stability theory as well as with those of previous, one-stream experiments.

Large-scale structures, resembling those observed in subsonic shear layers, are evident in the Schlieren photographs. It is estimated that the mean structure spacing, normalized by the local thickness, is reduced to about half its incompressible value as the convective Mach number becomes supersonic.

An estimate of the transition Reynolds number has been obtained from the photographs of two shear layers having quite different convective Mach numbers, one low subsonic and the other sonic. In both cases, it is about $2 \times 10^5$, based on distance to transition and properties of the high unit Reynolds number stream, thus suggesting that, in this experiment, transition is dominated by instabilities of the wake, rather than of the shear layer.

TABLE OF CONTENTS

# LIST OF FIGURES

# LIST OF TABLES

# LIST OF SYMBOLS

| Symbol | Description |
|---|---|
| $a$ | Sound speed |
| $c$ | Disturbance wave speed, $c = c_r + ic_i$ |
| $\bar{c}_i$ | Normalized $c_i$, $\frac{c_i}{U_1-U_2}$ |
| $\bar{c}_r$ | Normalized $c_r$, $\frac{c_r-U_2}{U_1-U_2}$ |
| $h$ | Nozzle exit height |
| $h^*$ | Nozzle throat height |
| $\ell$ | Mean structure spacing |
| $M$ | Mach number |
| $M_c$ | Convective Mach number, defined in Eqs. (4.11), (4.28), (4.30), and (4.31) |
| $M_c^*$ | Critical convective Mach number, Section 4.1.1 |
| $M_e$ | Mach number at nozzle exit |
| $p$ | Static pressure |
| $p_t$ | Total pressure |
| $p'_t$ | Pitot pressure |
| $r$ | Velocity ratio, $\frac{U_2}{U_1}$ |
| $R$ | Gas Constant |
| $Re_t$ | Boundary layer transition Reynolds number based on axial distance |
| $Re_{x_{tr}}$ | Shear layer transition Reynolds number, $\frac{Ux_{tr}}{\nu}$ |
| $Re_\theta$ | Reynolds number, $\frac{U\theta}{\nu}$ |
| $Re'$ | Unit Reynolds number, $\frac{U}{\nu}$ |

| | |
|---|---|
| s | Density ratio. $\frac{\rho_2}{\rho_1}$: |
| | Entropy, Section 3.3.3 |
| t | Time |
| T | Static Temperature |
| $T_t$ | Total Temperature |
| u | Local mean streamwise velocity |
| U | Freestream Velocity |
| x | Streamwise coordinate, Figure 1.1 |
| $x_{tr}$ | Distance to transition, from trailing edge |
| $x_{gr}$ | Distance to first turbulent-growth datum, from trailing edge (Section 3.2.2) |

Greek Letters

| | |
|---|---|
| $\alpha$ | Disturbance wave number, $\alpha = \alpha_r + i\alpha_i$ |
| $\beta$ | Propagation angle of oblique disturbance |
| $\gamma$ | Ratio of specific heats |
| $\delta$ | Shear-layer thickness (unspecified); |
| | Boundary-layer velocity thickness, Section 3.2.2 |
| $\delta'$ | $d\delta/dx$ |
| $\delta^*$ | Boundary-layer / Shear-layer displacement thickness |
| $\delta_{pit}$ | Shear-layer pitot thickness, defined on Figure 2.10 |
| $\delta_{vis}$ | Shear layer visual thickness |
| $\delta_\omega$ | Shear layer vorticity thickness |
| $\eta$ | Similarity variable, y/x |
| $\theta$ | Boundary layer momentun thickness |
| $\mu$ | "Complex" convective Mach number, Eq.(4.9) |
| $\nu$ | Kinematic viscosity |
| $\rho$ | Density |
| $\tau$ | Shear Stress |
| $\phi$ | Velocity potential |
| $\psi$ | Disturbance amplitude function, Eq.(4.6) |
| $\omega$ | Frequency of disturbance |

Subscripts

| | |
|---|---|
| 0 | Incompressible value at same velocity and density ratios |
| 1 | High-speed stream conditions |
| 2 | Low-speed stream conditions |
| $\infty$ | Boundary-layer freestream conditions |
| e | Nozzle exit conditions |
| j | 1,2 |

# Chapter 1
# Introduction

## 1.1. Motivation.

As a result of today's increasing importance of supersonic combustion, there has recently been renewed interest in the compressible turbulent shear layer. Compressibility plays a crucial role in the stability and mixing of shear layers, its effects being capable of producing order-of-magnitude changes compared to incompressible shear layers. It is essential that these effects be understood in a coherent and universal way. The limited amount of experimental data in two-stream, compressible turbulent shear layers dictates an extensive experimental investigation where a parametric study of such flows can be carried out.

It has been observed that turbulent shear layers with one stream supersonic and one stream at rest (e.g., at the edges of jets) spread more slowly than incompressible shear layers. Birch and Eggers [1972] have compiled a survey of such experiments. Although some inconsistencies exist among the various experimental investigators, there is a definite trend of decreasing growth rate with increasing freestream Mach number. In most one-stream experiments, increasing Mach number is accompanied by decreasing temperature and thus increasing density of the jet. The thinning of the shear layer with increasing Mach number was thus attributed by many investigators to the density ratio between the jet and the external gas. This led to models incorporating Howarth-Dorodnitsyn-type transformations, density-dependent eddy viscosities, etc.

Whether density effects alone could account for the differences in spreading rate was one of the questions that motivated the experiment of Brown and Roshko [1974], who built an apparatus in which

incompressible shear layers with large density differences could be studied by using different gas combinations, like helium and nitrogen, at low speeds. It was found that, although there is some effect of density on the spreading rate, it is very much smaller than what is observed in the supersonic case. It was therefore concluded that compressibility, per se, plays an important role in the development of the supersonic shear layer.

Little information about turbulent growth rates can be extracted from the scarce, two-stream experiments found in the literature, primarily because most measurements were taken in the near field of a flow with a strong wake component (Bailey and Kuethe [1957]). Ortwerth and Shine [1977] conducted an interesting heterogeneous experiment, mentioned later in this section, but provided unclear growth-rate data. Recently, Chinzei et al. [1986] conducted a rather extensive investigation of turbulent shear layers, with air in both streams, where one Mach number is supersonic and the other ranges from subsonic to supersonic. Their growth rate measurements, however, are hard to interpret quantitatively because they are based on an uncommon definition of shear-layer thickness and are correlated ignoring density effects. Other two-stream experiments concentrate on transition (Shackleford et al. [1973], Demetriades and Brower [1982]) and ejector performance (Dutton et al. [1982]).

In recent years, supersonic stability and mixing have found the rather unlikely application in understanding the behavior of cosmic jets emanating from the nuclei of galaxies. Astrophysicists believe that cosmic jets are supersonic and that, as a result, their morphology and small spreading angle could be partly due to Mach-number effects (Blandford et al. [1982]). Considerable computational effort has been expended to simulate the fluid-mechanical properties of such jets, an example being the work of Norman and Winkler [1983].

An important elementary feature that distinguishes a supersonic flow from a subsonic one is that in the supersonic case a disturbance does not propagate upstream, while in the subsonic case a disturbance is felt throughout the flowfield. Given the limited region of influence of a supersonic disturbance, we might expect that a supersonic shear layer is more stable, therefore mixes more slowly, than a subsonic one. In trying to convert this abstract notion to a more concrete one, we come to the following obvious question: in what frame of reference do we measure the compressibility of the shear layer? In the case of the one-stream shear layer, we might choose the laboratory frame of reference. In the case of the two-stream shear layer, however, this becomes a very poor choice. As an extreme example, we consider a shear layer comprised of two supersonic streams with nearly equal velocities. Clearly, it would be a mistake to describe such a shear layer as intrinsically supersonic, when the velocity difference between the freestreams is low subsonic. The problem of finding the proper frame of reference becomes even more complex when the gases have different speeds of sound. Nevertheless, it is essential that a sensible choice for a frame of reference is made in which the intrinsic compressibility of the flow can most adequately be characterized.

In two-stream compressible shear layers, the effects of compressibility are coupled not only with the effects of density ratio, but also with those of velocity ratio. These two parameters have been found to play a fundamental role in the growth of fully-developed, turbulent incompressible shear layers. In order to understand and quantify the effects of compressibility, a scheme must be invented where the compressibility effects are somehow uncoupled from those of the other important parameters. Useful comparisons can only be made when one parameter is varied at a time, something that is lacking in the correlations done by previous experimental investigators.

It has been observed, initially by Brown and Roshko, that subsonic turbulent shear layers contain large, so-called "coherent" structures reminiscent of those in the early stages if instability. It was realized that the growth of the shear layer is governed primarily by its instability at these large scales. It would be interesting to find out whether such large structures dominate the development of compressible shear layers. There is already visual evidence that large-scale structures exist in supersonic shear layers. This evidence comes from the experiments of Ortwerth and Shine [1977], where a stream of helium at M=3 mixes with a stream of nitrogen also at M=3, and Oertel [1979] at the edges of supersonic jets.

Another interesting aspect of compressible shear layers is the transition from laminar to turbulent flow. We might expect that, since compressibility apparently stabilizes the flow, transition is delayed as compressibility increases. The extensive transition investigation of Chapman et al. [1948] indicates that such a trend exists in reattaching shear layers. It would be incorrect, however, to simply extend these results to the free shear layer without taking into account the stabilizing influence of the reattachment process. Unfortunately, there are virtually no transition experiments in compressible, one-stream, free shear layers. In the two-stream case, transition may be wake-dominated, in which case the compressibility of the wake may be more important than that of the far-field shear layer. The related investigations of Shackleford et al. [1973] and Demetriades and Brower [1983] tend to support that premise. The dependence of transition on the intrinsic compressibility of the flow is a subject worth pursuing further.

Some insights into the effects of compressibility on the development of the turbulent shear layer can be gained by carrying out the inviscid, linear stability analysis of shear layers with typical velocity and density profiles, the simplest case being the vortex sheet. The results of such analyses cannot, of course, be directly applied to

the turbulent problem, but they provide tools and intuition which are very useful for understanding more complex problems.

## 1.2. Research Program Objectives.

The objective of this study was to investigate planar, two-stream shear layers between similar or dissimilar gases at a variety of freestream Mach numbers, ranging from subsonic to high supersonic. In that way, compressibility effects, together with those of density and velocity ratios, could be studied. Additionally, it was desired to have variable test section static pressure, offering a range of Reynolds numbers, from those associated with transitional flow to those associated with fully turbulent flow. The general configuration of the shear layer and the variables involved are summarized in Figure 1.1.

A new and unique facility was necessary to meet the experimental specifications mentioned above. Its design and construction proved to a formidable task, the generation and instrumentation of a shear layer composed of two independent supersonic streams presenting many complex problems. Nevertheless, the facility was completed in sufficiently short time that a fair number of experiments was conducted within the duration of this project.

This investigation focuses primarily on the measurement of turbulent growth rates from pitot pressure surveys. Such measurements are performed at 10 Mach number-gas combinations with varying degrees of compressibility, so that statistically meaningful trends are established. An attempt is made to correlate and unify the results, using ideas stated earlier in this chapter, so that the net effect of compressibility can be abstracted as clearly as possible.

The laminar-to-turbulent transition and structure of the turbulent layer are observed with instantaneous Schlieren photography. From the photographs, some rather subjective estimates of transition Reynolds

numbers and large-scale structure spacings are obtained.

Other aspects of the flow, such as streamwise pressure gradient, velocity profiles, and growth of a wake flow are briefly investigated.

# Chapter 2
# Experimental Details

## 2.1. General Description.

A new facility was designed and built in which a two-dimensional, compressible shear layer can be established at a variety of Mach numbers, Reynolds numbers, density ratios and velocity ratios. The flow apparatus is essentially a two-stream, blow-down supersonic wind tunnel with two independent supply sides. Each supply side is connected to high-pressure gas cylinders. Similar or dissimilar gases can be used to generate the shear layer. After being expanded to their design Mach numbers, the two gases are brought into contact downstream of a splitter plate and mix inside a rectangular test section. Glass windows, mounted on the test section sidewalls, allow for visual observation of the layer. The downstream end of the apparatus is connected to a low pressure tank which is evacuated by a vacuum pump. A schematic overview and photographs of the facility are shown on Figures 2.1 and 2.2.

Instantaneous Schlieren photography is used to visualize the structure of the turbulent layer as well as the laminar-to-turbulent transition region. Pitot pressure profiles, obtained by a traversing pitot probe, are used to measure the thickness of the layer at several streamwise locations. Each Schlieren photograph and thickness measurement is accompanied by a record of total pressures, total temperatures and sidewall static pressure distribution. The experiment is microprocessor controlled, which allows for the execution and proper timing of several functions within the short duration of each run. The operation of the facility is intermittent, each run lasting typically 1.5 to 2 seconds.

## 2.2. Flow Apparatus.

The flow apparatus can be divided into two sections: the high pressure section and the low pressure section. The high pressure section consists of the gas supply system and the settling chamber. The low pressure section consists of the test section, where the shear layer is formed, the low pressure tank and the vacuum pump. The settling chamber and test section, which together form the "main apparatus", are contained in a 3 ft long, clamp-like structure which forms the top and bottom outside walls of the main apparatus. The main apparatus sits on rails along which it can traverse forward or backward along the flow direction. The usefulness of this feature will be discussed in section 2.3.1. The detailed design of the flow apparatus is shown on Figure 2.1. All its structural components are machined from aluminum 7075 and are bolted to each other, allowing for quick assembly and disassembly.

2.2.1. High-Pressure Section. Two identical but independent supply lines feed gas into each of the two separate compartments of the settling chamber. Each supply line is connected to a manifold of 5 gas cylinders, each cylinder containing 200 standard cubic feet of gas at a pressure of 2000 psig when fully loaded. The manifold is connected, through a 3/4 in. diameter carbon steel tube, to a dome-loaded, high-capacity pressure regulator (Grove Model 202G). The regulator reduces the gas pressure to a value ranging from 10 psia to 100 psia. Downstream of the pressure regulator, a solenoid valve (ASCO) is used to start and stop the flow. The gas is fed into the settling chamber compartment by means of two 3/4-in. diameter flexible metal hoses. The use of flexible hoses permits the movement of the main apparatus along its rails.

The settling chamber has two separate compartments of identical design. Each compartment consists of a gas inlet, a constant area section with flow management devices and a contraction section. The length and width of the entire settling chamber are 12 in. (305 mm) and

2.25 in. (57 mm) respectively. The height of each compartment at the constant area section is 2 in. (51 mm). The two compartments are separated by a 0.4 in. (10 mm)-thick divider plate. The structural design allows for a maximum pressure differential of 150 psi between compartments and a maximum pressure of 150 psig for the whole settling chamber.

The gas inlet is designed so that the flow entering each compartment develops a uniform, rather than a jet-like, velocity profile. That design is shown on Figure 2.3. The two flexible hoses, which supply the gas, are attached to the ends of a manifold-type structure, which forms the upstream end-plate of the compartment. The manifold has 25 outlets, of 0.2 in. (5.1 mm) diameter, evenly spaced across the end-plate and oriented in the downstream direction. The flow discharges into the compartment through each outlet, thus acquiring a approximately uniform velocity profile.

Inside the 7-in. (178 mm) long constant area section of each compartment, a series of flow management devices help smooth out the velocity profile into a uniform one. Immediately downstream of the gas inlet there are two perforated plates of 0.1 in. (2.5 mm) hole diameter and 40% solidity. They are followed by a 3-in. (76 mm) long piece of honeycomb with 0.08-in. (2.0 mm) mesh size. Downstream of the honeycomb there are two wire screens with 0.02-in. (0.5 mm) mesh size and 38.5% solidity. The dimensions and spacings of the above devices are a result of compromise between physical constraints and suggestions in Loherke and Nagib [1972], as well as private consultations with Dr. Morteza Gharib.

In the design of the contraction section, care was taken to avoid flow separation that might result from a small length-to-height ratio. The contraction has a length-to-height ratio of 2.5, which is considered to be quite safe in that respect (Chmielewski [1974]). The shape of the contraction is a fifth-order polynomial, with the first

and second derivatives vanishing at the extremes. It is claimed by Tan-atichat et al. [1980] that such a shape is superior to others in maintaining a uniform velocity profile all the way to the contraction exit.

An important feature of the settling chamber design is the ability of its upper and lower walls to slightly deflect about flexure joints located at the upstream end of the chamber. Each wall is cantilevered near the flexure joint and can be deflected inwards or outwards by means of a screw mechanism mounted on the structure that contains the settling chamber and test section. Although the deflection angles are very small -less than 0.5 degrees- they can significantly change the throat height of the supersonic nozzles. It will be seen in section 2.2.3 that this is very useful for the proper installation of the supersonic nozzles.

Sealing of the settling chamber from the ambient surroundings, as well as sealing of each compartment from the other, is accomplished by rubber O-rings, placed in grooves that run along every contact surface between components.

2.2.2. Low-Pressure Section. The most important part of the apparatus is the test section (Figure 2.1), where the shear layer is formed. At the upstream end of the test section, a removable centerbody, placed between the upper and lower test section walls, forms two supersonic nozzles. The centerbody ends in a sharp trailing edge. The downstream end of the test section forms a supersonic diffuser that is connected to a low-pressure tank. Optical quality glass windows extend from upstream of the centerbody tip all the way to the diffuser. The windows are mounted on removable sidewalls that provide access to the test section. The upper and lower test section walls can each be deflected inwards or outwards. A detailed description of the test section follows below.

In designing the various test section components, special effort was made to avoid protrusions or extrusions in joints between components, particularly where the flow is supersonic. As is well known, in supersonic flow such disturbances travel unattenuated for long distances, causing undesirable effects. As a result, the design of the supersonic part of the test section is such that no joints exist perpendicular to the flow direction.

In contemplating the design of a nozzle combination that would produce two streams at independent Mach numbers, two arrangements were considered: one where a thin, wedge-shaped splitter plate is placed between two nozzle contours; and one where a contoured centerbody is placed between two parallel walls. The latter arrangement was preferred because it is structurally sounder than the former, although the former provides more flexibility when more than two interchangeable nozzle contours are used.

The upstream part of the centerbody becomes a smooth continuation of the settling chamber divider plate, as can be seen in Figure 2.F3. It is joined with the divider plate by means of an insert. The joint is located one third of the way into the subsonic contraction. The centerbody has its maximum thickness right at the end of the contraction, where the two nozzle throats are formed. The downstream part of the centerbody forms two supersonic nozzles with equal exit heights of 0.45 in. (11.4 mm). The length of the subsonic part of the centerbody, from upstream joint to throat, is 3.2 in. (81 mm). The length of the supersonic part, from throat to tip, varies from 1.96 in. (50 mm) to 2.27 in. (58 mm), depending on the combination of Mach numbers. The tip thickness is typically 0.02 in. (0.5 mm). The centerbody width is 2.25 in. (57 mm) and its upstream thickness, where it joins the divider plate, is 0.4 in. (10 mm). The transition from the 0.4 in. thickness to the maximum thickness at the throats is accomplished by fifth-order polynomials curves.

A 1/4 in. diameter hole is drilled across the whole width of the centerbody, 1.2 in. (30 mm) upstream of the throat, and is aligned with equal diameter holes drilled through the settling chamber sidewalls. When the centerbody is in place, structural support is provided by a pin driven through the centerbody and sidewalls. Once access to the test section is gained, the centerbody can be removed simply by pulling out the pin. The sides of the centerbody are covered with RTV silicone rubber, which forms thin gaskets that seal the centerbody against the sidewalls. Details about the design, construction and use of the centerbodies are given in section 2.2.3.

The rectangular test section is 9 in. (230 mm) long, 2.25 in. (57 mm) wide and its height at the nozzle exits is 0.9 in. (23 mm). The aspect ratio of each nozzle exit is thus 5.0. The top and bottom walls can each be deflected about 1.2 in. (30 mm) long flexure areas located 3.2 in. (81 mm) downstream of the nozzle throats, or 0.8 in. (20 mm) downstream of the edge of the longest centerbody used here. Each wall can deflect outwards or inwards a maximum of 5 degrees. The deflections are controlled by screw mechanisms, similar to those that control the throat heights. The sidewall deflections were intended to compensate for possible boundary layer and shear layer displacement thickness effects. Along each wall there are 16 equally spaced static pressure taps, of 1/32 in. (0.8 mm) diameter each. The distances of the upstream-most and downstream-most pressure taps from the nozzle throats are 1.05 in. (27 mm) and 8.55 in. (217 mm) respectively. The longitudinal spacing of the pressure taps is 0.5 in. (13 mm) and they are arranged as shown on Figure 2.4

The sidewalls of the test section are removable, providing access to the full length of the test section. A photograph of the exposed test section is shown on Figure 2.5. Long rectangular glass windows are mounted on the sidewalls and provide a view of the whole test section. Each window's length, height, and thickness are 14 in. (356 mm), 1.5 in. (38 mm) and 0.5 in. (12.7 mm) respectively. The windows are

made of optical quality BK-7 glass. They extend from 0.8 in. (20 mm) upstream of the nozzle throat all the way to the diffuser section. The upstream joint of the window with the aluminum frame is therefore located well upstream of the sonic throats, satisfying the design objective stated at the end of Section 2.2.2.

With the facility in operation, the test section is surrounded by gas at low pressure, estimated to be within 0.5 psia of the test section static pressure. This minimizes the possible leakage of gas in or out of the test section through the very small gap between the unsealed deflectable walls and the sidewalls. Based on the design width of that gap, the maximum possible leakage across the entire test section is estimated to be of the order of 0.1% of the test section volumetric flow rate.

At the downstream end of the test section, a wedge-shaped diffuser is used to decelerate the flow into an area 2.4 in. (61 mm) by 2.25 in. (57 mm). The diffuser is 2 in. (51 mm) long, with its upstream end rounded-off and slightly protruding in the flow. The two wedges, one on the upper and one on the lower wall, are removable. With the wedges removed, the diffuser takes the shape of a backward-facing step. Removal of the wedges did not significantly alter the diffuser performance. The wedges are removed when the traversing pitot probe is installed.

The downstream end of the apparatus is connected to the low pressure tank by means of a 2-in. diameter, 5-ft long flexible metal hose. That hose, together with the flexible hoses connected to the settling chamber, allow the movement of the apparatus along its rails.

The low pressure tank has an approximate volume of 200 $ft^3$ (5.5 $m^3$). It is connected to a large capacity rotary piston vacuum pump ( Beech-Russ 325RP ) that displaces 325 $ft^3$/min. The tank and pump were parts of the now abandoned GALCIT Arc Tunnel Facility. The recommissioning of the vacuum pump, which had be sitting idle for many years,

required the refurbishment of some parts and the installation of a new electrical system. The tank was slightly modified to be adapted to the facility.

The size of the tank and vacuum pump proved to be quite satisfactory for the operation of the facility, providing run times as long as 5 seconds and pump-down times of less than 3 minutes. The tank can be evacuated to pressures as low as 5 mm Hg, although such low pressures were not necessary for the experiments.

2.2.3. Centerbody Details. It was desired to design the centerbody supersonic nozzle contours such that the flow at the nozzle exit is expanded to a uniform parallel jet, free of waves of significant strength. The contours can be designed graphically using the method of characteristics, assuming uniform flow at the throat. This method is laborious and its accuracy depends on the number of characteristics and the skill and patience of the designer. Foelsch [1946] has proposed an elegant method by which the nozzle contours are computed analytically. His method applies the method of characteristics to a flow originating from a line source upstream of the nozzle throat. The expansion region of the nozzle is a circular arc, whose radius and final angle are chosen by the designer. The coordinates of the cancellation region are given by analytical expressions. Given the parameters of the circular expansion region, a unique shape for the cancellation region is computed for each exit Mach number and specific heat ratio. The Foelsch method is briefly described in Appendix A.

Because of its relative simplicity, the Foelsch method was applied to the design of the centerbodies used here. Ideally, it is good practice to apply a boundary layer displacement thickness correction to the nozzle contours. Such a correction would strictly be valid only at a given Reynolds number, at which the boundary layer thickness distribution is somehow known. It was anticipated that the nozzles designed here would be used at a wide range of Reynolds numbers, thus making a

single boundary layer correction impossible. That, coupled with imperfections in the manufacturing of the centerbodies, led to the belief that a boundary layer correction would be rather pointless. As a result, no such correction was given to the nozzle contours. The correctness and implications of this decision are discussed in Section 3.2.2. where nozzle boundary layer is calculated at Reynolds numbers that typically occurred in the experiments.

A computer program, written on C.I.T.'s Computer Support Services VAX 11/780 computer, generates the centerbody coordinates, given the parameters of the expansion region, the exit Mach numbers and the specific heat ratios.

The centerbodies were made of aluminum 7075 and were machined on a numerically controlled (N.C.) mill (Servo Products Model 6000) of C.I.T.'s Engineering and Applied Science Division. The centerbody coordinates were computed on C.I.T.'s VAX 11/780 computer and fed into the memory of the N.C. mill. Because of the unusual geometry of the centerbodies, an elaborate support system was built that enabled the machining and protected the centerbody tip from being bent by the cutting tool. Despite the automation, the machining was very slow and hampered by repeated breakdowns of the mill and the computer. Due to the small size of the mill's memory, only a limited number of coordinates could be input, resulting in a coarse surface on the final product. The surfaces were later sanded by hand to a smooth finish. The tolerance of the whole fabrication process is estimated to be about 0.005 in. (0.12 mm).

Each centerbody is easily installed by attaching it to the settling chamber divider plate and by inserting the support pin described in Section 2.2.2. Using filler gauges and by slightly deflecting the settling chamber sidewalls, the correct nozzle heights, corresponding to each centerbody, are set to within 0.002 in. (0.05 mm).

Three centerbodies, each with a unique exit Mach number, $M_e$, and specific heat ratio, $\gamma$, combination were designed and fabricated. Their designs are shown on Figure 2.6. In Figure 2.7, pitot pressure profiles, obtained at the exits of the nozzles formed by the centerbodies, indicate that the Foelsch design is quite adequate in producing nearly uniform exit conditions.

The specifications of the centerbodies are listed in Table 2.1 below. The nozzle exit heights are 0.45 in. (11.4 mm). The throat heights, $h^*$, and throat to trailing-edge lengths, L, are also listed in the table.

Table 2.1. Centerbody Design Conditions

| | Side 1 | | | Side 2 | | | |
|---|---|---|---|---|---|---|---|
| Centerbody | $M_e$ | $\gamma$ | $h^*$(in.) | $M_e$ | $\gamma$ | $h^*$(in.) | L(in.) |
| I | 3.0 | 7/5 | 0.105 | 3.0 | 5/3 | 0.148 | 1.96 |
| II | 3.5 | 7/5 | 0.065 | 2.3 | 5/3 | 0.238 | 2.39 |
| III | 4.0 | 5/3 | 0.081 | 1.9 | 7/5 | 0.286 | 2.27 |

The above centerbodies are used with three of the most common, inexpensive and safe gases: helium ($\gamma$=5/3), argon ($\gamma$=5/3) and nitrogen ($\gamma$=7/5). Any other gases with the above specific heat ratios are either too expensive (like xenon) or too dangerous (like hydrogen) to use. A mixture of gases with the same $\gamma$, like He and Ar, could be used if the facility had provisions for such operation. In the current experiments, only unmixed gases are used, providing a fair number of Mach number-gas combinations.

It was tempting to employ the above centerbodies at slightly off-design conditions by using monatomic gases where diatomic gases are supposed to be used and vice-versa. That adds a couple more Mach number-gas combinations to the ones obtained at the design conditions without the time-consuming fabrication of a new centerbody. The geometry of the centerbody remains unchanged, that is, the throat heights remain at the design conditions. Since the nozzle area ratio stays constant, the change of $\gamma$ creates a different exit Mach number. A calculation of the nozzle contour at the new condition showed that the slope differs only a maximum of 1 degree from the existing contour for the cases listed in Table 2.2 below:

Table 2.2. Centerbody Slightly Off-Design Conditions

| | Side 1 | | Side 2 | |
|---|---|---|---|---|
| Centerbody | $M_e$ | $\gamma$ | $M_e$ | $\gamma$ |
| III | 4.0 | 5/3 | 2.0 | 5/3 |
| III | 3.3 | 7/5 | 1.9 | 7/5 |

Additionally, centerbody III is used for supersonic/subsonic combinations, with its low Mach number side becoming a slowly diverging subsonic channel.

## 2.3. Diagnostics.

2.3.1. Flow Visualization. Flow visualization is used to detect the large-scale structures of the shear layer and to estimate the location of the laminar to turbulent transition region. It is accomplished by a spark-illuminated Schlieren system designed for high sensitivity and very short exposure time. A schematic of the Schlieren system is

shown on Figure 2.8

The system is a conventional one, with a horizontal knife edge and a folded configuration due to lack of space in the laboratory. All its components lie on a horizontal plane and are attached on a steel plate-covered table by means of magnetic mounts. The Schlieren heads are 3.93 in. (100 mm) diameter, f10 spherical mirrors (Melles Griot). A combination of flat mirrors folds the light path as shown on Figure 2.8. All mirrors in the system are figured to one tenth of wavelength of visible light.

The spark source (Xenon Corp. Model N-789B "Nanolamp" with Model 437 power supply) is of unique design, originally invented by Fischer [1961]. Its high capacitance - low inductance characteristics allow it to produce sparks of approximately 20 nanosecond duration. The very short spark duration enables the instantaneous visualization ("freezing") of flow structures whose scale is of the order of millimeters and whose velocity is of the order of 1000 m/s. The spark brightness is lower than that of other, longer duration sparks but high enough to produce good quality photographs on high speed film. The film used here is 35 mm Kodak Tri-X Pan. Its ASA rating is 400 but can be increased to 1000 by developing the film with diafine.

The design of the Schlieren light source is critical in obtaining adequate brightness and high sensitivity. High sensitivity is necessary because the test section pressures, and hence refractive indices, are very low. The source consists of the spark, condenser and optical slit. The smaller the slit width, the higher the sensitivity becomes. The slit used here (Edmund Scientific) has adjustable width that ranges from 0.005 in. (0.13 mm) to 0.08 in. (2.0 mm) although only a range from 0.005 in. to 0.010 in. was actually used. Given the small slit width and the limited brightness of the spark, the proper focusing of the spark on the slit becomes very important. Since the spark is a point source, it is desirable to capture its light in the greatest

possible solid angle. For that, a large diameter, small f-number condenser should ideally be used. Such a condenser, however, produces high spherical aberration that smears the focal area and thus decreases the brightness at the slit. Therefore, the f-number of the condenser should not be too small. After many trials, the selected configuration is a two-element, 2.75 in. diameter, f2.25 condenser.

The small width of the optical slit, together with the large focal length of the schlieren heads, produce a system with enough sensitivity to allow visualization of most flows generated here. The sensitivity can be varied by adjusting the slit width and the amount of knife edge insertion in the source image plane. Due to the small refractive index gradients encountered here, visualization was possible only with the slit and knife edge both parallel to the shear layer. Visualization was best when the refractive index difference was large and the shear layer spreading rate small.

A continuous light source, that consists of a 100-Watt Tungsten -Halogen lamp (Oriel Model 6322), is used for continuous flow observations and helps in the alignement of the optical components. A sliding mirror offers the choice of continuous or instantaneous illumination without necessitating the removal or relocation of either light source.

The parallel light beam that enters the test section covers 4 in.es (100 mm) of streamwise length. In order to enable visualization of all parts of the 9 in. long test section, the apparatus traverses on rails, while the optical system remains stationary. As mentioned previously, the flexible connections of the main apparatus to the other systems make the traversing motion possible. Usually two photographs, with an overlap of 0.5 in. (unless otherwise stated), are enough to visualize most of the test section.

2.3.2. Pitot Probe. A pitot probe that traverses the shear layer at selected streamwise locations was designed and constructed. The probe provides pitot pressure profiles from which the shear layer thicknesses and growth rates are measured. The design of the probe and traversing mechanism reflects the need for a device small enough not to cause flow choking problems and simple enough to require only minor apparatus modifications for its installation. Additionally, the probe was designed to provide good spatial resolution and short time response. A sketch of the probe and traversing mechanism is shown on Figure 2.9. A photograph of the probe, installed in the test section, can also be seen on Figure 2.5.

The probe consists of a 0.083 in. (2.1 mm) diameter, 8 in. (203 mm) long stainless steel tube, flattened at the end to an opening 0.005 in. (.13 mm) by 0.10 in. (2.5 mm). A typical shear layer thickness being 5 mm, the probe offers an adequate spatial resolution. The probe is rigidly mounted inside a larger, 1/8 in. diameter tube, which provides its structural support. The supporting tube pivots and translates longitudinally about a point 2 in. (51 mm) downstream of the test section end (the diffuser wedges are removed). The motorized pivoting motion enables the tip of the probe to move laterally across the test section at a nearly constant speed. The longitudinal translation, which is done manually, allows the positioning of the probe tip anywhere along the test section. The maximum possible incidence angle of the probe with the flow is 10 degrees. This angle is considered small enough not to affect the accuracy of the pressure measurement (Liepmann and Roshko [1957]). The downstream end of the probe is connected, via flexible tubing, to a pressure transducer (Setra Systems Model 204), located outside the apparatus.

The pivot mechanism consists of a 9-in. (230 mm) long moment arm, extending to the downstream end of the apparatus. Directly above the tip of the moment arm and located outside the apparatus there is a A.C., 27.2 RPM, reversible motor (Bodine NYC-12RS3). A cable that

passes through the apparatus wall links the tip of the moment arm to the motor shaft. The cable slides through a teflon seal that minimizes the leaking of ambient air into the apparatus. As the motor turns clockwise, the cable winds on the motor shaft and the probe traverses downwards. The probe returns to its resting position, against the upper test section wall, by the action of a spring and by turning the motor counter-clockwise. The motor shaft has three consecutive segments of 0.25, 0.375, and 0.50-in. diameters, on each of which the cable can be attached. Since the motor RPM is fixed, the traversing speed of the probe tip is a known function of longitudinal position and motor shaft diameter. The shaft diameter is selected so that the traversing time across the shear layer is about 1.5 seconds, a typical traversing speed being 10 mm/s. The response time of the probe-transducer system, of the order of 10 ms, is small enough to permit this kind of operation. To ascertain good temporal resolution, the probe was occasionally traversed in the opposite direction and the signal obtained was identical to the original one.

Two mechanically programmed electrical switches, linked to the probe motion via the motor, are located outside the apparatus. They provide coordination of the probe motion with other functions of the facility and shut-off the motor before the probe touches the lower test section wall. That coordination will be further described in section 2.4.

Given a monotonic pitot-pressure profile, the shear layer pitot thickness is obtained by measuring the profile width, from $p_{t_2}' + 0.05\ \Delta p_t'$ to $p_{t_2}' + 0.95\ \Delta p_t'$ (5% to 95% width), as shown on Figure 2.10(a). If the profile is not monotonic, that is if a local minimum occurs, the profile width is measured from $0.95\ \Delta p_{t_1}'$ to $0.95\ \Delta p_{t_2}'$, with $\Delta p_{t_1}'$ and $\Delta p_{t_2}'$ defined on Figure 2.10(b). The occurrence of a minimum does not necessarily imply a wake effect and could be a result of the mixing

between dissimilar gases, as will be discussed in Section 3.2.3. Examples of actual pitot thickness measurements in present cases where the pitot-pressure profile is monotonic or has a deficit are shown on Figure 2.11. The case designation will be introduced in Section 2.7. It is estimated that the pitot thickness obtained by the above method is about 80% of the corresponding visual thickness (Section 3.5).

2.3.3. Pressure and Temperature Measurement. The measurement of the total pressures, $p_t$, regulator outlet pressures, $p_r$, and sidewall static pressure is obtained with a Scanivalve-pressure transducer system. The motorized Scanivalve (Scanivalve Corp. Model WS5-24) has two 24-port fluid switch wafers (Scanivalve Corp. Model W0602/1P-24T), one connected to the sidewall static pressure ports and the other to the total pressure and regulator outlet pressure ports. The Scanivalve makes one complete rotation in the duration of one run.

The static pressure port arrangement has been described in Section 2.2.2. In all, there are 32 ports, 24 or fewer of which can be connected to the Scanivalve wafer. Due to the limited time response of the system, only 12 ports are scanned, six on each test section wall. The ports used in the present experiments are shown on Figure 2.4. Each port is connected to two consecutive wafer ports, so that the 12 ports are scanned in one complete Scanivalve rotation. The collector of the Scanivalve is connected to a 0-25 psia range, capacitance-type pressure transducer (Setra Systems Model 204).

The total pressure ports are located in the contraction section of the settling chamber, while the regulator outlet pressure ports are located immediately downstream of the regulator outlet (the difference between $p_t$ and $p_r$ will be explained in Section 2.5.1.). These ports are connected to the second Scanivalve wafer and are scanned at the beginning and the end of each run. This is done to detect any significant pressure change that might occur during the run. The wafer is connected to a 0-250 psia range, capacitance-type pressure transducer

(Setra Systems Model 204). This is the same transducer that is used with the pitot probe. It can be switched from the Scanivalve to the pitot probe and vice-versa.

The total temperature measurement is done by two thermocouple probes, each immersed in the flow downstream of the pressure regulator, near the flexible hose connection. Installation was easiest in that location and no significant temperature change is expected to occur from that point to the settling chamber contraction.

Each probe consists of a type T (copper-constantan), 0.015 in. diameter thermocouple bead (Omega Engineering). The two probes are alternately connected to a single digital thermometer (Omega Model 115 TC). The response time of the thermocouple-transducer system is short enough for the purposes of the present experiments.

**2.4. Experimental Control and Data Acquisition.**

The experiment is controlled automatically by an Intel 8085 microprocessor. The shortness of the run times and the complexity of operation make this an invaluable tool. The microprocessor, after being programmed, generates 5-Volt pulses that activate relays, which in turn switch on and off the various functions of the faility. Following is a typical sequence of events that take place in a run of 2.0 second duration (t is time in seconds):

| | |
|---|---|
| t=0.00 | Solenoid valve opens (flow starts).<br>Thermocouple 1 is switched to thermometer.<br>Recording oscilloscope is triggered. |
| t=0.94 | Camera shutter opens. |
| t=1.00 | Spark light source is activated.<br>Thermocouple 2 is switched to thermometer. |

t=1.06 Camera shutter closes.

t=2.00 Solenoid valves close (flow stops).

Additionally, the microprocessor generates 24 consecutive pulses that turn the Scanivalve motor one complete rotation. The duration of the run is a variable in the microprocessor program and the above sequence of events can be expanded or contracted at will.

When the traversing probe is not used, the execution of the microprocessor program is activated manually. With the probe in operation, the program execution is activated by a switch linked to the probe motion, briefly described in Section 2.3.2. The switch closes as soon as the probe passes through a predetermined lateral location, the motor having time to achieve its full RPM.

The outputs of the pressure and temperature transducers are recorded on a two-channel, digital oscilloscope (Nicolet Model 206) and stored on floppy disk. A series of pressure gauges (Glasco), connected to every pressure stage of the facility, help monitor the experiments and set the regulator pressures.

The experiment is physically controlled from a control panel which contains the pressure gauges, pressure regulator controls, microprocessor, probe motor controls, power supplies for the instruments, and various visual indicators.

## 2.5. Operating Procedure.

2.5.1. Supersonic-Supersonic combinations. Provided that the pressure ratio is high enough and that no flow choking occurs in the nozzles, the Mach numbers at the nozzle exits are, for a given $\gamma$, functions of the nozzle geometry only. The main objective of the procedure was to set the regulator outlet pressures, $p_r$, such that the static

pressures at the nozzle exits, $p_e$, are nearly equal. The pressure $p_r$ is higher than the total pressure $p_t$ because the flow chokes somewhere between the regulators and the settling chamber, apparently at the solenoid valve. Once sufficient pressure ratio exists across the apparatus, the ratio $p_t/p_r$ depends only on the nozzle throat height and is therefore fixed for a given nozzle configuration. Knowing $p_t/p_r$, the pressures $p_t$ and $p_r$ that correspond to equal nozzle exit static pressures were calculated using the isentropic relation:

$$p_t = p_e \left[ 1 + \frac{\gamma-1}{2} M_e^2 \right]^{\frac{\gamma}{\gamma-1}}$$

The regulators were then set at or near the prescribed value and the flow was started. The sidewall static pressure distribution was displayed on the oscilloscope. If the distribution were full of "kinks", indicating strong compression and expansion waves bouncing along the test section due to pressure mismatch, the regulators were set at slightly different values and the flow was started again. The procedure was repeated until the pressure distribution became relatively smooth, at which point the experiment was finally performed. The difficulties associated with this procedure are discussed in Section 2.6.

2.5.2. Supersonic-Subsonic Combinations. In the limited number of cases that belong to this category, the low Mach number nozzle becomes a slowly diverging subsonic diffuser. The subsonic Mach number depends on the mass flow rate and the test section static pressure. A very low total pressure (almost equal to the test section static pressure) is created by bypassing the main gas supply system and by injecting gas from the regulator outlet into the settling chamber through a small sonic orifice, whose diameter is approximately 0.1 in. (2.5 mm). The subsonic Mach number at the nozzle exit is calculated from the regulator outlet pressure, orifice diameter, and test section static pressure. The exact equivalent orifice diameter is determined by measuring

the flow rate through it under choked conditions. Unless the dividing streamline of the shear layer is drastically tilted, and provided that the growth rates are relatively small, the subsonic freestream Mach number at the downstream part of the test section will be close to that calculated at the nozzle exit.

## 2.6. Experimental Difficulties.

As with any new type of experimental facility, a number of problems were encountered as a result of the nature of the flow and the unpredictable performance of some industrial hardware.

2.6.1. Pressure Regulation. Pressure regulation of the large volumetric flow rates generated in the current facility proved to be a tough problem. The pressure regulators (Grove Model 202G) were initially plagued by severe output pressure oscillation (chattering). This was cured by an internal modification that lengthens the time response to outlet pressure changes. After the modification, the regulators provided a steady outlet pressure. It was very hard, however, to predict exactly the regulator output pressure once the flow was started. That pressure could be as much as 10 psi different from the pressure at which the regulator was set. Apparently, that presure change is a function of the regulator inlet pressure and is largest when the gas cylinders are fully loaded. Many trials were thus necessary until the test section pressure distribution became satisfactory, as described in Section 2.5.1.

2.6.2. Flow Visualization. The high sensitivity of the Schlieren system, while indispensable for visualizing the flows generated here, created a few problems that caused the poor quality and subsequent rejection of many photographs. The primary difficulty stems from the fact that the Nanolamp spark, which is really an arc channel between two electrodes, can slightly "jump" from one firing to the other. That "jumping" causes the focal point on the narrow optical slit to shift away from the slit's center, thus reducing the illumination in many photographs. As mentioned in Section 2.3.1, the small slit width is

essential for obtaining high sensitivity.

Visualization was most difficult in the cases where the refractive index gradients were of the same order of magnitude with those caused by the movement of ambient air in the laboratory. This usually happened when the gases had similar refractive indices or when the shear layer spreading rate was relatively large. In these cases, it is possible to adequately visualize only the upstream part of the shear layer.

2.6.3. Adverse Pressure Gradient. Positive streamwise pressure gradient in the test section is a phenomenon that occurred in every Mach number-gas combination and was most severe in the cases where one stream is at very high Mach number and the density ratio is large, for example He at M=4 and Ar at M=2 (a case that was finally rejected). In some cases, the static pressure rise was so severe that the low Mach number stream became subsonic at some downstream location. The severely affected cases were eventually dropped from the current experimental program. In the moderately affected cases, the pressure usually rose sharply in the first 1/3 length of the test section and leveled off for the remaining length. This permitted the calculation of a local Mach number, based on an average static pressure, over the downstream half of the test section. This is the region where the turbulent growth rates are measured. The outward deflection of the test section sidewalls lessened the magnitude of the pressure rise without being able to fully compensate for it. This phenomenon and its implications are discussed in Section 3.3.

2.6.4. Limited Gas Supply. Perhaps the main difficulty of the current experiments stems from the limited supply of gases, which does not allow sufficient time for experimentation. As mentioned previously, many trials were necessary in order to set the right conditions for a particular measurement. These trials depleted the gas supply and sometimes there was hardly enough gas left to make a couple of runs. The situation was most difficult when one of the gases was helium

because of its high volumetric flow rates. Ironically, the cases that involved helium were usually the ones that required the largest number of trials.

2.7. Run Conditions.

All runs were restricted to 1.5 to 2.0 second duration in order to conserve gas and maintain nearly steady-state conditions during each run. The total pressures ranged from 0 to 80 psig, while the test section static pressures ranged from 0.2 psia to 2.5 psia. The total temperatures were measured to be very close to room temperature and in most cases are within 5% of each other. The maximum total temperature difference recorded here is 20 degrees C, which is too small to cause any significant change in the flow parameters.

A list of all the Mach number-gas combinations covered in the experiments is presented in Table 2.3 below. $M_e$ is the ideal nozzle exit Mach number and M is the actual Mach number at the downstream part of the test section, where the growth rates are measured. M is calculated by knowing the average freestream pitot pressure, $p_t'$, and static pressure, p, over the downstream half of the test section and by using the Rayleigh pitot formula:

$$\frac{p_t'}{p} = \left\{\frac{(\gamma+1)\,M^2}{2}\right\}^{\frac{\gamma}{\gamma-1}} \left\{\frac{\gamma+1}{2\gamma M^2 - (\gamma-1)}\right\}^{\frac{1}{\gamma-1}}$$

The maximum variation of M along the downstream half of the test section is typically 5% of the value of M computed by the above method. Representative static pressure distributions, on which the above calculation is based, are shown on Figure 3.5. For the supersonic/subsonic combinations, the subsonic Mach number is calculated by the method described in Section 2.5.2.

The test cases are tabulated in order of increasing compressibility, based on a compressibility-effect parameter that will be introduced in Chapter 4. Their designation indicates the two gases used (A=argon, H=helium, N=nitrogen), the fastest gas placed first, and the order of compressibility. For example, in cases HN6 and HN9 helium is in the fast stream, nitrogen in the slow stream and HN9 is more compressible than HN6. The velocity ratio $U_2/U_1$ and density ratio $\rho_2/\rho_1$, calculated at the downstream conditions, are listed for each case.

Table 2.3. Mach Number-Gas Combinations

| Case | Gas 1 | $M_{e1}$ | $M_1$ | Gas 2 | $M_{e2}$ | $M_2$ | $\rho_2/\rho_1$ | $U_2/U_1$ |
|---|---|---|---|---|---|---|---|---|
| NA1 | $N_2$ | 1.9 | 1.6 | Ar | 4.0 | 3.3 | 4.4 | 0.93 |
| AA2 | Ar | 4.0 | 3.4 | Ar | 2.0 | 1.8 | 0.43 | 0.81 |
| NN3 | $N_2$ | 3.3 | 3.1 | $N_2$ | 1.9 | 1.7 | 0.54 | 0.74 |
| NA4 | $N_2$ | 3.0 | 2.8 | Ar | 3.0 | 2.6 | 1.8 | 0.75 |
| NA5 | $N_2$ | 3.5 | 3.2 | Ar | 2.3 | 2.1 | 1.2 | 0.67 |
| HN6 | He | 2.3 | 1.7 | $N_2$ | 3.5 | 3.0 | 9.2 | 0.52 |
| AA7 | Ar | 4.0 | 3.1 | Ar | 0.2 | 0.2 | 0.24 | 0.13 |
| HN8 | He | 3.0 | 2.6 | $N_2$ | 3.0 | 2.8 | 5.5 | 0.42 |
| HN9 | He | 4.0 | 3.4 | $N_2$ | 1.9 | 1.6 | 2.2 | 0.29 |
| HA10 | He | 4.0 | 3.1 | Ar | 0.3 | 0.3 | 2.4 | 0.04 |

An attempt was made to measure the fluctuation level in the settling chamber by installing a pressure transducer of millisecond time response (PCB) near the gas inlet to the settling chamber (installation near the contraction would have been very difficult). With the facility in operation, the transducer output showed an oscillation with

frequency of the order of 100 Hz and amplitude less than 1% of the absolute pressure. That oscillation was more apparent at the starting of the flow and usually decayed to very low levels in the first 100 ms after the opening of the solenoid valves. It is traced to the motion of the pressure regulator valve which tries to adjust to the downstream conditions. No other disturbance of higher frequency was detected. Since the frequencies associated with the structures of the present shear layers are of the order of 100 kHz and higher, the effect of the total pressure oscillation on the development of the shear layer is believed to be insignificant. It is highly unlikely that any device in the high-pressure section of the facility would generate frequencies so high as to cause forcing of the shear layer.

# Chapter 3
# Experimental Results

In this chapter, the results obtained in the current experiments are presented uncorrelated with any compressibility-effect parameter. Such a parameter is introduced in Chapter 4 and the appropriate correlations are done in Chapter 5.

## 3.1. Schlieren Photography.

Schlieren photographs of all ten test cases investigated here are shown on Figures 3.1(a) through 3.1(j). The Reynolds numbers at which the flows were photographed are representative of those that occurred in the measurements of the growth rates. The shear layer is believed to be turbulent for at least the downstream two thirds of the test section. In Figures 3.2(a) and 3.2(b), photographs of cases NA4 and HN8 are shown at relatively low Reynolds numbers. All photographs are presented full-scale. For each test case, usually two photographs are shown, the upper one showing the upstream part of the test section and the lower one showing the downstream part. The two photographs are taken at different runs under the same flow conditions. They overlap 0.5 inch, unless stated otherwise. The trailing edge of the centerbody is located where the initial compression and expansion waves originate. In a few cases, only the upstream photograph is shown because the vanishing refractive index gradients do not permit visualization of the downstream part of the flow.

3.1.1. Waves in the Test Section. Compression and expansion waves originating from the trailing edge of the centerbody are visible in all photographs. These waves, and possibly others generated further downstream, reflect on the test section walls and impinge on the shear layer as they propagate downstream. Ideally, if the static pressures at the nozzle exits were perfectly matched, there would be no waves. In reality, even if the pressures are exactly matched, waves will be produced from the finite thickness of the centerbody's tip and the

displacement thicknesses of the trailing edge boundary layers. The possibly sloping dividing streamline of the shear layer may produce more waves downstream, even if the nozzle exit pressures are equal. The growth of the displacement thickness of the shear layer, which is quite rapid near the trailing edge (Section 3.3), further complicates the flowfield and is another source of waves. It is thus very difficult, and perhaps impossible, to completely eliminate the waves throughout the test section. It is believed here that the current pressure setting procedure, described in Section 2.5.1, by which the nozzle exit pressures are set such that the sidewall pressure distribution is the smoothest possible, works best in minimizing the strength of waves impinging on the shear layer.

3.1.2. Growth Rates. It is evident from the photographs that the shear layer spreading rates are remarkably smaller than those usually observed in subsonic experiments. It would be premature, however, to conclude that compressibility is the only major cause for the small spreading rates. Other, equally important flow parameters, like the velocity and density ratios, should also be considered. This is a subject to which Chapter 5 is devoted.

One way to measure the visual spreading rates from the photographs is to fit straight-line mean tangents to the edges of the layer, as done by Brown and Roshko [1974]. This has been done in the current facility (Papamoschou and Roshko [1986]), covering most cases under investigation here. Due to the smallness of the growth rates and the uncertainty in defining the edges of the layer, such procedure is subjective and of limited accuracy. The results obtained by the above method, however, are in qualitative agreement with the present results.

The decay of the refractive index gradients with downstream distance may sometimes create the appearance that the shear layer grows very slowly or that it even gets thinner! One must then be cautious in interpreting growth rates from Schlieren photographs, especially when

the indices of refraction are very small, as is the case here. The thickness of the shear layer, as it appears on the Schlieren photograph, may vary with the sensitivity of the Schlieren system. If the edges of the layer are well defined, increasing the sensitivity beyond a threshold level should not produce significant change in the layer thickness. If the edges are not well defined, increasing the sensitivity may result in an apparent thickening of the layer. Interestingly, the layer edges appear, on the average, better defined in the less compressible cases and less well defined in the more compressible cases. For example, the edges of case NN3 (Figure 3.1(c)) are better defined than the edges of case HN8 (Figure 3.1(h)). This could be due to the fact that, in the current experiments, the growth rate of the highly-compressible cases is relatively large, thus the refractive index gradients across the shear layer small. It may also be related to the decay rate of a disturbance away from the layer which, we hypothesize, is slower for the highly-compressible cases. The latter point stems from a vortex sheet analysis presented in Section 4.1.

3.1.3. Shear-Layer Structures. Large structures, reminiscent of those found in subsonic mixing layers, can be seen in most Schlieren photographs. Evidence of large-scale structures in supersonic shear layers has been previously found in the experiments of Ortwerth and Shine [1977] and Oertel [1979]. Although the structures observed in the current experiments are not as clearly defined as, for example, those observed in the subsonic experiments of Brown and Roshko [1974], some rough measurements can be obtained from the photographs.

Of primary interest here is the mean scaling of the structure spacing, $\ell$, with the pitot thickness of the layer, $\delta_{pit}$. Similar measurements, in subsonic shear layers, have been made in the past by various investigators. Brown and Roshko found that the ratio $\ell/\delta_\omega$ stays fairly constant with downstream distance and has the value of about 3. Koochesfahani et al. [1979] found $\ell/\delta_\omega=3.9$ while measurements of Jones et al. [1973] imply that $\ell_m/\delta_\omega=5.1$, where $\ell_m$ is the most frequent

structure spacing (found to be almost equal to $\ell$ by Brown and Roshko). Assuming that $\delta_\omega/\delta_{pit}=0.60$, a relation that will be suggested in Section 3.5, Brown and Roshko's result translates to $\ell/\delta_{pit}=1.8$, and that of Jones et al. to $\ell/\delta_{pit}=3.1$.

A "mean" structure spacing is obtained from the Schlieren photographs by measuring the length of a row of 3 to 5 vortical structures centered around an average x-position and then dividing that length by the number of vortices included in it. Where possible, this is done at two streamwise locations, one near the middle of the test section and one near the end. The thickness of the layer is known from the pitot pressure profile measurements, which will be shown in Section 3.2. It is found that the ratio $\ell/\delta_{pit}$ does not change significantly with downstream distance, the maximum difference measured here being 15% of the average value. In the cases where $\ell$ is measured at two streamwise positions, the average value of $\ell/\delta_{pit}$ is presented in the table below. Clearly, the above method of measuring structure spacings is much inferior to that used by the subsonic shear layer investigators, they having the advantage of tracking the structures with movies. The current technique is estimated to be 25% accurate.

The measured values of $\ell/\delta_{pit}$ for 9 Mach number-gas combinations are presented below in Table 3.1. Unfortunately, the poor visualization in case HA10 did not allow identification of any structures in that flow.

Table 3.1. Mean Structure Spacing Normalized by Pitot Thickness

| Case | $\ell/\delta_{pit}$ |
|---|---|
| AN1 | 2.0 |
| AA2 | 2.3 |
| NN3 | 2.3 |
| NA4 | 2.0 |
| NA5 | 2.1 |
| HN6 | 2.5 |
| AA7 | 1.5 |
| HN8 | 1.2 |
| HN9 | 1.2 |

It appears that in the highly compressible cases (AA7 and beyond) the ratio $\ell/\delta_{pit}$ is approximately half of that in the less compressible cases. This will be further discussed in Section 5.2. For the less compressible cases, the values of $\ell/\delta_{pit}$ are close to the value of 1.8, implied by Brown and Roshko.

3.1.4. Laminar-to-Turbulent Transition. In all the photographs shown on Figures 3.1(a) to 3.1(j), it appears that the shear layer becomes turbulent after a very short initial laminar region. The trailing edge boundary layers are believed to be laminar, the arguments to that being presented in Section 3.2.2. It was desired to extend the laminar region by lowering the unit Reynolds numbers in order to observe a more gradual transition to turbulence. From these observations, a rough estimate of the transition Reynolds number could be obtained.

The investigation of the transition region is rather limited. Only two Mach number-gas combinations were exploited. These combinations are NA4 ($N_2$ at $M_e$=3.0 and Ar at $M_e$=3.0) and HN8 (He at $M_e$=3.0 and $N_2$ at $M_e$=3.0). The above cases were chosen primarily because the total pressures of the two streams are about equal, making it easy to vary the total and thus the test section static pressure by a wide range. In all other cases, the total pressure ratio is greater than 6, which limits the range of static pressures because of structural and flow rate constraints. Additionally, the above two cases offer better than average flow visualization.

Schlieren photography at the very low test section static pressures established in this part of the investigation proved to be quite difficult. The refractive indices were extremely small and the edges of the layer lost their definition. Nevertheles, it was possible to distinguish some features of what appears to be the transition region. Figures 3.2(a) and 3.2(b) are Schlieren photographs at low pressure of cases NA4 and HN8 respectivelly. In both cases, the test section pressure is approximately 0.20 psia. The following features are observed from the photographs and apply to both cases: initially, the layer is laminar, grows extremely slowly and produces a relatively sharp contrast on the photograph; then it becomes wavy, with the disturbance waves confined within the edges of edges of the almost straight layer which now loses its initial sharpness; further downstream, the layer breaks up into structures. Although it is hard to pinpoint the onset of transition, there is no doubt that by the midlength of the test section layer is turbulent. For case NA4, it appears that transition starts about 40 mm downstream of the trailing edge. For case HN8, that distance is about 60 mm. The above estimates of distance to transition are subjective and should be treated as such. In both cases, the layers are turbulent 100 mm downstream of the trailing edge.

The definition of a single transition Reynolds number that can adequately characterize the state of a two-stream shear layer is a difficult, if not impossible, task. Some researchers base the Reynolds number on the properties of the high speed fluid and the distance to transition. Others base it on the velocity difference, one of the kinematic viscosities or their average, and the thickness of the layer. The latter definition would provide a rather poor transition criterion here, since the thickness of the initially laminar layer hardly grows with downstream distance It seems more useful to list the transition Reynolds numbers based on the properties of each fluid and the estimated distance to transition, $x_{tr}$. It is important to note that in cases NA4 and HN8 the Reynolds number of the high-speed stream is lower than that of the low-speed stream, a contrast to the familiar situation in homogeneous shear layers.

It is likely that the Reynolds number alone does not adequately characterize the transition process. If the transition is an inviscid process, essentially a Kelvin-Helmholtz type of instability, one might expect that the definition of a Reynolds number is less important and that distance to transition scales with initial conditions. Indeed, Roshko and Lau [1965], in their experiments of transition and reattachment of incompressible free shear layers, find that $x_{tr}$ is much better correlated with the boundary layer thickness before separation than with the Reynolds number based on $x_{tr}$. Bradshaw [1969] and Breidenthal [1981] also suggest that $x_{tr}$ scales with the momentum thickness at the trailing edge, $\theta$. With that in mind, the ratios $x_{tr}/\theta_1$ and $x_{tr}/\theta_2$ have been calculated and are presented in Table 3.2, together with the transition Reynolds numbers based on $x_{tr}$.

Table 3.2. Shear Layer Transition Reynolds Numbers

| Case | $\frac{U_1 x_{tr}}{\nu_1}$ | $\frac{U_2 x_{tr}}{\nu_2}$ | $\frac{x_{tr}}{\theta_1}$ | $\frac{x_{tr}}{\theta_2}$ |
|---|---|---|---|---|
| NA4 | 120,000 | 190,000 | 470 | 670 |
| HN8 | 100,000 | 180,000 | 640 | 720 |

Examination of the possible effect of compressibility on transition Reynolds number and comparisons with results of other investigators will be presented in section 5.2.

## 3.2. Turbulent Growth Rates.

3.2.1. Method of Measurement. Turbulent growth rates are measured by applying straight-line least-squares fit to the pitot thickness data over the downstream half of the test section. The pitot thickness is obtained by the pitot pressure profile as shown on Figure 2.10. It is believed that the flow is fully turbulent in that region, something that will be closely examined in section 3.2.2. Futhermore, the static pressure variation over that region is small enough that the freestream conditions can be treated as constant without significant error. For each case, the layer thickness is measured at typically six to eight streamwise locations. The growth rate is deduced from at least four thickness measurements in the downstream region of the layer. Figure 3.3 shows representative pitot pressure profiles at four x-locations for all present cases.

For each test case, the shear layer thicknesses were obtained at approximately the same static pressure. For a couple of cases, the thicknesses were measured at different static pressures to detect

possible Reynolds number effect on the turbulent growth rate. The unit Reynolds numbers were varied by a factor of two and no effect was observed within the accuracy of the measuring technique. In the case of subsonic shear layers, it is generally assumed that the growth rate of the fully-developed flow is largely independent of Reynolds number. However, this issue is not fully resolved yet. In the shear-layer experiments of Mungal et al. [1984], there is evidence that the layer thickness varies modestly with Reynolds number. In the current investigation, although the measurements are too few to make any solid conclusions, we neglect any Reynolds-number effects on the turbulent growth rate. More important here is the effect of the strength of waves impinging on the layer: the thickness of the layer can increase as much as 25% if the streamwise static pressure is very "bumpy", implying the presence of relatively strong waves throughout the test section. It was often necessary to repeat a particular measurement many times until the pressure distribution appeared to be the smoothest possible. The growth rate data presented here are believed to have been obtained near the best possible conditions achievable in the current facility. That, however, does not preclude room for improvement and the scatter of the data may indicate that some thicknesses could be as much as 5% smaller if the pressure distribution were ideal.

The shear layer pitot thickness measurements are shown on Figure 3.4 for all ten test cases. The straight lines that fit the downstream portion of the data are also shown, except for case NA1. Case NA1 is essentially a wake flow and fitting a straight line through the data would be inappropriate. That case is examined in Section 3.2.3. The standard deviation of the data points from the straight-line least-squares fit, as a fraction of the growth rate, does not exceed 5%. The overall uncertainty of the growth rate measurement is estimated to be ±10%. The growth rates, together with other relevant quantities, are summarized in section 3.2.2.

The straight-line least-squares fit produces a displaced origin of the shear layer which, in some cases, is located as much as 60 mm upstream of the trailing edge. Considering the small growth rates, the finite boundary layer thicknesses at the trailing edge, and the possibly parabolic growth of the initial laminar layer, such great origin displacements should not be surprising. It should be noted, however, that the origin displacement thickness found by the above method is very sensitive to the accuracy of the thickness measurements and could be up to ±30% in error. Sirieix and Solignac [1966] found experimentally that the displaced origin of a M=3, one-stream shear layer is located about 20$\delta$ upstream of the separation point, where $\delta$ is the velocity thickness of the boundary layer before separation. In the present experiments, a typical combined $\delta$ of the two streams is about 1.5 mm (Section 3.2.2). Putting that in Sirieix and Solignac's formula, we obtain an origin displacement of about 30 mm, which falls in the range of the origin displacements found here.

3.2.2. Trailing-Edge Boundary-Layer Thickness. The primary motivation for calculating the boundary layer thickness at the trailing edge is the need to know whether the turbulent shear layer has had enough length to develop so that it is independent of initial conditions. Bradshaw [1966] suggests that for a one-stream, subsonic shear layer the distance to a fully developed turbulent flow is of the order of 1000 momentum thicknesses of the initial boundary layer. On the other hand, Sirieix and Solignac [1966] found that for a one-stream, M=3 shear layer that distance is only 10 boundary layer velocity thicknesses, which translates to about 200 momentum thicknesses. Bradshaw's criterion is used here because it is more conservative. It is applied to both streams, since it is not known whether a single momentum thickness can adequately define the initial conditions of a two-stream shear layer that unavoidably has a wake component.

Before proceeding with any calculation, it is important to first establish whether the trailing edge boundary layers are laminar or turbulent. From their appearance on the Schlieren photographs it is almost certain that they are laminar. A more objective criterion would have been the Reynolds number based on nozzle length, $Re_L$, if reliable transition Reynolds numbers elsted for supersonic nozzle boundary layers. Unfortunately, transition experiments, even for flat plates, have been very limited. Mack [1975] has summarized transition Reynolds numbers for compressible boundary layer over flat plate, measured by various investigators. The trend of the data indicates that the transition Reynolds number based on distance from leading edge, $Re_t$, has a minimum value of $1.5 \times 10^6$ near M=4. That trend is inconsistent with results of linear stability theory, which predicts monotonically increasing stability with increasing Mach number. Furthermore, the transition Reynolds number of a boundary layer in an accelerating freestream, as in a supersonic nozzle, could be significantly lower that that of a flat plate boundary layer. The value of $Re_t=1.5 \times 10^6$, believed here to be very conservative, will be compared to $Re_L$ to judge the state of the trailing edge boundary layers.

The highest $Re_L$ established under the current growth rate measurement conditions is $2.6 \times 10^6$ in the $M_e=4$ stream of case AA2. In all other cases, $Re_L$, is near or below $1.5 \times 10^6$. Case AA2 appears marginal in that respect, while all other cases appear to have laminar trailing edge boundary layers. Given the great conservatism of the above transition criterion, however, it is strongly doubted that the boundary layers of case AA2 are turbulent or even transitional.

The boundary layer momentum thickness at the trailing edge is obtained by first calculating the momentum thickness, $\theta$, along the subsonic contraction using the Thwaites [1949] method. The thickness at the beginning of the contraction is assumed to be zero. Along the supersonic nozzle, $\theta$ is calculated by a compressible Thwaites method proposed by Rott and Crabtree [1953]. It uses the Illingworth-

Stewartson transformations to reduce the compressible problem into an equivalent incompressible one, assuming adiabatic wall. The calculation starts at the nozzle throat, where $\theta$ is known from the previous subsonic calculation.

For the cases where one stream is subsonic, a Thwaites calculation along the nozzle (which now becomes a diverging subsonic diffuser) revealed that the boundary layer is likely to separate 10 mm downstream of the throat. This is not considered a serious problem because the subsonic stream is so slow, compared to the supersonic one, that it is merely there to establish a density difference and provide the entrainment needs of the shear layer. Thus, the initial conditions of the subsonic stream are not likely to affect the development of the shear layer. Nevertheless, it would have been more appropriate to design a converging nozzle for the subsonic stream. That, however, entails a very asymmetric centerbody design, difficult to fabricate and requiring extensive modifications of the test section.

It is worth noting here that $\theta$ depends strongly on the freestream acceleration and rather weakly on compressibility. An incompressible Thwaites calculation along the supersonic nozzle, based on the actual supersonic flowfield, gives a value of $\theta$ quite close to that obtained by the compressible Thwaites method for the Mach number range established here. In contrast to that, the boundary layer displacement thickness, $\delta^*$, is a strong function of compressibility: the ratio $H=\delta^*/\theta$, known as the "shape factor", increases dramatically with Mach number. Rott and Crabtree [1952] propose the relation,

$$H = \frac{T_t}{T_\infty} (H_i + 1) - 1 \qquad (3.1)$$

where $T_t$ is the stagnation temperature, $T_\infty$ the freestream temperature, and $H_i$ the incompressible shape factor, whose value is 2.6 for flat plate. For example, a M=4, $\gamma$=5/3 boundary layer over insulated flat

plate has H=22, almost an order of magnitude larger than its incompressible value. The ratio $\delta^*/\delta$, as tabulated by White [1974], is 0.6 for M=2, 0.8 for M=4 and approaches 1 for very high Mach numbers.

The momentum and displacement thicknesses of the trailing-edge boundary layers, calculated by the above methods, are shown on Table 3.3:

Table 3.3. Trailing-Edge Boundary-Layer Thicknesses

| Case | $\theta_1$(mm) | $\delta_1^*$(mm) | $\theta_2$(mm) | $\delta_2^*$(mm) |
|---|---|---|---|---|
| AN1 | 0.025 | 0.47 | 0.080 | 0.41 |
| AA2 | 0.021 | 0.39 | 0.076 | 0.57 |
| NN3 | 0.042 | 0.44 | 0.069 | 0.36 |
| NA4 | 0.038 | 0.31 | 0.028 | 0.33 |
| NA5 | 0.051 | 0.59 | 0.062 | 0.56 |
| HN6 | 0.091 | 0.82 | 0.042 | 0.49 |
| AA7 | 0.024 | 0.46 | * | * |
| HN8 | 0.040 | 0.47 | 0.035 | 0.28 |
| HN9 | 0.039 | 0.74 | 0.072 | 0.38 |
| HA10 | 0.045 | 0.84 | * | * |

* : Boundary layer likely to separate upstream of trailing edge

Based on the above values of $\theta$, the following quantities are calculated: $x_{gr}/\theta$, where $x_{gr}$ is the distance (from trailing edge) of the upstream-most thickness datum used in the calculation of the turbulent growth rate according to Section 3.2.3; $Re_\theta = U\theta/\nu$ at the trailing edge

flow conditions. These quantities, together with the visual growth rate $\delta'_{pit} = d\delta_{pit}/dx$ and the unit Reynolds number Re' for each stream, based on the downstream flow conditions, are shown on Table 3.4:

Table 3.4. Growth rates with corresponding $x_{gr}/\theta$ and Re'

| Case | $\delta'_{pit}$ | $\frac{x_{gr}}{\theta_1}$ | $Re_{\theta_1}$ | $Re'_1(mm^{-1})$ | $\frac{x_{gr}}{\theta_2}$ | $Re_{\theta_2}$ | $Re'_2(mm^{-1})$ |
|---|---|---|---|---|---|---|---|
| AN1 | ** | ** | 640 | 22800 | ** | 250 | 2600 |
| AA2 | 0.030 | 3400 | 800 | 17900 | 900 | 310 | 7000 |
| NN3 | 0.027 | 2000 | 680 | 16100 | 1200 | 290 | 4000 |
| NA4 | 0.028 | 2100 | 540 | 17400 | 2800 | 600 | 22600 |
| NA5 | 0.026 | 1800 | 600 | 16600 | 1400 | 370 | 8700 |
| HN6 | 0.023 | 1000 | 230 | 2600 | 2100 | 700 | 16500 |
| AA7 | 0.036 | 3000 | 640 | 23700 | * | * | 260 |
| HN8 | 0.038 | 2000 | 430 | 13000 | 1100 | 600 | 27800 |
| HN9 | 0.028 | 1800 | 410 | 15300 | 1000 | 290 | 4500 |
| HA10 | 0.069 | 1600 | 360 | 8200 | * | * | 380 |

*: Boundary layer likely to separate upstream of trailing edge

**: Wake flow

The calculated values of $x_{gr}/\theta$ presented above indicate that all cases satisfy Bradshaw's criterion. While this is comforting to know, it should be interpreted cautiously in view of the very limited information about self-similar behavior of supersonic shear layers.

Finally, a note should be made on the effects of $\delta^*$ on nozzle flow. It was mentioned in Section 2.2.3 that the nozzle contours were designed without correcting for the boundary layer displacement

thickness. From the values of $\delta^*$, shown on Table 3.4, it is clear that the He nozzles have the greatest $\delta^*$. This is to be expected since He has a low unit Reynolds number. The nozzle exit area is effectively decreased by about 15%, while $\delta^*$ at the throat is calculated to be too small to make any appreciable change in the effective throat area. For a nozzle designed for an ideal $M_e$=4.0, the reduced effective area ratio results in an actual $M_e$=3.8. This small change is not important for the purposes of the current experiments. Also, the uniformity of the nozzle exit profiles, shown on Figure 2.7, suggests that $\delta^*$ does not cause significant deterioration of the Foelsch nozzle performance. In that respect, the decision not to correct the nozzle contour was a practical one that apparently did not compromise the flow quality at the nozzle exits. On the other hand, in applications where $M_e$ must have a precise value, that correction must obviously be included.

3.2.3. Wake Effect. In a two stream shear layer, the initial region of the flow is wake-dominated due to the finite thickness of the trailing edge and the displacement thicknesses of the trailing edge boundary layers. It is desired to obtain an estimate of the extent of the wake-dominated region in the current supersonic shear layers.

In the cases where the two gases are dissimilar, the velocity is not necessarily a monotonic function of pitot pressure and, since no concentration measurements were made here, the construction of accurate velocity profiles from pitot pressure profiles would require additional (ad-hoc) assumptions. Extracting wake information from pitot pressure profiles can thus be misleading: a deficit in the pitot pressure profile may not be due to the wake but rather to the mixing process. Striking examples of that are cases NA4 and HN8 where the total pressures are almost equal while the velocities are different: the pitot pressure profile has a wake-like appearance (Figure 3.3) all the way to the end of the test section where the flow is almost certainly a fully developed shear layer. The occurrence of a deficit in these cases is explained later in this section. On the other hand, the pitot pressure

profiles of case AN1, which is a pure wake flow, appear like shear layer profiles with no evidence of deficit from the first measuring station at x=20 mm. Clearer presence of the wake is observed in cases NA5 and HN6, where a deficit appears at the upstream stations that dissappears at the downstream stations. That deficit last occurs at x=63 mm in both cases. It should be kept in mind that even in these cases the deficit could be partly due to the mixing process.

The distance of 60 mm is used here as a conservative estimate of the extent of the wake-dominated flow. The measurements of turbulent growth do not start till x=75 mm, so we can assume with some confidence that they lie outside the region affected by the wake.

The pitot pressure deficit in cases NA4 and HN6, and possibly in other heterogeneous cases, can be justified on the basis of entropy increase due to mixing. It can be easily shown that, for a turbulent Prandtl number close to unity, the differential equation that governs the mean entropy s is

$$u\frac{\partial s}{\partial x} + v\frac{\partial s}{\partial y} = -\frac{R}{p}\, u\, \frac{\partial \tau}{\partial y} \qquad (3.2)$$

where $\tau$ is the shear stress. Introducing the similarity variable $\eta$=y/x and using the continuity equation, (3.2) takes the form

$$\frac{ds}{d\eta}\left[\frac{1}{\rho}\int_{-\infty}^{\eta}\rho u d\eta\right] = \frac{R\ u}{p}\,\frac{d\tau}{d\eta} \qquad (3.3)$$

Any static pressure variation across the layer is assumed negligible. The distribution of the right-hand side of (3.3), as well as that of its components, is illustrated on Figure 3.5, where $\eta$=0 denotes the location of the dividing streamline. We note that the term in brackets on the left-hand side of (3.3) is positive. Clearly, $d\tau/d\eta$ and $ds/d\eta$ are both positive for $\eta<0$ and negative for $\eta>0$ (provided, of course, that $du/d\eta>0$, which is the convention here). Thus, s behaves

qualitatively as $\tau$, i.e., it has a maximum within the layer. We conclude, therefore, that there is an entropy increase inside the layer. To illustrate how that produces a pitot-pressure defect in the cases where the total pressures are nearly equal, we study the following simple example. We consider a shear layer with $M_1 = M_2$, $\gamma_1 = \gamma_2$, but $U_1 \neq U_2$ because the gases have different molecular weights (the stagnation temperature is assumed uniform). We thus have $T_1 = T_2$ and $p_{t_1} = p_{t_2}$. At some fixed x-location, the entropy variation across the layer, s(y), can be related to the temperature variation, T(y), through the first thermodynamic law:

$$s(y) - s_j = c_p(y) \ln \frac{T(y)}{T_j} \tag{3.4}$$

where subscript j=1,2 denotes the freestream conditions. We are reminded that, based on our assumption that the turbulent Prandtl number is unity, $T_t$ is constant throughout the flowfield. If we could somehow place in the flow a probe that measures $p_t$ directly by bringing the flow to rest isentropically, then T(y) would be given in terms of $p_t(y)$ by

$$\frac{T(y)}{T_j} = \left[\frac{p_t(y)}{p_{t_j}}\right]^{-\frac{\gamma-1}{\gamma}} \tag{3.5}$$

Substituting (3.5) into (3.4) we have

$$s(y) - s_j = - R(y) \ln \frac{p_t(y)}{p_{t_j}} \tag{3.6}$$

It is evident from (3.6) that for s(y) to be uniquely defined we must have $s_1 = s_2$. Since the left hand side of (3.5) is positive inside the mixed region, $p_t(y)$ has a deficit within the layer. Given that p is constant across the layer, the Mach number distribution has a deficit,

thus the pitot pressure distribution also has a deficit.

3.2.4. Growth of a Wake Flow. Case NA1 (Ar at $M_e$=4.0 and $N_2$ at $M_e$=1.9) is an interesting flow situation where the velocities are equal while the Mach numbers are very different. Since this is a wake, rather than a shear layer, its far field growth is expected to be parabolic. With that in mind, the quantity $\delta^2_{pit}$ is plotted versus x in Figure 3.6. The plot exhibits nearly linear behavior, and a straight line least squares fit through the thickness data downstream of x=40 mm gives:

$$\frac{\delta^2_{pit}}{x-x_0} = 0.16 \text{ mm}$$

where $x_0$, the virtual origin, is -5 mm. The growth of the farfield wake is found from similarity arguments to be

$$\delta^2_{pit} = C_{pit} (x-x_0) \theta_w \qquad (3.7)$$

where $\theta_w$ is the momentum defect thickness and $C_{pit}$ is a non-dimensional constant to be determined. Since the velocity and density profiles cannot presently be known, is not clear what to use as $\theta_w$ here. Konrad [1977] and Roberts [1985], in their studies of wakes, have used $\theta_w = \theta_1 + \theta_2$, where $\theta$ is the momentum thickness of the trailing edge boundary layer. Doing the same here, using the values of $\theta$ shown on Table 3.3, we have $\theta_w$ = 0.10 mm. Substituting that in (3.7) we get $C_{pit}$= 1.6. In the literature it is more common to find the growth rate in the form:

$$y^2_{1/2} = C_1 (x-x_0) \theta_w$$

where $y_{1/2}$ is one half of the half-defect width. Typically $C_1 \approx 0.1$, as found in the subsonic experiments of Sreenivasan ans Narasimha [1982] and the supersonic experiments of Demetriades [1969]. It is desired to

somehow translate the value of $C_{pit}$=1.6. obtained here. to an equivalent value of $C_1$. If we make the rough approximation that $\delta_{pit} \simeq 4\ y_{1/2}$ we get $C_1 \simeq 0.1$. This apparent agreement with the results of the other investigators is subject to the validity of the assumptions and approximations made here.

The implication that the subsonic wake and the supersonic wake obey the same growth laws may seem surprising at first but one should consider that in the far wake the velocity defect becomes eventually subsonic with respect to the freestream velocity. Thus, the supersonic far-field wake is not fundamentally different from the subsonic one.

### 3.3. Streamwise pressure gradient.

The static pressure gradients encountered during the measurements of the growth rates are shown on Figure 3.7 for all ten cases. The common trend is a rapid pressure increase near the trailing edge followed by a region of relatively small pressure gradient. At the end of the test section the pressure rises again but this is thought to be an upstream influence of the diffuser shock waves, possibly propagated through a separated boundary layer. Fortunately, the slow pressure change over the downstream half of the test section allowed the calculation of average freestream conditions associated with the growth rate measurements. as described in Section 2.7.

Letting p be the average downstream static pressure and $p_e$ the nozzle exit pressure. the mildest pressure increase occurs for case NN3. where $p/p_e$=1.2 and the largest one for cases HN9 and HA10. where $p/p_e$=2.0. Some Mach number-gas combinations. achievable with the current set of centerbodies. namely He at $M_e$=4.0 / Ar at $M_e$=2.0 and Ar at $M_e$=4.0 / He at $M_e$=2.0 produced such severe pressure gradients that the low Mach number stream eventually became subsonic at some downstream distance and flow breakdown was evident at the nozzles. Full outward deflection of the top and bottom walls did little to improve the situation. After numerous trials. no region of mild pressure

gradient could be established and the above two combinations were dropped from the experimental program.

The streamwise pressure rise, while a nuisance in the accomplishment of the current research goals, became an intriguing phenomenon in itself that merited further investigation. Generally speaking, the basic cause of the pressure rise is the entropy increase due to mixing. In that respect, the shear layer can be viewed as a two-stream equivalent of Fanno flow. That property of supersonic shear layers has been appreciated by researchers of supersonic-supersonic ejectors where the goal is efficient pressure recovery. Dutton et al. [1982] conducted experimental and theoretical studies of such ejectors. In a set-up similar to the present one, they established shear layers with pressure gradients of the same nature as the ones observed here. Their control-volume analysis of a constant-area supersonic planar shear layer with uniform mixed conditions revealed the elstence of two solutions for the mixed flow: one supersonic and isentropic; one subsonic that is equivalent to a two-stream shock solution. The subsonic solution applies to the actual experiment since mixing produces entropy. As might be expected, the higher the Mach numbers of the unmixed flow, the greater the pressure recovery.

The rapid pressure rise near the trailing edge suggests an equally rapid local growth rate of the shear layer displacement thickness, $\delta^*$. Essentially, $\delta^*(x)$ acts like a solid, initially concave wedge between the two streams, with its apex near the trailing edge and orientation such that the static pressures in the two freestreams are roughly equal. The pressure rise is transmitted along Mach lines originating from that fictitious wedge. Downstream of the the initial region of fast pressure rise, $\delta^*(x)$ grows slowly and its effect can to some extent be counteracted by outward deflection of the test section walls.

Adverse pressure gradients, similar to the ones encountered in the present experiments, have also been reported by Devis [1972] in a shear layer consisting of He at M=0.98 and $N_2$ at M=2.78. Ferri and Edelman [1967] have carried out analytical and numerical investigation of compressible mixing under constant area or constant pressure conditions. Their computations of the constant-area mixing of a coalal jet formed of $H_2$ at $M_e$=2.0 and $N_2$ at $M_e$=2.0 show the presence of very strong adverse pressure gradients, the static pressure reaching 3 times its jet exit value in a short distance from the jet origin.

In shear layers with one stream supersonic and one stream subsonic, if the Mach number of the supersonic stream is not large, approximately less than 2, then it is possible, depending on the freestream conditions, to have an adverse or a favorable pressure gradient. As an example, Cosner [1976] in his investigation of a $M_e$=1.4 / $M_e$=0.6 shear layer, with air in both streams, observed a slight negative pressure gradient along his test section. On the other hand, if the Mach number of the supersonic stream is large, as in the present supersonic-subsonic combinations (cases AA7 and HA10), the potential for pressure recovery is great and the pressure will certainly rise. In that case, the static pressure throughout the subsonic stream will be close to the highest one occuring in the supersonic stream. That creates an interesting situation where the static pressures near the trailing edge cannot be matched in any way. The shear layer must therefore be curved near the trailing edge in order to support that pressure difference. This situation is evident in cases AA7 and HA10 from their sidewall pressure distributions (Figure 3.7) and from the Schlieren photograph of case AA7 (Figure 3.1(g)).

### 3.4. Velocity Profiles.

Due to the lack of concentration measurements, velocity profiles have been constructed from pitot pressure profiles and wall static pressure readings only for the homogeneous cases AA2, NN3 and AA7. Appendix C illustrates how sensitive the velocity profile of a

heterogeneous case is on the assumed density profile. In calculating the velocity profiles for the homogeneous cases, it is assumed that the turbulent Prandtl number is close to unity, therefore the total temperature is uniform throughout the flowfield. It is also assumed that the static pressure is constant across the layer. The accuracy of the above assumptions was not tested experimentally.

First, the Mach number distribution, M(y), is obtained from the pitot pressure distribution normalized by the local static pressure. For M(y)<1, the Rayleigh pitot formula

$$\frac{p_t'(y)}{p} = \left[\frac{\gamma+1}{2} M^2(y)\right]^{\frac{\gamma}{\gamma-1}} \left[\frac{\gamma+1}{2\gamma M^2(y) - (\gamma-1)}\right]^{\frac{1}{\gamma-1}} \quad , \quad M(y)>1 \tag{3.8}$$

is used, from which M(y) is obtained implicitly. For M(y)≤1, the probe now measures total pressure directly, so M(y) is given directly from the isentropic relation

$$M(y) = \left[\frac{2}{\gamma-1}\left(\left[\frac{p_t}{p}\right]^{\frac{\gamma-1}{\gamma}} - 1\right)\right]^{1/2} \quad , \quad M(y)\leq 1 \tag{3.9}$$

After M(y) is obtained, the velocity is calculated using the assumption that the total temperature is conserved:

$$U(y) = a_0 M(y) \left[1 + \frac{\gamma-1}{2} M^2(y)\right]^{1/2} \tag{3.10}$$

where $a_0$ is the ambient speed of sound.

The far-field velocity profiles of cases AA2, NN3 and AA7 are shown on Figure 3.8. Profiles obtained at other x-locations look very similar to the ones shown on Figure 3.8, so they are not included here.

A striking feature of the velocity profiles is the almost linear velocity distribution throughout most of the mixed region of the layer. That shape of the velocity profile causes the vorticity thickness

$$\delta_\omega = \frac{\Delta U}{\left(\frac{\partial u}{\partial y}\right)_{max}} \qquad (3.11)$$

to be a very large portion of the pitot thickness, $\delta_{pit}$. Indeed, measurements of $\delta_\omega$ at several x-locations for the three cases yield $\delta_\omega/\delta_{pit} \simeq 0.9$.

**3.5. Relations Among the Various Thicknesses.**

As mentioned in Section 3.1.2, the measurement of visual growth rate from the current Schlieren photographs is an inaccurate and subjective process. A more reliable and consistent alternative is the measurement of growth rate from the distribution of pitot thicknesses, as done in Section 3.2.1. It is desired here to examine the relations among pitot thickness, visual thickness, and vorticity thickness, the latter being defined by (3.11).

The visual thickness, although a subjective measurement, is useful in defining the extent of the region involved in the mixing. The same applies to the pitot thickness, which is the distance between two points in the pitot pressure profile very close to the freestream values (Figure 2.11). The vorticity thickness, on the other hand, is quite sensitive to the shape of the velocity profile and may not adequately describe the mixed region.

It has been customary to assume that $\delta_\omega = 0.5\delta_{vis}$. While this is valid for incompressible shear layers with uniform density, there is hardly any evidence to suggest that it holds for shear layers with density difference, let alone compressibility effects. The only known heterogeneous shear layer experiment where velocity profiles have been constructed, with the help of concentration measurements, is that of

Brown and Roshko [1974]. Their velocity profile for s=1/7 and r=0.13 looks very much like the present ones (Figure 3.8) in that it is nearly linear all the way to the edges of the layer. Their measurements of vorticity thickness in the heterogeneous cases are too few to make any quantitative conclusions. It is worth noting that in the s=1/7 case of Brown and Roshko, as well as in the current homogeneous cases (Section 3.4) the heavier fluid is on the high-speed side.

An attempt is made here to establish approximate relations among $\delta_{pit}$, $\delta_{vis}$, and $\delta_{\omega}$. For incompressible flow with uniform density, if we assume that the velocity profile is desribed by a simple hyperbolic tangent we get $\delta_{\omega}/\delta_{pit}=0.82$ for r=0 and 0.68 for r approaching 1, with $\delta_{pit}$ as defined in Figure 2.10(a). Since in this case $\delta_{\omega}/\delta_{vis}=0.5$, $\delta_{pit}/\delta_{vis}$ takes the values 0.61 for r=0 and 0.74 for r approaching 1. It should be noted that this is a theoretical result and that actual velocity profiles usually tend to deviate from such simple shapes, especially near the edges of the layer. For the different density case, Brown and Roshko [1974] provide pitot pressure, vorticity thickness and visual thickness data for s=7 and r=0.38. From those, we estimate that $\delta_{\omega}/\delta_{pit}=0.55$ and $\delta_{pit}/\delta_{vis}=0.95$, $\delta_{pit}$ being defined similarly to Figure 2.10(b).

For the compressible case, Sirieix and Solignac [1969] measured velocity profiles for a $M_1=3$, $M_2=0$ shear layer with air in both streams. Calculating the pitot pressure profile by a procedure opposite of that described in Section 3.4, we find that $\delta_{\omega}/\delta_{pit}=0.95$, a value similar to that obtained for the current velocity profiles.

The scarcity of experimental thickness data in heterogeneous incompressible and compressible shear layers undermines any further effort to develop more precise relations among the thicknesses. For the incompressible case, we will assume that $\delta_{pit}/\delta_{vis}=0.80$, a value between the theoretical one for hyperbolic tangent profile and the experimental one obtained from Brown and Roshko's measurements. For

uniform density, that relation translates to $\delta_{\omega}/\delta_{pit}=0.60$. For the compressible case, the evidence from the current velocity profiles and those of Sirieix and Solignac suggests that $\delta_{\omega}$, $\delta_{pit}$, and possibly $\delta_{vis}$, are nearly equal at high Mach numbers.

# Chapter 4
## The Convective Mach Number Concept

In investigating the effects of Mach number on the stability and growth rates of compressible shear layers, one would like to find a parameter that will correlate and unify the results for various flow conditions. In shear layers where $M_2=0$, for given stagnation conditions $M_1$ is itself such a parameter. Most compressible shear layer experiments in the literature belong to this category and the growth rate data indeed correlate well with $M_1$, as shown on Figure 15 of Brown and Roshko [1974]. However, in shear layers where the stagnation conditions are variable and $M_2 \neq 0$, as in the present experiments, the choice of the right parameters is not clear. The growth rate, $\delta'$, of a compressible, fully-developed turbulent shear layer can be generally expressed in terms of dimensionless parameters

$$\delta' = f \left( \frac{U_2}{U_1}, \frac{\rho_2}{\rho_1}, M_1, M_2, \gamma_1, \gamma_2 \right) \tag{4.1}$$

while for incompressible fully-developed turbulent shear layers it has been well established that their growth rate

$$\delta'_0 = f_0 \left( \frac{U_2}{U_1}, \frac{\rho_2}{\rho_1} \right) \tag{4.2}$$

One possibility is that

$$\delta' = f_0 \left( \frac{U_2}{U_1}, \frac{\rho_2}{\rho_1} \right) \; C \left( M_1, M_2, \gamma_1, \gamma_2 \right) \tag{4.3}$$

which implies that the velocity and density ratios act independently of the compressibility parameters. So far this is just speculation and is not supported by any analytical studies.

Clearly, a more analytical tool is needed for the investigation of compressibility effects. The simplest and most insightful way to approach the problem is to first examine a vortex sheet in compressible flow. Obviously, the vortex sheet itself cannot be compared quantitavely to the present shear layers but in analyzing it one finds parameters and trends that are very useful for understanding the behavior of more complex flows.

In this chapter, only two-dimensional disturbances are considered. Possible effects of three-dimensional disturbances are discussed in Section 5.4.

## 4.1. The Compressible Vortex Sheet.

The vortex sheet in an inviscid compressible flow was first analyzed by Landau [1944] and then by Hatanaka [1947], Pai [1954], Miles [1958] and others. The analyses of the above investigators focus on stability criteria and not on finding a compressibility-effect parameter in the sense described previously. The focus of the present analysis is the definition of such a parameter and the study of the dependence of amplification rates on that parameter as well as on other variables not related to compressibility, like the velocity ratio and the density ratio. The analysis presented below is that of a temporally developing vortex sheet and follows loosely that of Pai.

4.1.1. Fundamental Equation and Solutions. We consider a vortex sheet of shape $\eta = \eta(x,t)$ between two parallel streams in an infinite domain (Figure 4.1). The velocity potentials of the flows on both sides of the vortex sheet can be expressed as

$$\Phi_j = U_j\, x + \phi_j \qquad (4.4)$$

where j=1 refers to the fast stream and j=2 to the slow stream. $\phi_j$ is the perturbation velocity potential. From small perturbation theory, the differential equation that governs $\phi_j$ is

$$\frac{1}{a_j^2}\frac{D^2\phi_j}{Dt^2} = \frac{\partial^2\phi_j}{\partial y^2} + \frac{\partial^2\phi_j}{\partial x^2} \tag{4.5}$$

where

$$\frac{D}{Dt} = \frac{\partial}{\partial t} + U_j\frac{\partial}{\partial x}$$

We now assume that $\phi_j$ has the form

$$\phi_j = \psi(y)\, e^{i\alpha\,(x - ct)} \tag{4.6}$$

where $\psi(y)$ is the disturbance amplitude function, $\alpha$ is the disturbance wave number, taken to be real, and $c=c_r+ic_i$ is the complex phase velocity of the disturbance. We can rewrite (4.6) in the form

$$\phi_j = \psi(y)\, e^{\alpha c_i t}\, e^{i\alpha\,(x - c_r t)} \tag{4.7}$$

where $\alpha c_i$ is the temporal amplification rate. Substituting (4.3) into (4.2) we have

$$\frac{\partial^2\psi_j}{\partial y^2} - \alpha^2\,(1 - \mu_j^2)\,\psi_j = 0 \tag{4.8}$$

where

$$\mu_j = \frac{U_j - c}{a_j} = \frac{U_j - c_r}{a_j} - i\,\frac{c_i}{a_j} \tag{4.9}$$

It should always be kept in mind that $\mu_j$ is complex. The general solution of (4.8) is

$$\psi_j(y) = A_j\, e^{\alpha(1 - \mu_j^2)^{1/2}\, y} + B_j\, e^{-\alpha(1 - \mu_j^2)^{1/2}\, y} \qquad (4.10)$$

where $A_j$ and $B_j$ are constants to be determined by the boundary conditions. Equation (4.10) deserves close attention. To understand its nature, we must examine the regimes that the factor $1-\mu_j^2$ goes through as the flow conditions vary. For that, we go back to (4.9) and define

$$M_{c_j} = \frac{U_j - c_r}{a_j} \qquad (4.11)$$

$M_{c_j}$ is the Mach number in a frame of reference convecting with the real phase speed of the disturbances $c_r$. More simply, it is the Mach number "felt" by those disturbances. We call it the convective Mach number and its value may be different for each stream. Since $U_2<c_r<U_1$, (4.11) gives $M_{c_1}$ positive and $M_{c_2}$ negative. The fact that a Mach number is negative is nothing more than an artifact of the coordinate system, the low-speed flow moving from right to left in the convective frame of reference. Now we write

$$1 - \mu_j^2 = 1 - M_{c_j}{}^2 + \left[\frac{c_i}{a_j}\right]^2 + i\left[M_{c_j}\frac{c_i}{a_j}\right] \qquad (4.12)$$

In general, the behavior of (4.10) is an oscillation of exponentially amplifying or decaying amplitude. Examining (4.12) it becomes clear that the behavior of (4.10) is purely oscillatoty and the disturbances propagate unattenuated (radiate) away from the layer only when the imaginary term is zero and the real term is negative. Therefore, for $\psi_j(y)$ to be purely oscillatory, the following condition must be satisfied:

$$c_i = 0 \quad , \quad 1 - M_{c_j}{}^2 + \left[\frac{c_i}{a_j}\right]^2 < 0 \qquad (4.13)$$

From (4.10) it becomes obvious that (4.13) defines not only a radiation

condition for $\psi_j(y)$ but also complete stability for the vortex sheet. It is crucial to note that (4.13) is not generally satisfied when $M_{c_j}$ just exceeds 1 because at $M_{c_j}=1$ $c_i$ is still finite. As we will soon see, the vortex sheet is stable at values of $M_{c_j}$ usually considerably larger than 1. The convective Mach number beyond which the vortex sheet is stable is called here the critical convective Mach number and is denoted by $M_{c_j}^*$.

At this point it is useful to draw the distinctions between the present unsteady vortex sheet and the problem of a steady but flexible, wave-shaped surface of discontinuity between streams moving in opposite directions, first considered by Ackeret (Liepmann and Puckett [1947]). The latter situation is shown on Figure 4.2(a). The surface of discontinuity is stationary in a frame of reference moving with velocity $c_r$. In that frame of reference, the Mach numbers of the two streams are $M_{c_1}$ and $M_{c_2}$, as given by (4.11). For $M_{c_1}$ and $M_{c_2}$ both greater than 1, the pressures on both sides of the surface balance everywhere and the surface is neutrally stable (Figure 4.2(b)). When at least one of the Mach numbers is less than 1, the pressures cannot be balanced and the surface is unstable (Figure 4.2(c)). The above argument fails to predict the values of $M_{c_j}$ at which the vortex sheet becomes stable because it lacks the unsteady terms of (4.5). It is these unsteady terms that give rise to the complex nature of $\mu_j$ and thus alter Ackeret's simple picture. Nevertheless, Ackeret's argument provides some insight into the stability mechanism of the vortex sheet.

In the vortex sheet, a disturbance is classified as "supersonic", "sonic, or "subsonic" relative to a freestream velocity if its real phase speed with respect to that freestream velocity is greater than, equal to, or less than the local speed of sound. Thus, at side j of the vortex sheet a disturbance is supersonic if $M_{c_j}>1$, sonic if $M_{c_j}=1$,

and subsonic if $M_{c_j}<1$. It is possible that the same disturbance is supersonic with respect to one stream and subsonic with respect to the other.

In the past, there has been some confusion about the character of supersonic disturbances because arguments like that of Ackeret led to the misconception that supersonic disturbances are always associated with a stable vortex sheet. It is clear from (4.13) that this is not the case. In the regime $1<M_{c_j}<M_{c_j}^*$, the disturbances are supersonic but behave like subsonic ones in the sense that $\psi_j(y)$ decays or amplifies exponentially with y and the vortex sheet is unstable. It should be pointed out that the decay or amplification rate of disturbances with large $M_{c_j}$ (not necessarily larger than 1) is quite slower than that of low subsonic disturbances because the real part of (4.10) becomes smaller as $M_{c_j}$ increases.

4.1.2. Boundary Conditions and Eigenvalue Problem. The boundary conditions on the vortex sheet are:

(1) Disturbances at infinity must be finite.

(2) The velocity components of the fluid perpendicular to the vortex sheet are equal on both sides and equal to the motion of the vortex sheet itself in that direction.

(3) The pressures on both sides of the vortex sheet are equal.

The eigenvalue problem is obtained by applying the above boundary conditions to the perturbation potential (4.6) using the general solution (4.10). Boundary condition (1) dictates that $A_j=0$ in (4.10). Letting the shape of the vortex sheet be

$$\eta(x,t) = \eta_i \, e^{i\alpha (x - c\, t)} \tag{4.14}$$

and omitting the details, boundary conditions (2) and (3) give

$$\frac{\gamma_1 \, \mu_1^2}{(\mu_1^2 - 1)^{1/2}} = \frac{\gamma_2 \, \mu_2^2}{(\mu_2^2 - 1)^{1/2}} \tag{4.15}$$

Note that if $\mu_j$ were replaced by $M_{c_j}$ in (4.15), the pressure boundary condition for a flexible surface of discontinuity, described previously, would be obtained. So the eigenvalue equation (4.15) could be descriptively referred to as a pressure boundary condition defined by the "complex convective Mach numbers" $\mu_j$.

We rewrite (4.15) in the form

$$\mu_1^4 \, (1 - \mu_2^2) = \left|\frac{\gamma_2}{\gamma_1}\right|^2 \mu_2^4 \, (1 - \mu_1^2) \tag{4.16}$$

which, together with the definition of $\mu_j$ (4.9), can be solved for $c_i$ and $c_r$ in terms of the freestream conditions. Here, however, we wish to examine the variation of $c_i$ and $c_r$ with one of the convective Mach numbers $M_{c_j}$. We choose $M_{c_1}$ as the independent variable and we define non-dimensional phase velocities in the forms

$$\bar{c}_r = \frac{c_r - U_2}{U_1 - U_2} \tag{4.17}$$

and

$$\bar{c}_i = \frac{c_i}{U_1 - U_2} \tag{4.18}$$

The above definitions simplify the algebra considerably. Since

$U_2<c_r<U_1$, we must have $0<\bar{c}_r<1$. The notations $s=\rho_2/\rho_1$ and $r=U_1/U_2$ are used below. The pressures at the two sides of the vortex sheet being equal and $a^2=\gamma p/\rho$, we have

$$\frac{a_1}{a_2} = \left\{ s \frac{\gamma_1}{\gamma_2} \right\}^{1/2} \tag{4.19}$$

Using (4.17), (4.18) and (4.19) with (4.9), we express $\mu_1$ and $\mu_2$ in terms of $M_{c_1}$ :

$$\mu_1 = M_{c_1} \left\{ 1 - i \frac{\bar{c}_i}{1 - \bar{c}_r} \right\} \tag{4.20}$$

$$\mu_2 = M_{c_1} \left\{ s \frac{\gamma_1}{\gamma_2} \right\}^{1/2} \left\{ \frac{\bar{c}_r}{1 - \bar{c}_r} + i \frac{\bar{c}_i}{1 - \bar{c}_r} \right\} \tag{4.21}$$

Substituting (4.21) and (4.22) into (4.16), we solve (4.16) subject to the condition $0<\bar{c}_r<1$. We obtain three solutions of $\bar{c}_i$ and $\bar{c}_r$ in terms of $M_{c_1}$, s, and $\gamma_2/\gamma_1$. The three solutions correspond to damped, neutral and amplified disturbances. Here we are concerned only with the amplified solution. Note that the actual Mach numbers, $M_1$ and $M_2$, do not come into the picture. Knowing r, from (4.17) we calculate $c_i$ and $c_r$ normalized by any velocity we wish, thus $M_{c_2}$ is obtained from (4.11). We could have chosen $M_{c_2}$ as the independent variable and $M_{c_1}$ would have been obtained in a similar manner. The essential point is that either $M_{c_1}$ or $M_{c_2}$, which are compressibility-effect parameters, together with r, s ,and $\gamma_2/\gamma_1$, which are parameters not related to compressibility, uniquely define the state of the vortex sheet.

The same, of course, could be said for $M_1$: knowing $M_1$, r, s, and $\gamma_2/\gamma_1$, we can always calculate $M_2$, so $M_1$ could be used as a single compressibility parameter. The importance of $M_{c_1}$ as a

compressibility-effect parameter arises from the fact that it unifies the stability characteristics of a whole class of vortex sheets. As we will see, for s or 1/s not very large (say, $|\log(s)|<1$) and regardless of velocity ratio, the range of $M_{c_1}$ in which the vortex sheet becomes stable is roughly $1.2<M_{c_1}<2.5$, while $M_1$ could be range anywhere from zero to infinity. Therefore, $M_{c_1}$ is a more useful stability criterion and compressibility-effet parameter than $M_1$.

4.1.3. Discussion of Eigensolutions. The advantages of using $M_{c_1}$ as a compressibility-effect parameter become evident when the eigensolutions $\bar{c}_i$ and $\bar{c}_r$ are plotted versus $M_{c_1}$ for various values of s and $\gamma_2/\gamma_1$. This is done in Figures 4.3 through 4.6. The values of s are 0.1, 1, 10 and those of $\gamma_1/\gamma_2$ are 21/25, 1, 25/21 corresponding to combinations of monatomic and diatomic gases.

It is seen in Figures 4.3 and 4.4 that, for $M_{c_1}>0.5$, $\bar{c}_i$ declines sharply with increasing $M_{c_1}$ and vanishes at a value of $M_{c_1}$, centered around 1.4, that depends on s and $\gamma_2/\gamma_1$. In the range $0<M_{c_1}<0.5$, $\bar{c}_i$ decreases faster when the densities of the two fluids are similar than when they are very different Figure 4.3). Actually, for sufficiently large s or 1/s, $\bar{c}_i$ slightly increases at low values of $M_{c_1}$. Since $\bar{c}_i$ is proportional to the temporal amplification rate, the two sides of the vortex sheet are indistinguishable when $\bar{c}_i$ is related to the freestream conditions. Here, however, $\bar{c}_i$ depends on $M_{c_1}$, thus on which side has the larger density and the larger specific heat ratio. As a result, the curves of $\bar{c}_i$ versus $M_{c_1}$ become different when s and $\gamma_2/\gamma_1$ are replaced by their reciprocals, the difference accentuating as $\bar{c}_i$ vanishes. We remark that $\bar{c}_i$ is more sensitive to changes of $\gamma_2/\gamma_1$ (Figure 4.4) than to similar changes of s, something ignored in the existing compressible vortex sheet literature that deals only with equal specific heat ratio cases.

In Figure 4.5, the dependence of $\bar{c}_r$ on $M_{c_1}$ and s is shown for $\gamma_2=\gamma_1$. For uniform density and specific heat ratio, $\bar{c}_r$ is not affected by $M_{c_1}$ and has a value $\bar{c}_r=0.5$ which corresponds to $c_r = (U_1+U_2)/2$, that is, $c_r$ equals the average of the freestream velocities. When the freestreams have different densities, $c_r$ is closer to the speed of the heaviest gas, while the rise of $M_{c_1}$ results in $c_r$ moving toward the average velocity of the two streams. In Figure 4.6, the effect of $\gamma_2/\gamma_1$ on $\bar{c}_r$ is shown for the uniform density case where it is seen that $c_r$ slightly deviates from the average velocity of the two streams at high $M_{c_1}$. The calculation of $\bar{c}_r$ stops at $M_{c_1} = M_{c_1}^*$ because after that we get multiple solutions for $\bar{c}_r$ whose physical significance is not currently known.

For $\gamma_1=\gamma_2$, we obtain from (4.16) explicit solutions of $M_{c_j}^*$ in terms of s. Such stability relations, given in a different form, have been calculated by Landau and by Miles. We get

$$M_{c_1}^* = s^{-1/6}\left\{1 + s^{1/3}\right\}^{1/2} \tag{4.22}$$

and

$$M_{c_2}^* = -\left\{1 + s^{1/3}\right\}^{1/2} \tag{4.23}$$

As expected, when s is replaced by 1/s in (4.22) and (4.23) the expressions for $M_{c_1}^*$ and $-M_{c_2}^*$ are switched. For s=1 we have $M_{c_1}^*=-M_{c_2}^*=2^{1/2}$ which translates to $M_1=2^{3/2}$ when $M_2=0$. This is the well-known stability criterion for a homogeneous vortex sheet with one stream at rest, first formulated by Landau.

For $\gamma_2=\gamma_1$, the value of $\bar{c}_r$ at $M_{c_j} = M_{c_j}^*$ is

$$\bar{c}_r = \frac{1}{1 + s^{1/3}} \qquad (M_{c_j} = M_{c_j}^*) \tag{4.24}$$

It is interesting to compare that to the value of $\bar{c}_r$ for an incompressible vortex sheet

$$\bar{c}_r = \frac{1}{1 + s} \qquad (M_{c_j} = 0) \tag{4.25}$$

For $\gamma_2\neq\gamma_1$, we cannot get similar explicit expressions and the stability relations must be determined numerically. Based on the above, we can construct vortex sheet stability diagrams in terms of $M_{c_1}$, s, and $\gamma_2/\gamma_1$. These are shown on Figure 4.7. For $\gamma_2=\gamma_1$, $M_{c_1}^*$ tends to large values for s<<1, and approaches 1 for s>>1. For $\gamma_2/\gamma_1=25/21$, the trend is the same but $M_{c_1}^*$ approaches a value close to 2 for s>>1. For $\gamma_2/\gamma_1=21/25$, it appears that for s<<1 $M_{c_1}^*$ reaches an asymptote near 1.4. This behavior could be of interest in supersonic mixing of very heavy and light gases.

The temporal amplification rate, $\alpha c_i$, can be transformed into a spatial one by forming the ratio $\alpha c_i/c_r$. In the present unbounded vortex sheet, the disturbance wavelength cannot be related to any length scale because no other length scales exist. As a result, there are no eigenvalues for $\alpha$ and we can assign to $\alpha$ any value we wish. Here we take $\alpha = 1$. $c_i/c_r$ can be viewed as the transformed spatial amplification rate per unit wave number. It is related to the normalized phase velocities by

$$\frac{c_i}{c_r} = \frac{\bar{c}_i}{\bar{c}_r + \frac{r}{1-r}} \tag{4.26}$$

Thus, $c_i/c_r$ depends not only on s, $\gamma_2/\gamma_1$ and $M_{c_1}$ but also on r. A full parametric study of $c_i/c_r$ would be lengthy and would not add much to what is already known about $c_i$ and $c_r$. Here we investigate only the effects of $M_{c_1}$ and s, for $\gamma_2=\gamma_1$ and r=0. In Figure 4.8 we notice that s has a pronounced effect on the incompressible ($M_{c_1}=0$) amplification rate, something already known from the subsonic vortex sheet. The effect of compressibility becomes more clear when the amplification rates are normalized to be 1 at $M_{c_1}=0$ (Figure 4.9). We see that, as with $\bar{c}_i$, the decline of $c_i/c_r$ with increasing $M_{c_1}$ is faster for s>1 and slower for s<1. For small density ratios (s<0.3), $c_i/c_r$ actually increases near $M_{c_1}=0.4$ and then declines. Clearly, $c_i/c_r$ vanishes at the same value of $M_{c_1}$ that $c_i$ does. Therefore, although the $c_i/c_r$ versus $M_{c_1}$ curve depends on r, s, and $\gamma_2/\gamma_1$, the value of $M_{c_1}$ where the amplification rates become zero is independent of r.

Probably the most important point to make about the amplification rates is that they change gradually with $M_{c_1}$, something that Ackeret's argument cannot possibly predict. It is believed here that the decline of amplification rates, which starts at subsonic values of $M_{c_j}$, has to do with the distribution in y of the disturbance amplitude function, $\psi(y)$, ginen by (4.10), which is controlled by the comlex parameter $\mu_j$ given by (4.9). As $M_{c_j}$ increases, the real part of $\mu_j$ decreases until it becomes zero at $M_{c_j}=M_{c_j}^*$. Thus, the disturbances decay slower with y as $M_{c_j}$ increases. This may mean that less "energy" is left in the vicinity of the sheet that can be used for the excitation of the sheet itself. When $M_{c_j}$ exceeds $M_{c_j}^*$, all "energy" is radiated away from the sheet and the sheet cannot excite itself, thus remains stable. Here the term "energy" should be viewed as a measure of the magnitude of pressure fluctuations, the total energy of the system being constant.

This is only an intuitive explanation of the gradual decline of the amplification rates and by no means a rigorous one.

Finally, note should be made of the differences between temporal and spatial analyses. In the spatial analysis, the wave number is complex ($\alpha=\alpha_r+i\alpha_i$) while the frequency of oscillation ($\omega=\alpha c$) is real. The spatial amplification rate per unit wave number obtained by the spatial analysis ($-\alpha_i/\alpha_r$) is identical to the transformed spatial amplification rate obtained by the temporal analysis ($c_i/c_r$) when both quantities are related to the freestream conditions. On the other hand, the real phase velocity ($c_r$) given by the spatial analysis is quite different from that given by the temporal analysis, especially at low values of the velocity ratio. Therefore the $-\alpha_i/\alpha_r$ versus $M_{c_1}$ curve is different from the $c_i/c_r$ versus $M_{c_1}$ curve because $M_{c_1}$ depends on $c_r$. On the other hand, the value of $M_{c_1}^*$ is identical for both analyses since, by definition, both $-\alpha_i$ and $c_i$ vanish when the vortex sheet becomes stable. The temporal analysis has been stressed here because it closely resembles the treatment of the turbulent shear layer presented in Section 4.3.

## 4.2. Shear Layer of Finite Thickness.

Analytical investigations of the finite thickness, compressible shear layer have been very limited in the scientific literature. It is a problem full of mathematical complexities and the results obtained so far cannot be considerd very reliable. The linearized analysis of an inviscid, temporally developing, compressible shear layer has been carried out by Lin [1953] and Blumen et al. [1975], while the corresponding spatial analysis has been performed by Gropengiesser [1970]. It is not possible to list here every related work in the literature. The analyses of the above authors are in qualitative agreement with each other in that they predict a drastic reduction of amplification rates with increasing Mach number. Quantitative comparisons are difficult to make because of the variety of assumptions and notations each work

uses.

No attempt is made here to develop an analytical model for the stability of the compressible shear layer. Instead, a conceptual model will be outlined, using what is already known for the compressible vortex sheet and some fundamental results of the aforementioned analyses.

Contrary to the discontinuous nature of the vortex sheet, in a shear layer of finite thickness the velocity, density, temperature and specific heat ratio vary gradually across the layer. This gives rise to $\partial u/\partial y$, $\partial \rho/\partial y$, $\partial T/\partial y$, and $\partial \gamma/\partial y$ terms that make the perturbation equation much more complex than that used with the vortex sheet. Furthermore, there are no static pressure and velocity equality boundary conditions, like those applied to the vortex sheet, because no distinct interface exists between the two fluids. The only boundary condition here is that disturbances are finite at infinity. Most important, since the velocity varies gradually across the layer, parts of the same layer can exhibit different behavior as to how disturbances propagate through them.

For a temporally developing layer, the disturbance can be given in a wave-form equation, similar to that used with the vortex sheet:

$$Q' = q(y)\, e^{i\alpha(x - ct)} \tag{4.27}$$

with $\alpha$ real and $c=c_r+ic_i$ complex. Here Q' is the disturbance value of the mean flow parameter Q, and q(y) is its amplitude function. Q represents the mean values of the horizontal and vertical velocity components, density, pressure, and temperature.

In defining the convective Mach numbers of the shear layer, we distinguish between the freestream convective Mach numbers and the local convective Mach number. The freestream convective Mach numbers, defined similarly to those of the vortex sheet, are given by (4.11)

where $U_j$ and $a_j$ are the freestream values of the velocity and speed of sound respectivelly. The local convective Mach number is a function of y and is given by

$$M_c(y) = \frac{u(y) - c_r}{a(y)} \tag{4.28}$$

where u(y) is the local mean velocity and a(y) the local mean speed of sound. Clearly, at the edges of the shear layer $M_c(y)$ takes the freestream values $M_{c_1}$ and $M_{c_2}$. Further relations for $M_{c_1}$. $M_{c_2}$ and $M_c(y)$ cannot be obtained until the complete eigenvalue problem is solved. We do expect, however, that $M_{c_1}$ will uniquely characterize the compresibility of the flow and in that respect will unify the results, at least for s or 1/s not very large.

We classify a local disturbance at some y-location of the layer as subsonic, sonic, and supersonic, depending on whether $|M_c(y)|$ is less than, equal to, or greater than 1. To clarify this classification, we consider a shear layer with $M_{c_1}>1$ and $M_{c_2}>1$. It is shown on Figure 4.10(a) in a stationary frame of reference. Figure 4.10(b) depicts the same shear layer in a frame of reference moving with velocity $c_r$. The intersections of $u(y)-c_r$ with $\pm a(y)$ define the boundaries between sublayers where disturbances are subsonic or supersonic. The subsonic sublayer is centerd around the y-location where $u(y)=c_r$, while the supersonic sublayer is located outside the subsonic one and extends to the edges of the shear layer.

As $M_{c_1}$ (or $M_{c_2}$) increases, the subsonic sublayer shrinks but never quite vanishes. Therefore, subsonic disturbances will always exist regardless of how large $M_{c_1}$. This is an important distinction from the vortex sheet where for sufficiently high $M_{c_1}$ only supersonic disturbances exist. It is thus likely that the finite thickness shear layer

will in general be unstable at any value of $M_{c_1}$. On the other hand, we might expect that, as in the vortex sheet, the disturbances will decay slower, or possibly amplify, with y as $M_{c_1}$ increases. Since that appears to be the fundamental reason for the amplification rate decline in the vortex sheet, we conjecture that the amplification rate of the shear layer will also decrease with increasing $M_{c_1}$, starting at subsonic values of $M_{c_1}$.

The above features of this crude conceptual model are in line with the analytical results of Blumen et al. and Gropengiesser. Both analyses find that the amplification rates are drastically reduced with increasing Mach number, starting at subsonic Mach numbers, but never become zero, no matter how large the Mach number. One of Gropengiesser's results is plotted on Figure 4.11, showing the spatial amplification rate $-\alpha_i$ versus $M_1$ in a one-stream ($M_2$=0) shear layer with uniform density and specific heat ratio. Notable is the flattening of the $-\alpha_i$ curve at high Mach numbers. Gropengiesser has also computed the effect of density ratio on amplification rates and finds the same trend as in the vortex sheet, i.e., the rise of Mach number has a greater stabilizing effect for large density ratios (s>1) than for small ones (s<1). His results, however, show an excessive sensitivity of amplification rates on density ratio, especially at $M_1$=0. This is in disagreement with results of incompressible heterogeneous shear layer stability analysis (Maslowe and Kelly [1971]) and casts doubt on the quantitative reliability of Gropengiesser's computations.

### 4.3. Turbulent Shear Layer.

It is clear that the results of the linearized stability analysis for a finite thickness shear layer cannot be directly applied to the turbulent case, since the disturbances now have finite amplitude and linearization is not possible. A direct solution to the problem, using the full Navier-Stokes equations, is an enormous task which, to our knowledge, has not been attempted so far. Using the Reynolds time-

averaged equations of motion may be a simpler approach, but reliable models for the various correlation terms must first be invented.

Here we are not so much concerned with the exact solution to the compressible shear layer problem, as with the choice of a suitable coordinate system in which to view the flow. In subsonic shear layers, the discovery of organized large structures led to the idea that such a coordinate system is one moving with the structures. The term "celerity" has been used by Favre and Kovasznay to define the velocity of the moving frame in which the large structure is most nearly stationary.

Since large structures are also present in compressible shear layers, a frame of reference moving with $U_c$, where $U_c$ is the velocity of the dominant waves and structures, is a reasonable choice for a coordinate sysyten in which the intrinsic properties of the flow are investigated. Accordingly, we define the convective Mach numbers of a turbulent shear layer in the following fashion:

$$M_{c_1} = \frac{U_1 - U_c}{a_1} \tag{4.30}$$

$$M_{c_2} = \frac{U_c - U_2}{a_2} \tag{4.31}$$

With this definition, since $U_2<U_c<U_1$, both convective Mach numbers are now positive.

The fact that large-scale structures dominate the development of the turbulent shear layer (Figure 4.12(a)), helps in formulating a pressure boundary condition, in a way similar to the static pressure boundary condition of the vortex sheet, by which the convective velocity $U_c$ is calculated. This boundary condition is implicit in Cole's [1981] sketches of streamlines in the moving coordinates of the large structures (Figure 4.12(b)), and was first suggested to us by Dimotakis

[1982]. In this coordinate system, there is a saddle point between the structures; it is a common stagnation point for both streams, thus implies equality of total pressures in the two streams in that system. For equal static pressures this results in

$$\left[1 + \frac{\gamma_1 - 1}{2} M_{c_1}^2\right]^{\frac{\gamma_1}{\gamma_1 - 1}} = \left[1 + \frac{\gamma_2 - 1}{2} M_{c_2}^2\right]^{\frac{\gamma_2}{\gamma_1 - 1}} \tag{4.32}$$

This result has been obtained by Bogdanoff [1981] using a slightly different argument. It should also be noted that Oertel [1982] has obtained excellent experimental evidence supporting the concept of large coherent structures and associated convective velocities in supersonic shear layers.

For $M_{c_1}$ and $M_{c_2}$ not very high and $\gamma_1$ and $\gamma_2$ not substantially different, (4.32) can be approximated by

$$M_{c_2} = \left[\frac{\gamma_1}{\gamma_2}\right]^{1/2} M_{c_1} \tag{4.33}$$

which, together with (4.30), (4.31) and (4.19), gives

$$\frac{U_c}{U_1} = \frac{1 + r\, s^{1/2}}{1 + s^{1/2}} \tag{4.34}$$

For $\gamma_1 = \gamma_2$, $U_c$ can be expressed in the form

$$U_c = \frac{a_2 U_1 + a_1 U_2}{a_1 + a_2} \tag{4.35}$$

which has the form of a speed-of-sound weighted average. It should be noted that (4.34) and (4.35) are not restricted to compressible flow and are actually more accurate for incompressible flow.

$M_{c_1}$ and $M_{c_2}$ are slightly different when $\gamma_1$ =7/5 and $\gamma_2$=5/3 or the reverse. Figure 4.11 shows the dependence of $M_{c_1}$ on $M_1$ and $M_2$ for various gas combinations. $M_{c_1}$ has been calculated for uniform total temperature using (4.30) and (4.34). The error that results from using (4.33) instead of (4.32) is very small for the range of $M_{c_1}$ plotted on Figure 4.11, and is obviously zero for $\gamma_1=\gamma_2$.

As in Section 4.2, we define a local convective Mach number

$$M_c(y) = \frac{| u(y) - U_c |}{a(y)} \tag{4.36}$$

where u(y) and a(y) are the mean local values of velocity and speed of sound. Accordingly, we classify a disturbance as subsonic, sonic, or supersonic depending on whether $M_c(y)$ is less than, equal to, or greater than 1. A shear layer with $M_{c_j}>1$ is thus divided into supersonic and subsonic regions according to Figure 4.8(b), with $c_r$ replaced by $U_c$.

Having defined the convective Mach numbers of the turbulent shear layer, we hypothesize that (4.1) can be reduced to

$$\delta' = f\left( \frac{U_2}{U_1}, \frac{\rho_2}{\rho_1}, \frac{\gamma_2}{\gamma_1}, M_{c_1} \right) \tag{4.37}$$

i.e., the compressibility effects can now be expressed in a single parameter, $M_{c_1}$. The above parameters (enclosed in the parentheses of (4.37)) uniquely define the freestream conditions of the layer. The choice of $M_{c_1}$ or $M_{c_2}$ as a compressibility-effect parameter is not critical since the relation between the two is known from (4.33) and the two are not very different anyway.

With the statement of (4.37) in mind, we proceed to calculate the convective Mach numbers of the shear layers established in the current facility. The calculation, which uses (4.30), (4.31) and (4.34), is based on the freestream conditions at the region of turbulent growth rate measurement. The convective Mach numbers are shown on Table 4.1. For completeness, most of the information of Table 2.3 is reproduced here.

Table 4.1. Convective Mach Numbers

| Case | Gas 1 | $M_1$ | Gas 2 | $M_2$ | $M_{c_1}$ | $M_{c_2}$ | $\frac{\rho_2}{\rho_1}$ | $\frac{U_2}{U_1}$ | $\frac{\gamma_2}{\gamma_1}$ |
|---|---|---|---|---|---|---|---|---|---|
| AN1 | Ar | 1.6 | $N_2$ | 3.3 | 0.07 | 0.08 | 4.4 | 0.93 | 0.84 |
| AA2 | Ar | 3.4 | Ar | 1.8 | 0.26 | 0.26 | 0.43 | 0.81 | 1 |
| NN3 | $N_2$ | 3.1 | $N_2$ | 1.7 | 0.33 | 0.33 | 0.54 | 0.74 | 1 |
| NA4 | $N_2$ | 2.8 | Ar | 2.6 | 0.39 | 0.36 | 1.8 | 0.75 | 1.19 |
| NA5 | $N_2$ | 3.2 | Ar | 2.1 | 0.55 | 0.51 | 1.2 | 0.67 | 1.19 |
| HN6 | He | 1.7 | $N_2$ | 3.0 | 0.64 | 0.69 | 9.2 | 0.52 | 0.84 |
| AA7 | Ar | 3.1 | Ar | 0.2 | 0.89 | 0.89 | 0.24 | 0.13 | 1 |
| HN8 | He | 2.6 | $N_2$ | 2.8 | 1.05 | 1.15 | 5.5 | 0.42 | 0.84 |
| HN9 | He | 3.4 | $N_2$ | 1.6 | 1.44 | 1.57 | 2.2 | 0.29 | 0.84 |
| HA10 | He | 3.1 | Ar | 0.3 | 1.81 | 1.81 | 2.4 | 0.04 | 1 |

The so-far obscure designations of the experimental cases according to degree of compressibility now become clarified since they are based on the value of $M_{c_1}$. The implications of using $M_{c_1}$ as a compressibility-effect parameter become evident when we examine Table 4.1. It is seen that $M_1$ and $M_2$ alone provide little information about how compressible the flow is. For example, in case AN1, $M_1$ and $M_2$ are both supersonic and quite different from each other but $M_{c_1}$ is nearly

zero, implying that the flow is essentially incompressible. On the other hand, in case HN8 $M_1$ and $M_2$ are nearly equal but $M_{C_1}$ is quite large, suggesting large effect of compressibility. Finally, in case HA10 one stream is subsonic, yet $M_{C_1}$ is larger than in all the others. In that respect, there is no fundamental difference between a shear layer consisting of two supersonic streams and one consisting of a supersonic and a subsonic stream.

The usefulness of $M_{C_1}$ in correlating the experimental results will be tested in the next chapter.

# Chapter 5
# The Isolated Effect of Compressibility

Now that a compressibility-effect parameter has been defined in the name of the convective Mach number which, we hypothesize, describes the intrinsic compressibility of the shear layer, we proceed to correlate the experimental results with it. If we somehow fix all other relevant parameters and vary the convective Mach number only, we can estimate the isolated effect of compressibility on the experimental measurements.

## 5.1. Turbulent Growth Rates.

5.1.1. Uncoupling the Effect of Convective Mach Number. Assuming that the turbulent growth rate is generally correlated by (4.37), we see that there are two parameters besides $M_{c_1}$ that play an important role in the growth rate, namely the velocity ratio and the density ratio. As for $\gamma_2/\gamma_1$, since it already plays a role in the determination of the convective Mach numbers (equation (4.33)), we assume that its other possible effects are negligible compared to those of r and s. If we go ahead and plot the experimental growth rates versus $M_{c_1}$ without taking into account the effects of r and s, we obtain an inconclusive trend shown on Figure 5.1. That trend shows the growth rates actually increasing at high $M_{c_1}$, something that contradicts the expectation supported by previous experimental works that compressibility has a stabilizing effect. This illustrates the need to uncouple the effects of $M_{c_1}$ from those of r and s.

Such uncoupling is easier for the previous experimental works where $M_2=0$ (r=0) and both gases are air, the only parameter varying besides $M_{c_1}$ being s. Yet, the growth rate-Mach number correlations done in the past, like those of Birch and Eggers [1972] and Bogdanoff

[1982], consistently fail to allow for density ratio effects. It is known from subsonic experiments (Brown and Roshko [1974]) that shear layers with fixed r grow faster when s<1 and slower when s>1. In the above experiments, the freestream at high Mach number is much cooler than the stream at rest, thus s is quite high. As a result, the shear layer would grow more slowly even if it were incompressible at the same density ratio. The above correlations, therefore, overestimate the stabilizing effect of Mach number by as much as a factor of 2.

A simple way to estimate the net effect of $M_{c_1}$ is to compare the experimentally measured growth rates with those that would have occured if the flow were incompressible and the velocity and density ratios were kept unchanged. More specifically, we form the ratio

$$\frac{\delta'}{\delta'_0} = \frac{f\,(\,r,\ s,\ M_{c_1}\,)}{f\,(\,r,\ s,\ M_{c_1}=0\,)} \tag{5.1}$$

which will give the isolated effect of $M_{c_1}$ <u>at particular values of velocity ratio and density ratio</u>.

5.1.2. <u>A Model for the Incompressible Growth Rate</u>. In order to normalize the growth rate according to (5.1), we need an approximate model for the growth rate of the incompressible shear layer over a wide range of r and s. In creating such a model, we assume that the main effect of the density ratio is to determine the convective velocity of the structures $U_c$ as given by (4.34). We conjecture that in a frame of reference moving with $U_c$ the growth rate is simply proportional to $\Delta U = U_1 - U_2$. thus the density ratio drops out of the picture in that frame. We thus arrive at the very simple expression

$$\delta'_0 \sim \frac{\Delta U}{U_c} \tag{5.2}$$

which can be compared to the spatial growth rate of a temporally

developing vortex sheet $c_0/c_r$, the major difference being that $c_0/\Delta U$ weakly depends on density ratio. For uniform density (s=1), from (4.34) we have $U_c=(U_1+U_2)/2$ and (5.2) takes the familiar form

$$\delta'_0 \sim \frac{U_1 - U_2}{U_1 + U_2} \tag{5.3}$$

For visual thickness, (5.2) becomes, using (4.34)

$$(\delta'_{vis})_0 = 0.17 \frac{\Delta U}{U_c} = 0.17 \frac{(1 - r)(1 + s^{1/2})}{1 + r\, s^{1/2}} \tag{5.4}$$

the constant 0.17 having been obtained experimentally by Brown and Roshko [1974]. A generalized version of (5.4), obtained by similar arguments, was first proposed by Brown [1974] who suggests that the exponent of s in (5.4) is variable, ranging between 0.5 and 0.6. Dimotakis [1984] uses geometrical arguments to derive the entrainment and growth of the turbulent region and comes up with an expression for the growth rate quite similar to (5.4). Bogdanoff [1984] also proposes (5.2) without giving any specific arguments.

Although the present derivation of (5.4) is hardly based on rigorous arguments, its growth rate prediction is in surprisingly good agreement with experimentally observed growth rates of subsonic shear layers, as shown in Figure 5.2.

To compare with the present results of pitot thickness growth, we assume that $(\delta'_{pit})_0=0.80(\delta'_{vis})_0$, a relation suggested in Section 3.5. From (5.4) we have

$$(\delta'_{pit})_0 = 0.14 \frac{(1 - r)(1 + s^{1/2})}{1 + r\, s^{1/2}} \tag{5.5}$$

5.1.3. The Normalized Growth Rate. The ratio $\delta'_{pit}/(\delta'_{pit})_0$, called here the "normalized growth rate", is now formed according to (5.5), where $\delta'_{pit}$ is the experimentally obtained growth rate and $(\delta'_{pit})_0$ is the incompressible visual growth rate, obtained from (5.3), at the same r and s as the experimental one. The normalized growth rate is plotted versus $M_{c_1}$ in Figure 5.3. This is probably the most important result of this research project and illustrates the advantages of $M_{c_1}$ as a compressibility-effect parameter, as well as the usefulness of the growth rate normalization according to (5.1). We first note that all the normalized growth rates obtained here collapse roughly onto one curve, despite the wide variation of density ratio from one case to the other. For example, case HN6 ($M_{c_1}$=0.64) has s=0.24 and case AA7 ($M_{c_1}$=0.89) has s=9.2, yet they both have approximately the same $\delta'_{pit}/(\delta'_{pit})_0 \simeq 0.22$. In the vortex sheet, such variation of s would have significantly altered the effectiveness of the $M_{c_1}$ in reducing the growth rate (Figure 4.9). In the turbulent shear layer, however, it appears that that effectiveness is less sensitive to variations of s and, for that matter, variations of r and $\gamma_2/\gamma_1$. This suggests that the growth rate of a compressible shear layer might be generally expressed in the form of (4.3), that is,

$$\frac{\delta'}{\delta'_0} \simeq C(M_{c_1}) \tag{5.6}$$

where C is a universal function valid over a wide range of r and s. We must be cautious about such a statement, however, in view of the limited number of measurements and the experimental error involved. The accuracy of the incompressible model of the shear layer must also be taken into consideration.

The most striking feature of Figure 5.3 is the drastic reduction of the normalized growth rate with increasing $M_{c_1}$, until $M_{c_1}$ reaches

about 0.8. Beyond that point, it stays fairly constant, at a value approximately one fourth of the incompressible one. The apparent complete flattening of the normalized growth rate curve for $M_{c_1}>1$, implying independence of growth rate from $M_{c_1}$ for $M_{c_1}>1$, is a little surprising because there is no obvious reason why it should occur. On the other hand, it is interesting to note that Gropengiesser's computations do predict such a leveling off of amplification rates at high Mach numbers (Figure 4.11). It is possible that the normalized growth rate does decrease with increasing $M_{c_1}$ for $M_{c_1}>1$, but that decrease is so slow that it is covered up by experimental error.

Another important feature of Figure 5.3 is that the normalized growth rate decreases gradually with increasing $M_{c_1}$, starting at subsonic values of $M_{c_1}$. This contradicts some earlier ideas that the decline of growth rate would come abruptly, immediately after some relative Mach number becomes supersonic (Cosner [1976]). That gradual decline is in line with results of the vortex sheet analysis and shear layer computations of Blumen et al. [1975] and Gropengiesser [1969] (Figure 4.11). The fundamental reason for it occuring, even at subsonic values of $M_{c_1}$, is believed here to be similar to that proposed for the vortex sheet: as $M_{c_1}$ increases, the disturbances decay away from the layer more slowly, thus there is less potential for excitation left in the vicinity of the layer. The uncertain visual definition of the edges of the layer at high $M_{c_1}$, as noted in Section 3.1.2, may be an indication that disturbances do indeed decay slower with increasing $M_{c_1}$.

Assuming that (5.4) is approximately valid, at a given value of $M_{c_1}$ the effects of density ratio and velocity ratio on the growth rate are similar to those in an incompressible shear layer, given by (5.4):

the growth rate is smaller when the heavier gas is on the high-speed side and greater when the heavier gas is on the low-speed side; the growth rate increases with decreasing velocity ratio, i.e., with increasing freestream velocity difference.

The same type of correlation used with the present growth rates can be applied to the growth rates measured by previous investigators. The experimental data are taken from Maydew and Reed [1963], Ikawa and Kubota [1975], Sirieix and Solignac [1966], and Birch and Eggers [1973]. All these investigators have performed probe measurements of vorticity thickness ($\delta_\omega$) in shear layers with $M_2$=0 and both gases air. We form the ratio $\delta'_\omega/(\delta'_\omega)_0$ using (5.3) with the constant changed to 0.085. That change stems from the fact that in incompressible homogeneous shear layers the vorticity thickness is about half of the visual thickness (Brown and Roshko [1974]). There is little evidence, however, to suggest that the same relation holds for layers with density difference, as discussed in Section 3.5. The result is shown on Figure (5.4), where it is seen that the normalized growth rate versus $M_{c_1}$ exhibits the same qualitative behavior as the current one. Quantitatively, the major difference is that the leveling off of the curve at $M_{c_1}>1$ occurs at a normalized growth rate around 0.4, as opposed to 0.2 in the present experiments. That discrepancy probably arises from the fact that the ratio $\delta_\omega/\delta_{pit}$ may be a function of density ratio and freestream Mach number, as pointed out in Section 3.4. A value of $\delta_\omega/\delta_{pit}$=0.9, obtained from the current velocity profiles, at the large Mach number cases ($M_{c_1}>1$) would reconcile the two curves to some extent.

## 5.2. Transition Results.

It was found in Section 3.1.4 that the shear layer transition Reynolds number, $Re_{x_{tr}}$, (based on the properties of the high Re' stream and the distance to transition) is roughly $2\times10^5$ for cases NA4 and HN8. Also, $x_{tr}/\theta$ (based on the smaller $\theta$) is 670 for case NA4 and 720 for

case HN8. It is thus apparent that $Re_{x_{tr}}$ and $x_{tr}/\theta$ are insensitive to rather large changes of $M_{c_1}$, from $M_{c_1}$=0.39 (case NA4) to $M_{c_1}$=1.05 (case HN8). This is a little surprising since it is expected that the increase of $M_{c_1}$ will stabilize the flow, as found for the growth rates. One explanation may be that the transition process is wake-dominated, in which case the actual freestream Mach numbers, $M_1$ and $M_2$, may be more important than $M_{c_1}$. This observation is supported by experimental work of Shackleford et al. [1973]: they found that the distance to transition in a shear layer composed of alternatively heated $N_2$ streams, both at M=4, is independent of the velocity ratio which ranges between 0.4 and 1. In their case, this corresponds to $M_{c_1}$ ranging from 0 to 0.8.

Demetriades and Brower [1982] have conducted instantaneous hot film measurements in the transition region of a shear layer composed of air at M=3.0 and air at M=2.2. They quote a value of $Re_{x_{tr}}$ ranging between $1.2 \times 10^5$ to $3.5 \times 10^5$, with a corresponding value of $x_{tr}/\theta$ ranging between 250 and 700. The reason for that wide range of $x_{tr}$ stems primarily from the fact that in attempting to apply their theory to experimental results, they use the Reynolds number based on local layer thickness as their transition criterion. Given the extremely small growth rates, any uncertainty in defining the transition thickness of the layer translates into an order-of-magnitude greater uncertainty in defining $x_{tr}$. This illustrates the limited usefulness of a transition criterion based on layer thickness. Also, the physical significance of such a criterion becomes small when one considers the transition process as an inviscid one, thus scaling with initial conditions (Roshko and Lau [1965]). The transition experiments of Demetriades and Brower are likely to apply to a wake, rather than to a shear layer, since the velocity ratio is 0.9 and their measurements are made in the near field.

It is believed here that if the wake effect were negligible, the distance to transition, scaled by the initial conditions, and the transition Reynolds number would increase markedly with increasing convective Mach number. In a fixed experimental configuration, however, it is difficult to minimize the effect of the wake because in extending the distance to transition far downstream by lowering the pressure, the trailing-edge boundary layers become thicker, thus the wake extends further downstream. The effect of initial conditions on transition of incompressible shear layers has been the topic of extensive investigations by Roshko and Lau [1965] and Breidenthal [1981].

### 5.3. Large-Scale Structures..

A plot of structure spacing to visual thickness ratio, $\ell/\delta_{pit}$, versus $M_{c_1}$ is shown on Figure 5.5. It is seen that for $M_{c_1}<1$, $\ell/\delta_{pit} \simeq 2.2$, which is a typical value for incompressible shear layers. For $M_{c_1}>1$, the ratio decreases to $\ell/\delta_{pit} \simeq 1.2$. This suggests that the lateral extent of the shear layer where large-scale structures can form lessens as $M_{c_1}$ increases beyond some critical value. The above trend could be explained by the fact that as $M_{c_1}$ increases beyond 1, the subsonic sublayer, described in Section 4.2, occupies a smaller portion of the extent of the mixing region. It is thus implied that somehow vortical structures prefer to form in a "subsonic" environment, something that so far is very speculative.

### 5.4. Possible Effects of Oblique Disturbances.

So far, the analyses and discussions in Chapters 4 and 5 have been limited to two-dimensional disturbances. It is possible that oblique disturbances, i.e., disturbances that propagate at an angle $\beta$ to the mean flow direction, exist in compressible shear layers. Unfortunately, the possible presence of such disturbances in the present shear layers could not be detected with the existing diagnostics.

In the analytical works of Gropengiesser [1970] and Lessen et al. [1965] it is found that the shear layer becomes more unstable as $\beta$ increases. Bogdanoff [1981] proposes that in turbulent shear layers the effect of $\beta$ can be taken into account by defining an effective convective Mach number

$$M_{c_{1,eff}} = M_{c_1} \cos\beta \tag{5.5}$$

in which case the result shown on Figure 5.3 would be invariant with $\beta$ as long as it is plotted against $M_{c_{1,eff}}$. If (5.5) indeed holds, it is easy to see that for $\beta$ to have a significant effect it must be greater than about 30 degrees, otherwise its effect could be easily covered up by experimental error of the order of ±5%. We also note that the effect of obliquity on the growth rate would be more pronounced for $0<M_{c_1}<1$, where the growth rate decreases drastically with increasing $M_{c_1}$, than for $M_{c_1}>1$, where the growth rate changes slightly with $M_{c_1}$.

The visualization of large-scale structures in most current Schlieren photographs is a strong indication that these structures are basically two-dimensional. This, however, does not preclude the existence of smaller, three-dimensional disturbances that are superimposed on the larger ones. Actually, it is well known that such small structures exist in subsonic shear layers, although the primary structure is coherent spanwise (Konrad [1977], Breidenthal [1981]). Their potential effect on the development of the compressible layer is not currently known.

# Chapter 6
# Conclusion

A parametric study of supersonic shear layers has been carried out in which the freestream Mach numbers range from 0.2 to 4. the density ratio varies from 0.2 to 9.2. and the velocity ratio varies from 0.13 to 1. The emphasis of this investigation was upon determining the effect of compressibility on the properties of the shear layer, especially on the turbulent growth rate. The growth rate is based on the width of pitot-pressure profiles obtained at several streamwise locations. The Mach number in a frame of reference moving with the convective velocity of the dominant waves and structures, called the convective Mach number, is defined as a compressibility-effect parameter which correlates and unifies the experimental results. The effects of compressibility on other aspects of the flow, such as the large-scale structures of the layer, the transition from laminar to turbulent flow, the velocity profiles, and the streamwise pressure gradient, are also investigated.

## 6.1. Summary of Results.

(a) The growth rate of the turbulent region of the shear layer decreases drastically with increasing convective Mach number. That decrease is gradual, starting at low subsonic values of the convective Mach number, and tapering off as the convective Mach number becomes supersonic. The growth rate at supersonic values of the convective Mach number is about one fifth that of an incompressible shear layer with the same ratios of densities and velocities. The gradual thinning of the growth rate is in qualitative agreement with results of linear stability analyses of the vortex sheet and the finite thickness layer, as well as with previous experimental results of other investigators.

(b) Given a fixed convective Mach number, the effects of density and velocity ratios on the growth of the turbulent compressible shear layer are similar to those in an incompressible shear layer: at a fixed value of the velocity ratio, the layer spreads faster when the heavy gas is on the low-speed side and slower when the heavy gas is on the high-speed side; at a fixed value of the density ratio, the spreading rate increases with decreasing velocity ratio, i.e., with increasing velocity difference with respect to one of the freestream velocities.

(c) Large-scale structures, reminiscent of those observed in subsonic shear layers, are evident in the visual observation of compressible shear layers. The spacing of the structures, normalized by the pitot thickness, appears to be reduced by about 50% as the convective Mach number becomes supersonic. It is conjectured that large-scale motions are more likely to take place in the subsonic part of the layer, i.e., in the region where the convective velocity of the structures is subsonic with respect to the local mean velocity, rather than in the supersonic region.

(d) The distance to transition, $x_{tr}$, has been estimated visually for two shear layers composed of different gases, with both gases at M=3. The shear layers have widely different convective Mach numbers, one low subsonic and the other sonic. It is found that $Re_{x_{tr}}$ and $x_{tr}/\theta$ ($\theta$ being the smaller of the two initial boundary-layer momentum thicknesses) are about the same in both cases, having the approximate values of $2 \times 10^5$ and 700, respectivelly. It is conjectured that the transition process is wake-dominated, in which case the freestream Mach numbers may play a more important role than the convective Mach number.

(e) An adverse streamwise pressure gradient, taking place mostly near the trailing edge, was present at various intensities in all the current shear layer configurations. It is primarily caused by the fact that mixing produces entropy, the actual pressure rise mechanism being

a positive displacement thickness of the shear layer. The streamwise pressure rise is an inherent feature of shear layers with at least one high-Mach number stream.

(f) Velocity profiles for the homogeneous cases are remarkably full, the velocity distribution being nearly linear all the way to the edges of the shear layer. It appears that the Mach number, as well as the density ratio, contribute in that fullness of the velocity profile.

(g) A wake flow, established by mixing different gases at different Mach numbers but equal velocities, appears to grow according to laws established for subsonic wakes with uniform density.

**6.2. Suggestions for Further Work.**

It would be interesting to find how the trend of decreasing growth rate with increasing convective Mach number continues past the highest current value. To accomplish that, shear layers with one stream at very high Mach number and large density ratio must be generated, in which case the adverse pressure gradient may be so strong that it will cause a sharp reduction in the downstream value of the Mach number. It would be useful to see if experimental configurations are possible where the onset of adverse pressure gradient is delayed so that the high freestream Mach number is sustained over a long extent of the shear layer.

It may be desirable to study more extensively the effect of density ratio on the stability and growth rate of the shear layer at high convective Mach numbers. The effect of waves impinging on the shear layer could be investigated more quantitatively by generating waves of controlled strength in the test section.

A great deal of information would be provided by comprehensive instantaneous measurements in the transitional and turbulent regime. Such measurements could shed a lot of light on the so-far sketchy

picture of stability and mixing properties of the compressible shear layer.

Finally, a parametric stability analysis of the compressible shear layer would broaden our knowledge and understanding of the intricate features of that flow. It would be highly desirable for such an analysis to examine the effect of compressibility combined with the effects of density, specific heat ratio and velocity ratio.

# Appendix A

## Foelsch Supersonic Nozzle Design

In designing a supersonic nozzle, it is desired to expand the flow from M=1 at the throat to $M=M_e$ at the exit, where the flow is to be uniform and parallel to the direction at the throat. Such a nozzle consists of an arbitrarily shaped initial expansion region, followed by a wave cancellation region whose shape is uniqely determined by $M_e$, $\gamma$, and the shape of the initial expansion region. Assuming that the sonic line at the throat is straight, the shape of the cancellation region can be constructed graphically using the method of characteristics. Such construction is tedious and, unless the designer is very skillful, inaccurate.

Foelsch [1944] has shown that by assuming the flow immediately downstream of the initial expansion region to be radial, one obtains an exact analytical expression for the shape of the cancellation region. We consider the nozzle geometry shown on Figure A.1. For simplicity, the initial expansion region $T_1D_1$ is a circular arc of radius R and angle $\theta$, although any convex curve ending with inclination $\theta$ can be used. It is followed by a straight line segment $D_1A_1$ and by the cancellation region $A_1E$. The nozzle has an exit height h. The flow at the throat can be taken to be uniform.

We assume that the flow in the part of the nozzle formed by the arcs $D_1D_2$ and $A_1A_2$ of the two concentric circles and the straight lines $D_1A_1$ and $D_2A_2$ has the character of two-dimensional source flow originating at point O upstream of the throat. Actually, the radial flow prevails even further into the region $A_1QA_2$, where $A_1Q$ is the last reflected Mach line. Downstream of the source flow region, the flow is transformed by the action of Mach lines until it is uniform at the

exit. To reconcile the presence of uniform flow at the throat and radial flow in the region downstream of the throat, the portion $T_1T_2D_2D_1$ of the flow is replaced by an imaginary source flow $C_1C_2D_2D_1$ so that the condition and quantity of the flow along the straight line $T_1T_2$ are the same as along the arc $C_1C_2$. Thus, the sonic line $T_1T_2$ is replaced by an equivalent sonic arc $C_1C_2$ which has a radius $r_0$.

In two-dimensional source flow the Mach number at point P is a function of the radius vector r and is determined by the equation

$$r = r_0 \tau \tag{A.1}$$

where

$$\tau = \frac{1}{M}\left[\frac{\gamma+1}{\gamma-1} M^2 + \frac{2}{\gamma+1}\right]^{\frac{\gamma+1}{2(\gamma-1)}} \tag{A.2}$$

The Prandtl-Meyer expansion angle, $\psi$, at point P is given by

$$\psi = \left[\frac{\gamma+1}{\gamma-1}\right]^{1/2} \tan^{-1}\left[\frac{\gamma-1}{\gamma+1}(M^2 - 1)\right]^{1/2} - \tan^{-1}\left[M^2 - 1\right]^{1/2} \tag{A.3}$$

From (A.1), (A.2), and (A.3) we determine the equation of a Mach line

$$r = f(\psi) \tag{A.4}$$

in a two-dimensional source flow.

In order to construct a nozzle for exit Mach number $M_e$ and a given $\gamma$, the designer chooses the Mach number at point $A_1$, $M_a$, which also defines the expansion angle, $\psi_a$, at that point. The angle of the initial expansion is thus $\theta=\psi_e-\psi_a$, where $\psi_e$ is the final expansion angle corresponding to $M_e$. After considerable algebra, the coordinates of the cancellation region are found to be

$$\frac{x + x_0}{h} = \frac{\cos(\psi_e-\psi)}{\psi_e-\psi_a} \frac{\tau}{\tau_e} \left[1 + (\psi-\psi_a) \left[(M^2-1)^{1/2} - \tan(\psi_e-\psi)\right]\right] \quad (A.5)$$

$$\frac{y}{h} = \frac{\sin(\psi_e-\psi)}{\psi_e-\psi_a} \frac{\tau}{\tau_e} \left[1 + (\psi-\psi_a) \left[(M^2-1)^{1/2} - \cot(\psi_e-\psi)\right]\right] \quad (A.6)$$

where

$$x_0 = [h^* + R(1 - \cos\theta)] \cot\theta - R \sin\theta \quad (A.7)$$

and $h^*=h/\tau_e$ is the throat height.

In the current nozzle designs, $\psi_a = 1/2\ \psi_e$ and the ratio $R/h^*$ ranges from 5 for the low $M_e$ nozzles to 12 for the high $M_e$ nozzles.

## Appendix B

## Compressible Thwaites Method

In two-dimensional incompressible boundary layer under arbitrary pressure gradient (provided that separation is not imminent), the momentum thickness $\theta(x)$ can be reliably obtained by the Thwaites method.

$$\theta^2 = 0.45 \, \nu \, U^{-6} \int_0^x U^5 \, dx \tag{B.1}$$

It is possible, under certain assumptions concerning heat conduction and gas properties, to transform (B.1) for compressible boundary layer. There are several versions of a compressible Thwaites method, the simplest one having been proposed by Rott and Crabtree [1952], for which the following assumptions are necessary:

(a) The wall is insulated.

(b) The Prandtl number of the gas is unity.

(c) The viscosity $\mu$ varies linearly with temperature T.

Let $T_t$ be the stagnation temperature, $T_\infty(x)$ the temperature outside the layer, $T(x,y)$ the temperature inside the layer, and $M(x)$ the freestream Mach number. $T_t$ and $T_\infty$ are related by

$$\frac{T_t}{T_\infty} = 1 + \frac{\gamma - 1}{2} M^2 \tag{B.2}$$

while inside the boundary layer, the temperature T under condition (a)

and (b) is given by the law of Busemann [1935] and Crocco [1941]:

$$\frac{T}{T_\infty} = 1 + \frac{\gamma - 1}{2} M^2 \left\{1 - \frac{u^2}{U^2}\right\} \tag{B.3}$$

Since the pressure across the layer is constant, we have

$$\frac{\rho}{\rho_\infty} = \frac{T_\infty}{T} \tag{B.4}$$

Illingworth [1949] and Stewartson [1949] have given a transformation (generalizing a transformation of Howarth [1948]) by which new coordinates $x_i$, $y_i$ are introduced, in which the flow problem reduces to the incompressible case:

$$x_i = \int_0^x \left\{\frac{T_\infty}{T_t}\right\}^{\frac{3\gamma - 1}{2(\gamma - 1)}} dx \tag{B.5}$$

$$y_i = \left\{\frac{T_\infty}{T_t}\right\}^{\frac{\gamma + 1}{2(\gamma - 1)}} \int_0^x \frac{T_\infty}{T} dy \tag{B.6}$$

The velocity transformation in x and y must also be transformed by putting

$$u_i(x_i, y_i) = \left\{\frac{T_t}{T_\infty}\right\}^{1/2} u(x,y)$$

The momentum thickness of the compressible layer is given by

$$\theta = \int_0^x \left\{1 - \frac{u}{U}\right\} \frac{\rho\, u}{\rho_\infty\, U_\infty} dy \tag{B.8}$$

while the equation for the transformed incompressible case gives

$$\theta_i = \int_0^{x_i} \left\{1 - \frac{u_i}{U_i}\right\} \frac{u_i}{U_i}\, dy_i \qquad (B.9)$$

From (B.4), (B.5), and (B.7) these two momentum thicknesses are related as follows:

$$\theta_i = \left\{\frac{T_\infty}{T_t}\right\}^{\frac{\gamma - 1}{2\gamma - 1}} \theta \qquad (B.10)$$

The properties of the transformed incompressible fluid have the values found at the stagnation point of the compressible fluid. Thus, the quantity $\theta_i$ is given from (B.1) by

$$\theta_i^2 = 0.45\, \nu_t\, U_i^{-6} \int_0^{x_i} U_i^5\, dx_i \qquad (B.11)$$

Replacing $dx_i$, $U_i$, and $\theta_i$ by (B.5), (B.7) and (B.10) respectivelly, the result for the momentum thickness of the compressible layer is

$$\theta^2 = 0.45\, \nu_t \left\{\frac{T_t}{T_\infty}\right\}^{\frac{\gamma+1}{\gamma-1}-3} U^{-6} \int_0^{x} \left\{\frac{T_t}{T_\infty}\right\}^{3-\frac{2\gamma-1}{\gamma-1}} U^5\, dx \qquad (B.12)$$

This formula gives $\theta(x)$ in the compressible case directly, without the necessity of carrying out the transformation.

## Appendix C

## Sensitivity of Velocity Profile on Density Profile

It was stated in Section 3.4 that, in the current experiments, velocity profiles for the heterogeneous cases cannot be constructed without some assumption about the concentration profiles. It is our intention to show that, in general, the velocity profile produced by such assumption is no better than the assumption itself.

Assuming an ad-hoc relation between the velocity and density profiles, one could compute the velocity profile from the pitot-pressure distributions. This, however, is a laborious computational process that must be repeated every time that relation changes. We believe that the point can be made using a simple example that shows how sensitive the computed velocity at some point within the layer is on the assumed value of density at that same point.

We formulate the velocity and density distributions as follows:

$$u(y) = U_2 + (U_1 - U_2) f(y) \qquad (C.1)$$

$$\rho(y) = \rho_2 + (\rho_1 - \rho_2) g(y) \qquad (C.2)$$

where f(y) and g(y) are smooth, monotonic functions whose values vary between 0 for $y=-\infty$ and 1 for $y=+\infty$.

The velocity is given by

$$u(y) = M(y) \left[\frac{\gamma(y)\, p}{\rho(y)}\right]^{1/2} \qquad (C.3)$$

As always, we assume that p is uniform across the layer. Introducing the velocity ratio, $r=U_2/U_1$, and density ratio, $s=\rho_2/\rho_1$, from (C.3) we obtain the following relation between f(y) and g(y):

$$f(y) = \frac{1}{1-r}\,\frac{M(y)}{M_1}\left\{\frac{\gamma(y)}{\gamma_1}\,\frac{1}{s + (1-s)\,g(y)}\right\}^{1/2} - \frac{r}{1-r} \qquad (C.4)$$

In our example, we consider case HN6 (He at $M_1$=1.7, $N_2$ at $M_2$=3.0) with s=9.2 and r=0.52. Suppose that we somehow know that at some point near the middle of the layer M=2.5, $\gamma$=1.5, and g=0.5. From (C.4) we get f=0.1986. At the same point, we now consider a value of g that is 1% in error, i.e., g=0.505, while M and $\gamma$ stay practically the same ($\gamma$(y) and consequently M(y), obtained by the Rayleigh pitot formula (3.8), are weak functions of g(y)). The new value of f is 0.2038, or 2.5% in error. The corresponding change of u is from 763.4 m/s to 766.5 m/s, a 0.4% error.

This example helps to illustrate that, especially for large density difference, an error in the assumed value of g(y) will result in an error of equal order of magnitude in the resulting value of f(y). Therefore, in the absence of concentration measurements, any assumption about the density distribution must have solid theoretical and/or empirical basis, otherwise the construction of velocity profiles becomes a frivolous exercise.

## References

BAILEY, H.A. & KUETHE, A.M. 1957 Supersonic Mixing of Jets and Turbulent Boundary Layers. WADC Tech. Rep. 57-402.

BIRCH, S.L. & EGGERS, J.M. 1973 A Critical Review of the Experimental Data for Developed Free Turbulent Shear Layers. NASA SP-321, 943-949.

BLANDFORD, R.D., BEGELMAN, M.C., & REES, M.J. 1982 Cosmic Jets. Scientific American 5, 82.

BLUMEN, W., DRAZIN, D.G., & BILLINGS, D.F. 1975 Shear Layer Instability of an Inviscid Compressible Fluid. Part 2. J. Fluid Mech., 71(2), 305-316.

BOGDANOFF, D.W. 1982 Compressibility Effects in Turbulent Shear Layers. AIAA J., 21(6),926-927.

BOGDANOFF, D.W. 1984 Interferometric Measurement of Heterogeneous Shear-Layer Spreading Rates. AIAA J., 22(11),1550-1555.

BRADSHAW, P. 1966 The effect of Initial Conditions on the Development of a Free Shear Layer. J. Fluid Mech., 26(2), 225-236.

BREIDENTHAL, R. 1981 Structure in Turbulent Mixing Layers and Wakes Using a Chemical Reaction. J. Fluid Mech., 109, 1-24.

BROWN, G.L. 1974 The Entrainment and Large Structure in Turbulent Mixing Layers. Fifth Australasian Conf. on Hydraulics and Fluid Mechanics, Christchurch, New Zealand, 352-359.

BROWN, G.L. & ROSHKO A. 1974 On Density Effects and Large Structures in Turbulent Mixing Layers. J. Fluid Mech., 64(4). 775-781.

BUSEMANN, A. 1935 Gasstromung mit Laminarer Grenzschicht Entlang einer Platte. Zeitschr. Angew. Math. Mech., 15, 23.

CHAPMAN, D.R., KUEHN, D.M., & LARSON, H.K. 1958 Investigation of Separated Flows in Supersonic and Subsonic Streams with Emphasis on the Effect of Transition. NACA Rep. No. 1356.

CHINZEI, N., MASUYA, G., KOMURO, T., MURAKAMI, A., & KUDOU, K. 1986 Spreading of Two-Stream Supersonic Mixing Layers. Phys. Fluid 29(5), 1345-1347.

CHMIELEWSKI, G.E. 1974 Boundary Layer Considerations in the Design of Aerodynamic Contractions. J. Aircraft, 11, 435-438.

COLES, D. 1981 Pr.LIects for Useful Research on Coherent Structure in the Turbulent Shear Flow. Proc. Indian Acad. Sci., 4(2), 111-127.

COSNER, R.R. 1976 Experiments on Thin Airfoils Spanning a Transonic Shear Flow. Ph.D. Thesis, Calif. Inst. of Tech..

CROCCO, L. 1941 Sullo Strato Limite Laminare nei Gas Lungo una Laminar Piana. Rend. Math. Univ. Roma, 5, 2.

DEMETRIADES, A. 1969 Turbulent Mean-Flow Measurements in a Two-Dimensional Supersonic Wake. The Physics of Fluids, 12(1), 24-32.

DEMETRIADES,A. & BROWER, T.L. 1982 Experimental Study of Transition in a Compressible Free Shear Layer. AFOSR-TR No. 83-0144.

DEVIS, E. 1976 Shock Wave-Induced Mixing in Parallel Flow. Ph.D. Thesis, Cornell Univ., Ithaca, New York.

DIMOTAKIS, P.E. & BROWN, G.L. 1976 The Mixing Layer at High Reynolds Number; Large Structure Dynamics and Entrainment. J. Fluid Mech., 78(3), 535-560.

DIMOTAKIS, P.E. 1986 Two-Dimensional Shear-Layer Entrainment. fIAIAA J., 24(11), 1791-1796.

DUTTON, J.C., MIKKELSEN, C.D., & ADDY, A.L. 1982 A Theoretical and Experimental Investigation of the Constant-Area, Supersonic-Supersonic Ejector. AIAA J., 20(10), 1392-1400.

FERRI, A. & EDELMAN, E. 1967 Some Observations on Heterogeneous Mixing Inside Channels. New York Univ. Report NYU-AA-67-109.

FISCHER, H. 1961 Millimicrosecond Light Source with Increased Brightness. J. Optical Soc. of America, 51(5), 543-547.

FOELSCH, K. 1946 A New Method of Designing Two-Dimensional Laval Nozzles for Parallel and Uniform Jet. North American Rep. NA-46-235-2.

GROPENGIESSER, H. 1970 Study of the Stability of Boundary Layers in Compressible Fluids. NASA TT-F-12, 786.

HATANAKA, H. 1947 On the Stability of a Surface of Discontinuity in a Compressible Fluid. J. Soc. Sci. Culture, Japan, 2, 3-7.

IKAWA, H. & KUBOTA T. 1975 Investigation of Supersonic Turbulent Mixing with Zero Pressure Gradient. AIAA J., 13, 566-572.

JONES, B.G., PLANCHON, H.P., HAMMERSLY, R.J. 1973 Turbulent Space-Time Correlation Measurements in a Plane Two-Stream Mixing Layer at Velocity Ratio 0.3. AIAA 73-225.

KONRAD, J.H. 1976 An Experimental Investigation of Mixing in Two-Dimensional Turbulent Shear Flows with Appplications to Diffusion-Limited Chemical Reactions. Ph.D. Thesis, Calif. Inst. of Tech..

KOOCHESFAHANI, M.M., CATHERASOO, C.J., DIMOTAKIS, P.E., GHARIB, M. & LANG, D.B. 1979 Two-Point LDV Measurements in a PLane Mixing Layer. J. AIAA 17(12), 1347-1351.

LANDAU, L. 1944 Stability of Tangential Discontinuities in Compressible Fluid. Comptes Rendus de l'Academie des Sciences de l'URSS (Doklady), 44(4), 139-141.

LARSON, H.K. & KEATING, S.J. 1960 Transition Reynolds Numbers of Separated Flows at Supersonic Speeds. NASA TN D-349.

LESSEN, M., FOX, J.A., & ZIEN, H.M. 1965 On the Inviscid Stability of the Laminar Mixing of Two Parallel Streams of a Compressible Fluid. J. Fluid Mech., 23(2), 355-367.

LIEPMANN, H. & PUCKETT, A.E. 1947 Introduction to Aerodynamics of a Compressible Fluid. John Wiley & Sons, New York, 239-241.

LIEPMANN, H. & ROSHKO, A. 1957 Elements of Gas Dynamics. John Wiley & Sons, New York, 148.

LIN, C.C. 1953 On the Stability of the Laminar Region Between Two Parallel Streams in a Gas. NACA TN 2887.

LOEHRKE, R.I & NAGIB, H. 1972 Experiments on Management of Free-Stream Turbulence. AGARD Rep. No. 598.

MASLOWE, S.A. & KELLY, R.E. 1971 Inviscid Instability of an Unbounded Heterogeneous Shear Layer. J. Fluid. Mech., 65, 405-415.

MAYDEW, R.C. & REED, J.F. 1963 Turbulent Mixing of Compressible Shear Layers. AIAA J., 1, 1443-1444.

MILES, J.W. 1958 On the Disturbed Motion of a Plane Vortex Sheet. J. Fluid Mech., 4, 538-552.

MUNGAL, M.G., DIMOTAKIS, P.E. & HERMANSON, J.C. 1984 Reynolds-Number Effect on Mixing and Combustion in a Reacting Shear Layer. AIAA-84-0731.

NORMAN, M.L. & WINKLER, K.-H.A. 1983 Propagation and Morphology of Pressure-Confined Supersonic Jets. Max-Planck-Institut fuer Physik und Astrophysik, MPA 61.

OERTEL, H. 1979 Mach Wave Radiation of Hot Supersonic Jets Investigated by Means of the Shock Tube ans New Optical Techniques. Proc. 12th Int. Symp. of Shock Tubes and Waves, Jerusalem, 266-275.

ORTWERTH, P.J. & SHINE, A.J. 1977 On the Scaling of Plane Turbulent Shear Layers. AFWL-TR-77-118.

PAI, S.I. 1954 On the Stability of a Vortex Sheet in an Inviscid Compressible Fluid. J. Aero. Sci., 21, 325-328.

PAPAMOSCHOU, D. & ROSHKO, A. 1986 Observations of Supersonic Free Shear Layers. AIAA-86-0162.

ROBERTS, F.A. 1985 Effects of a Periodic Disturbance on Structure and Mixing in Turbulent Shear Layers and Wakes. Ph.D. Thesis, Calif. Inst. of Tech.

ROSHKO, A. & LAU, J.C. 1965 Some Observations on Transition and Reattachment of a Free Shear Layer in Incompressible Flow. Calif. Inst. of Tech., GALCIT Publ. No. 605.

ROTT, N., & CRABTREE, L.F. 1952 Simplified Laminar Bounary-Layer Calculation for Bodies of Revolution and for Yawed Wings. J. Aero. Sci., 19(8), 553-565.

SHACKLEFORD, W.L., WITTE, A.B., BROADWELL, J.E., TROST, J.E., & JACOBS, T.A. 1973 Experimental Studies of Chemically Reactive ($F+H_2$) Flow in Supersonic Free Jet Mixing Layers. AIAA-73-640.

SIRIEIX, M. & SOLIGNAC, J.L. 1966 Contribution a l'Etude Experimentale de la Couche de Melange Turbulent Isobare d'un Ecoulement Supersonique. Symp. on Separated Flow, AGARD Conf. Proc., 4(1), 241-270.

SPENCER, B.W. & JONES, B.G. 1971 Statistical Investigation of Pressure and Velocity Fields in the Turbulent Two-Stream Mixing Layer. AIAA-71-613.

SREENIVASAN, K.R. & NARASIMHA, R. 1982 Equilibrium Parameters for Two-Dimensional Turbulent Wakes. J. Fluids Engineering, 104, 167.

TAN-ATICHAT, J. NAGIB, H., & DRUBKA, R. 1980 Effects of Axisymmetric on Turbulence of Various Scales. NASA CR-165136.

THWAITES, B. 1949 Approximate Calculation of the Laminer Boundary Layer. Aero. Sci. Quart., 1, 245-280.

WHITE, F.M. 1974 Viscous Fluid Flow, McGraw-Hill, New York, 608.

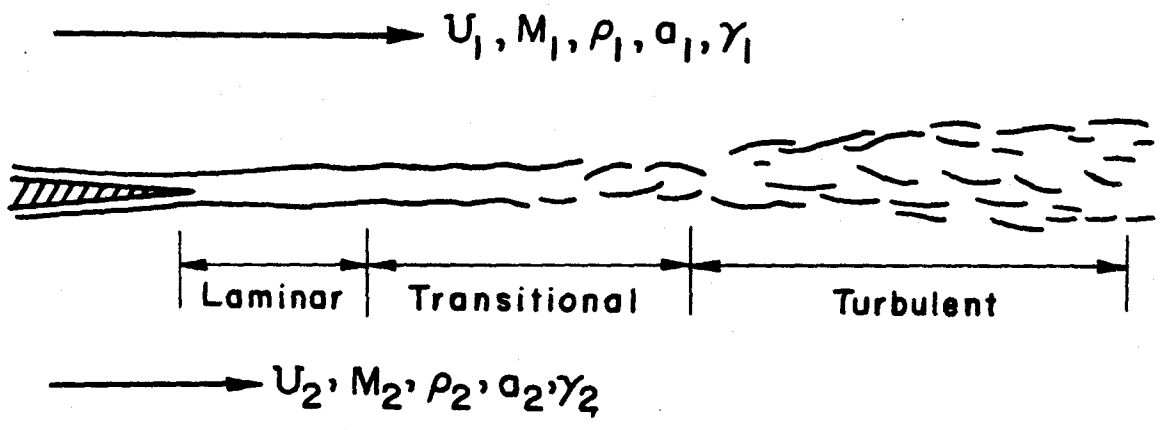


Figure 1.1 Compressible shear layer nonmenclature.

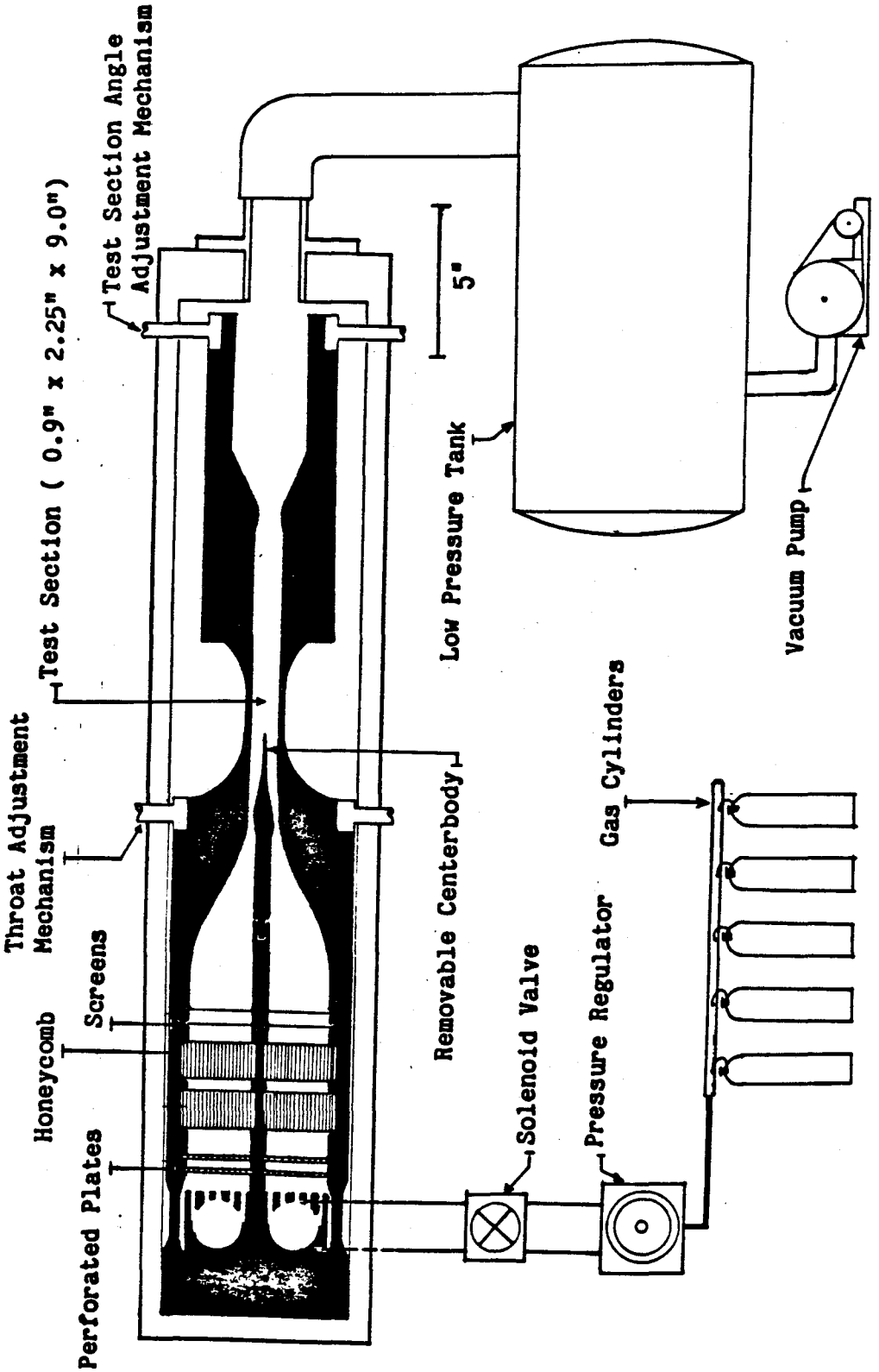


Figure 2.1 Schematic of flow facility.

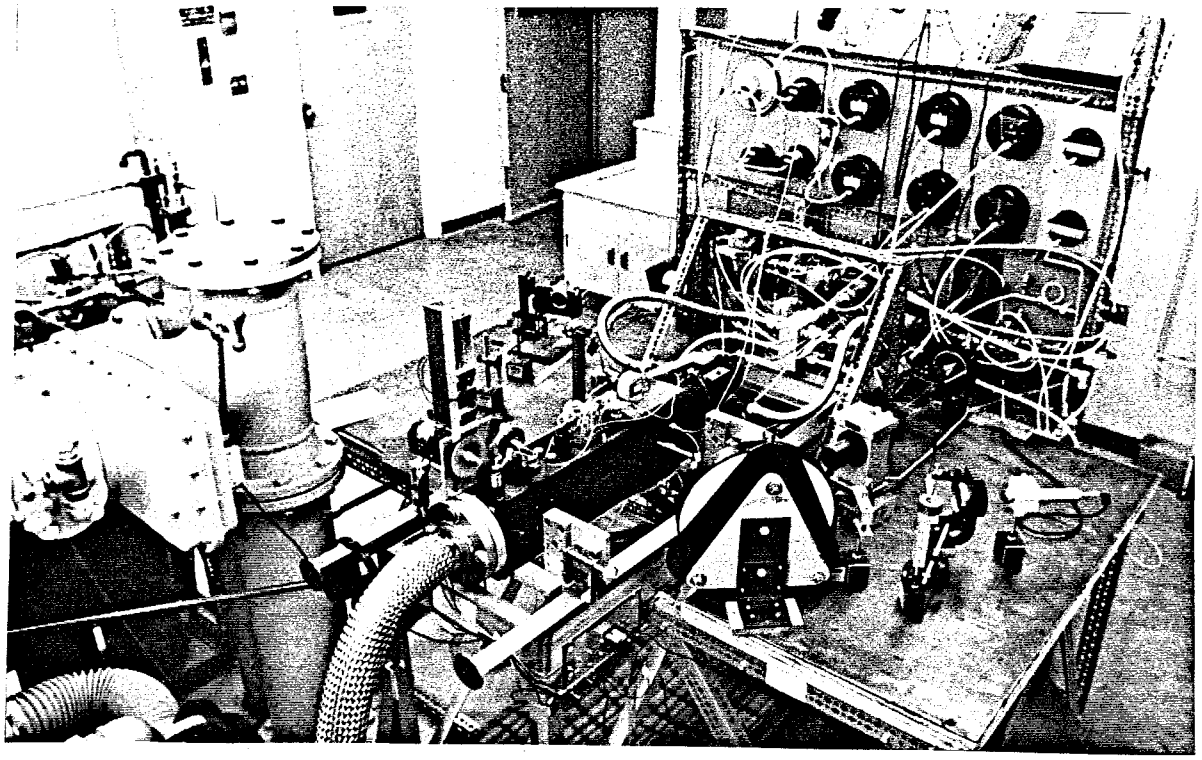

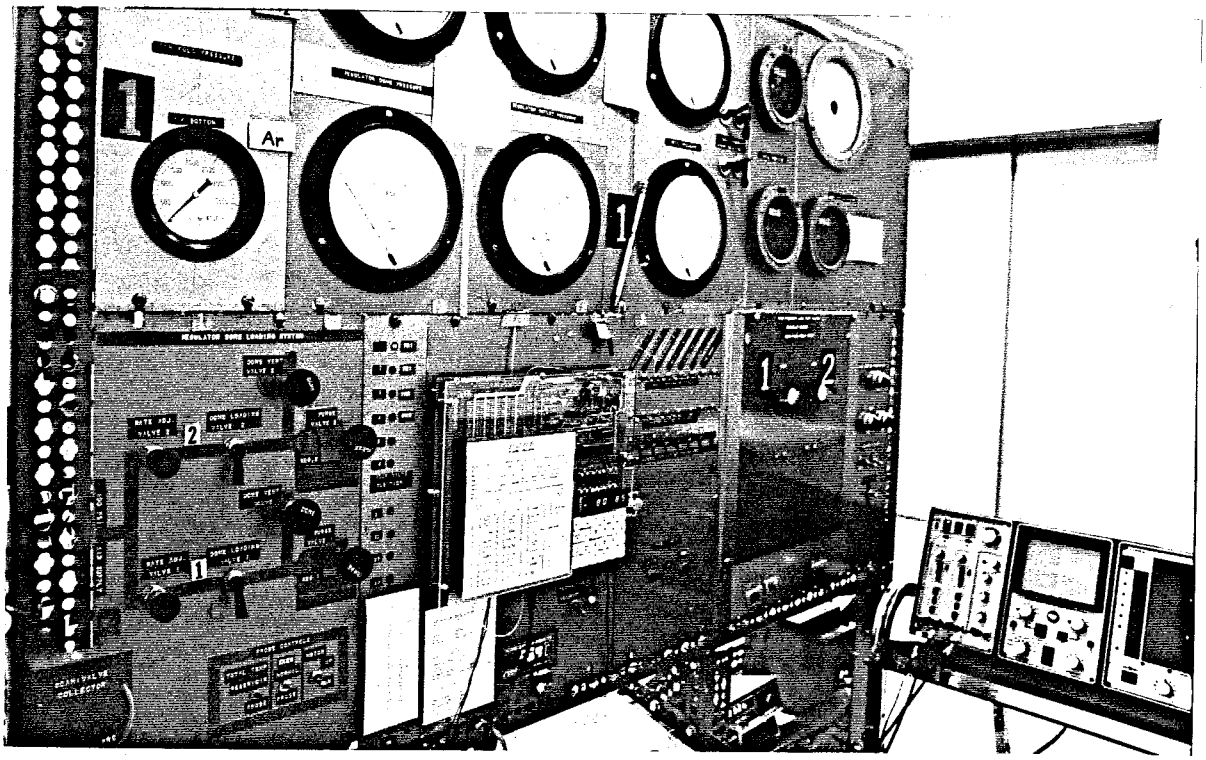


Figure 2.2 Photographs of facility.

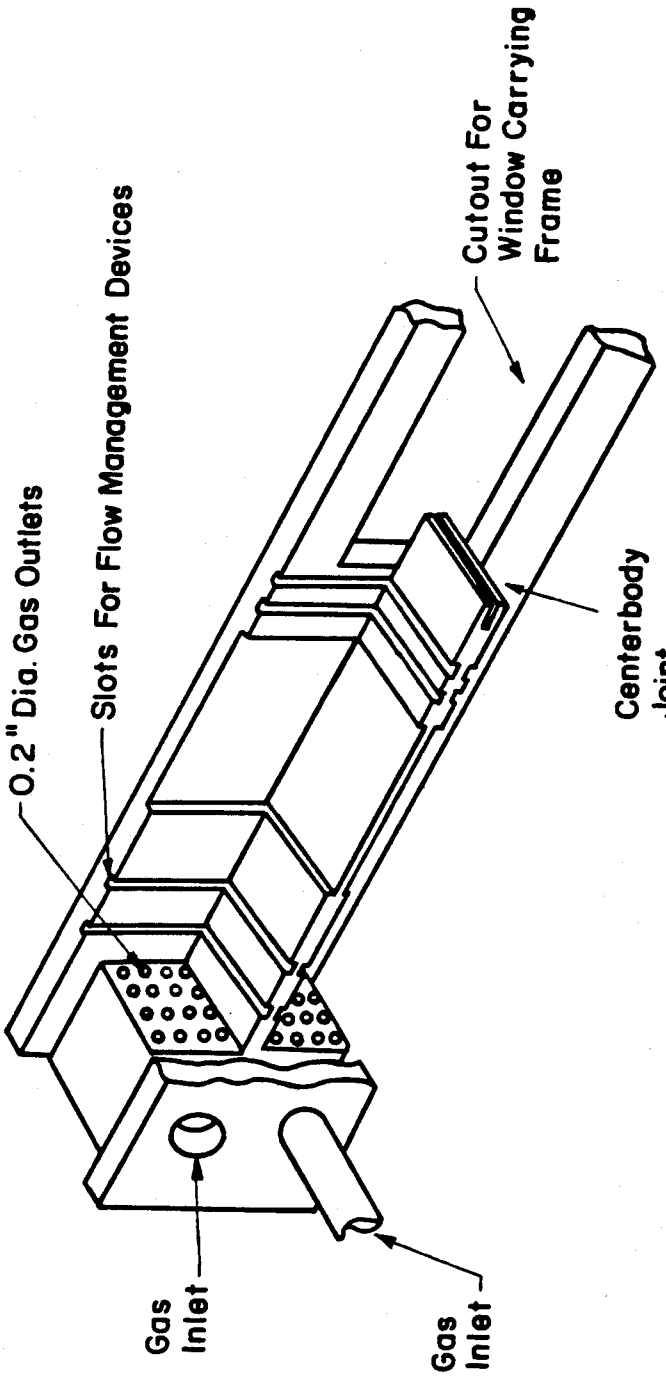


Figure 2.3 Design of settling chamber compartment.

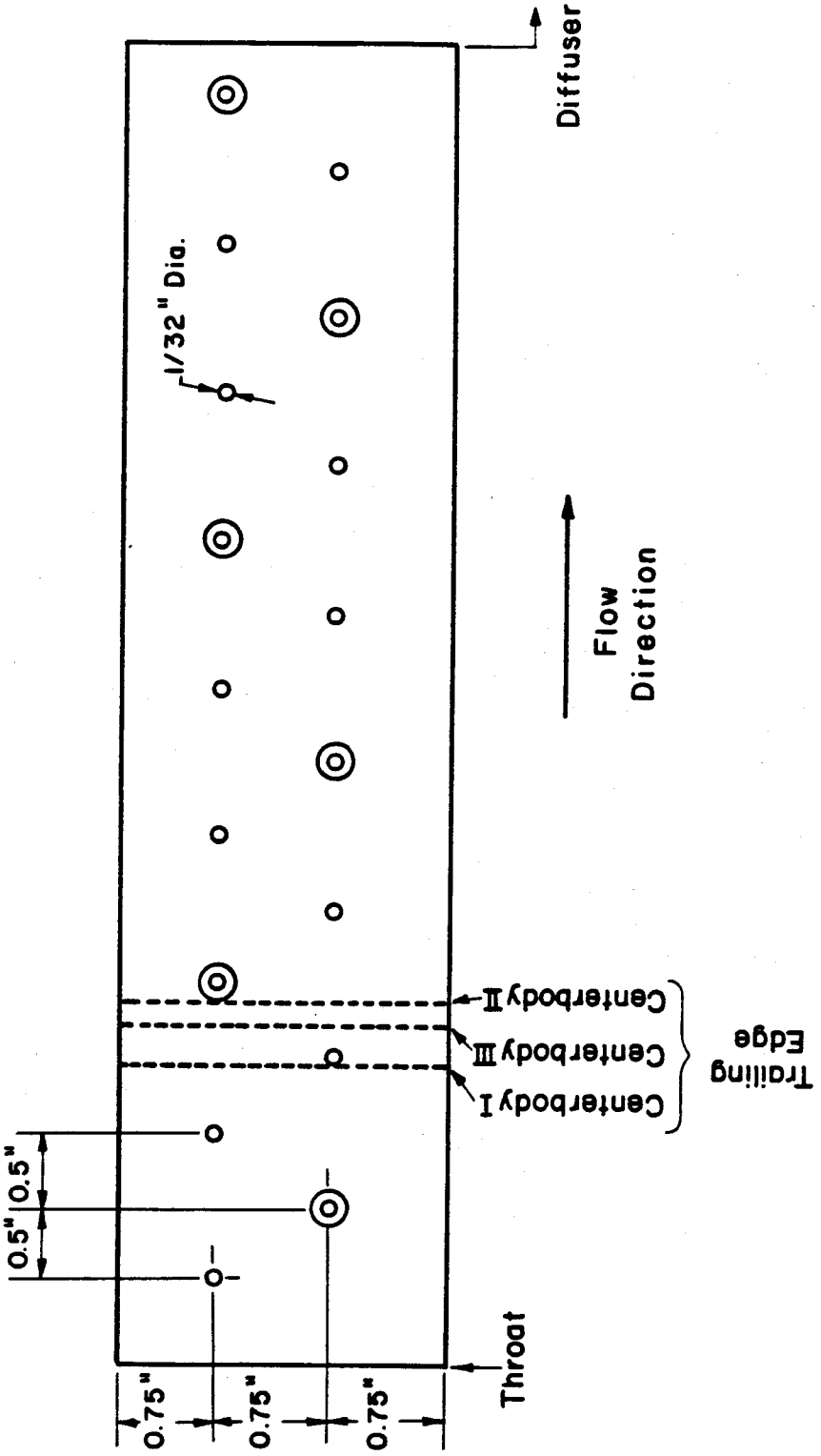


Figure 2.4 Pressure tap arrangement.
Circled are taps actually used.

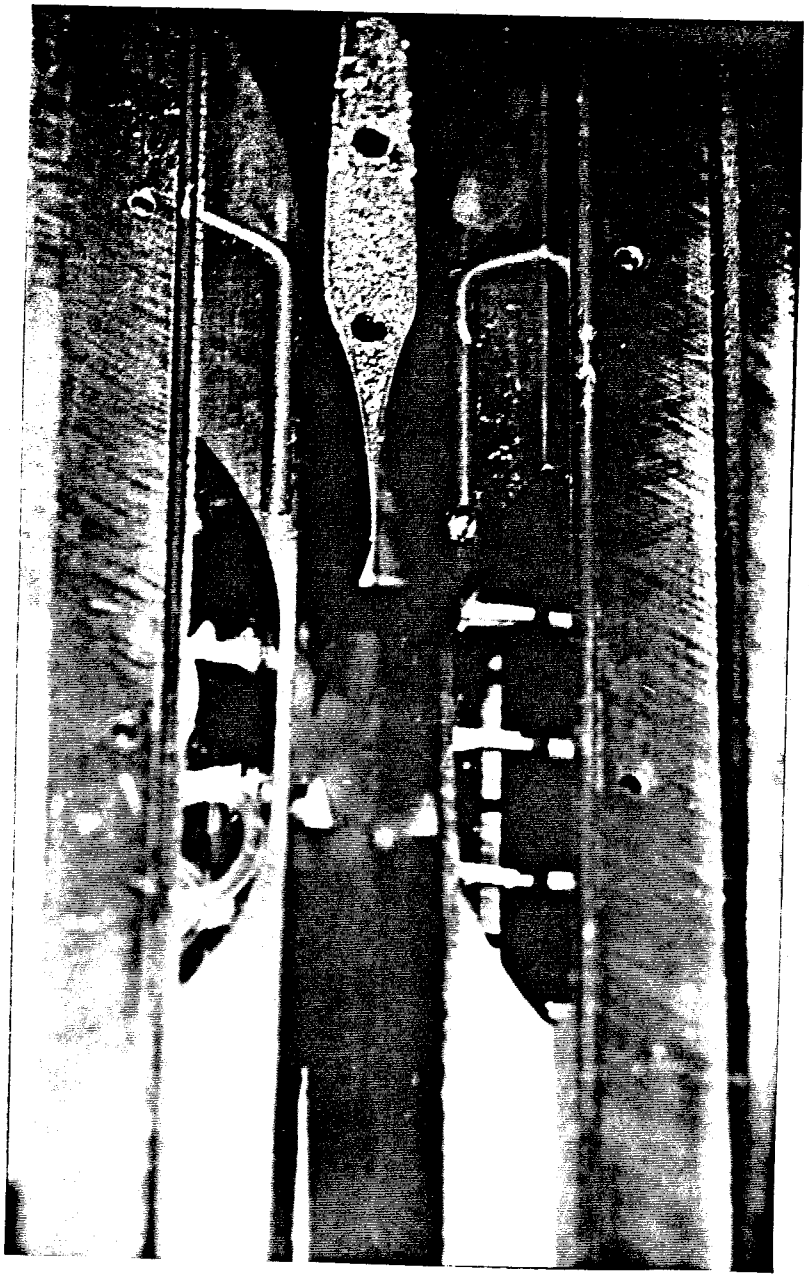

Figure 2.5 Photograph of test section with sidewall removed. Pitot probe is visible at left.

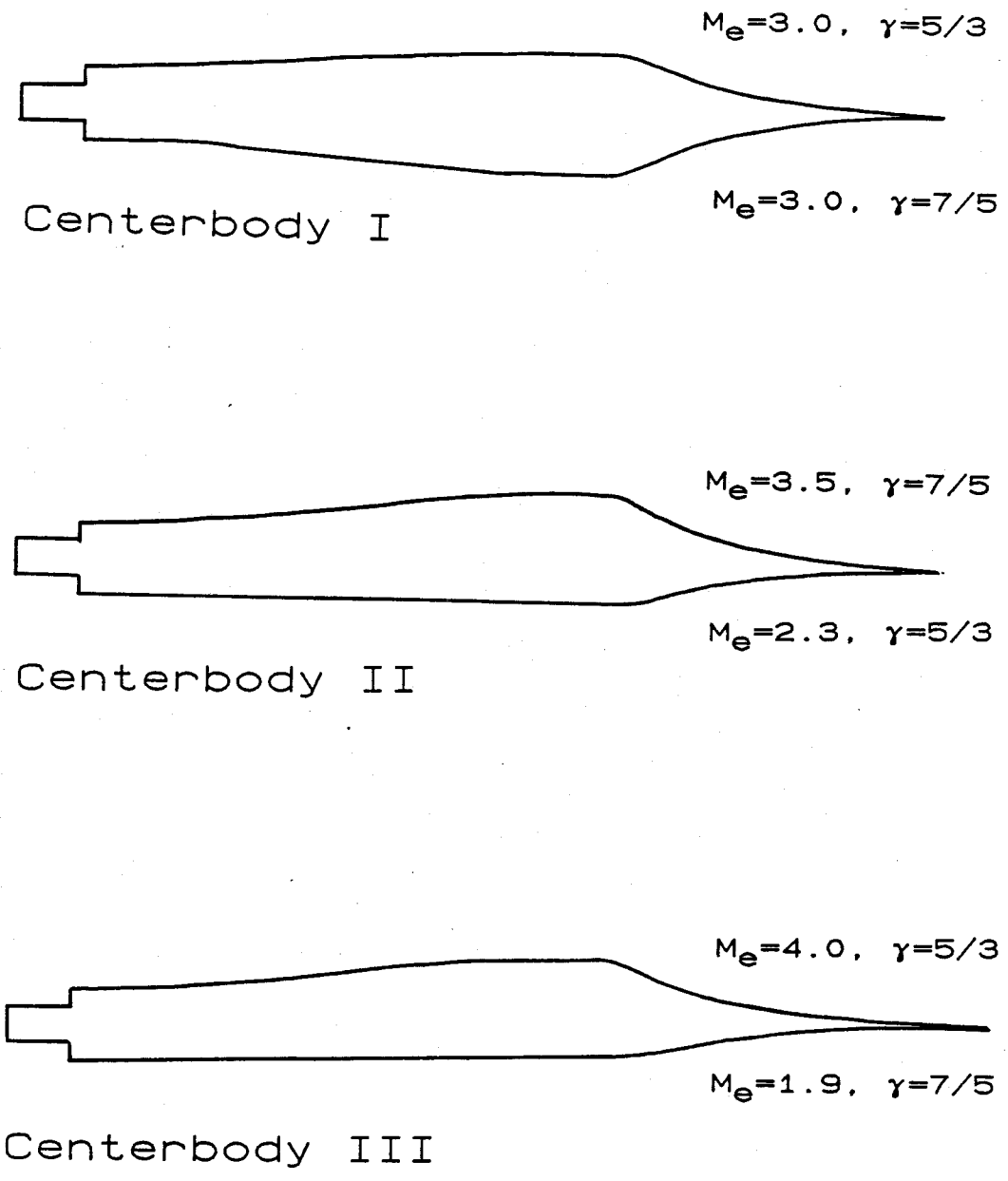


**Figure 2.6 Design of centerbodies.**

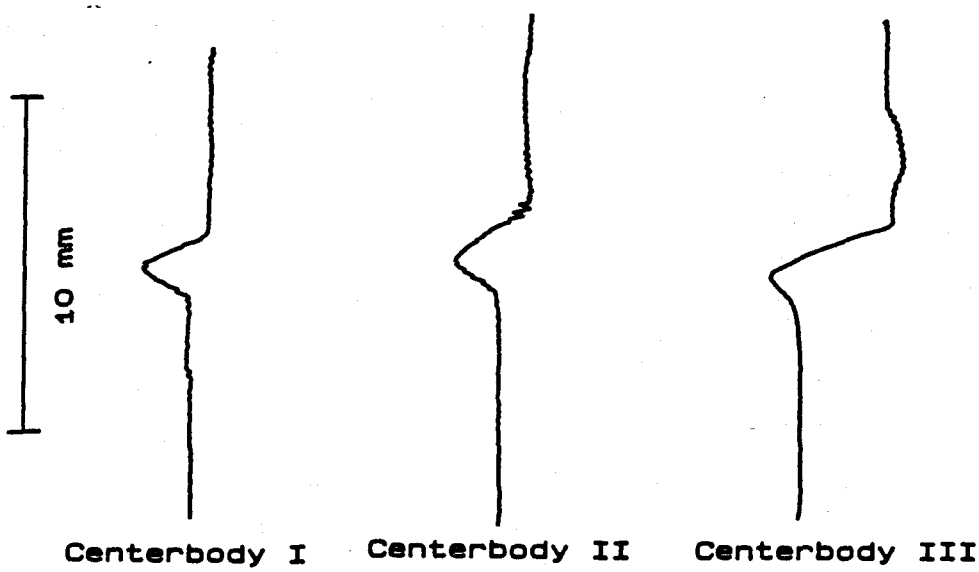


Figure 2.7 Pitot pressure profiles at nozzle exit.

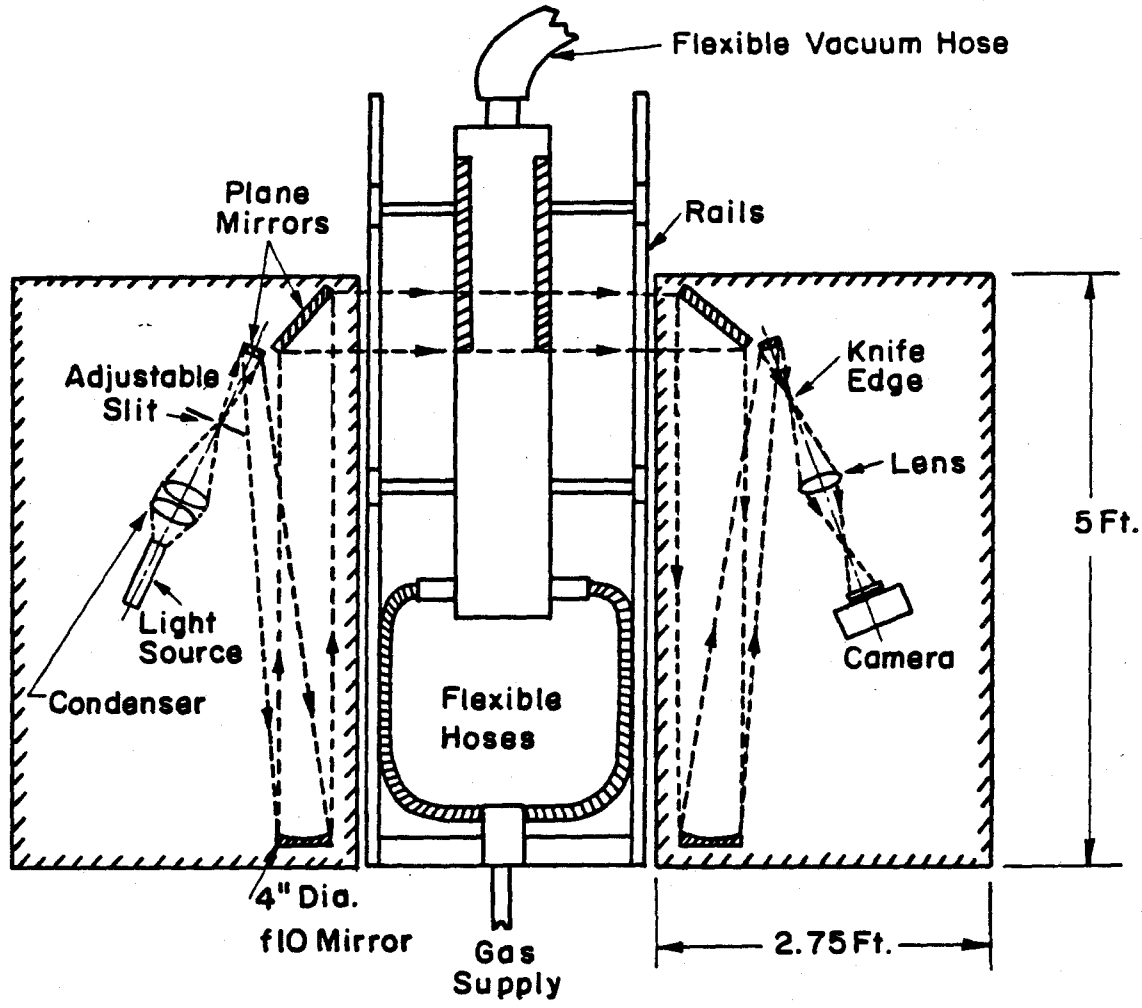


Figure 2.8 Schematic of Schlieren optical system.

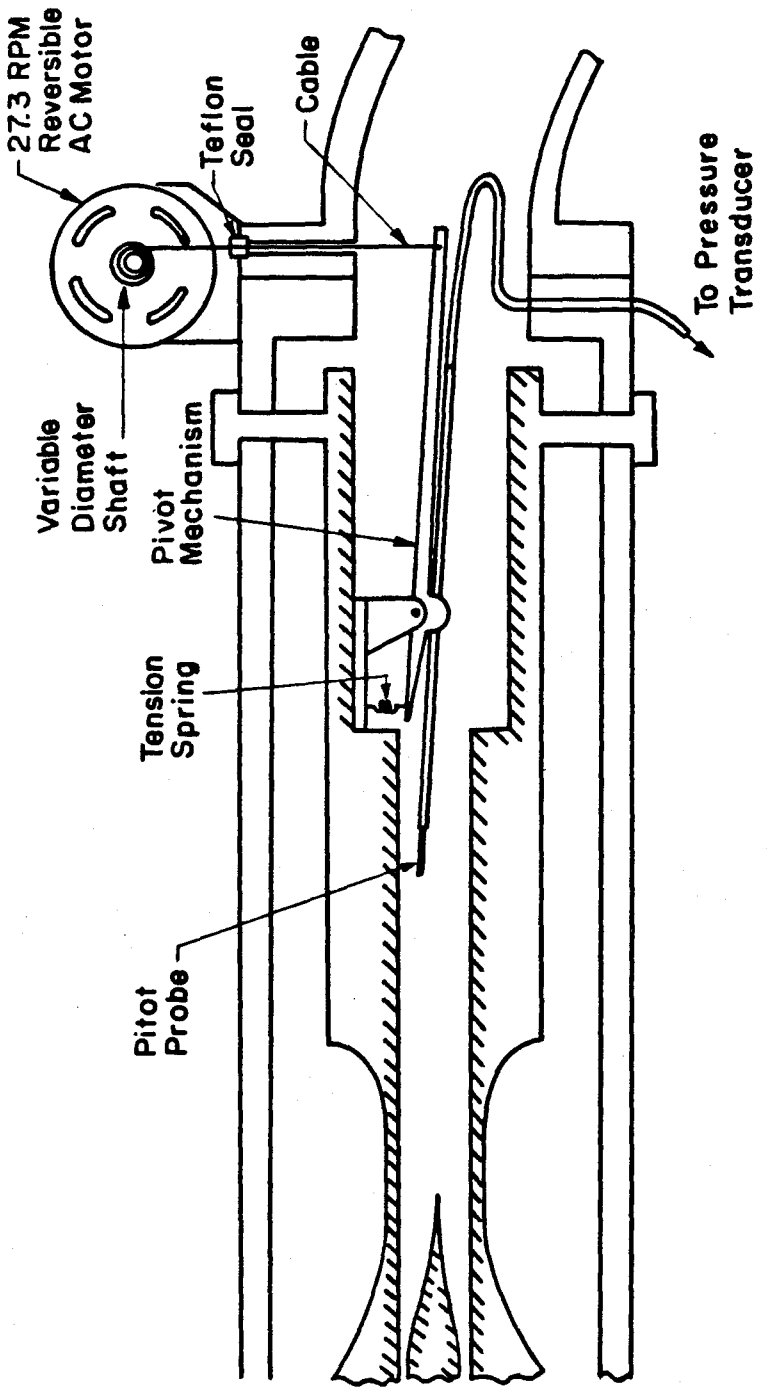


Figure 2.9 Schematic of pitot probe mechanism.

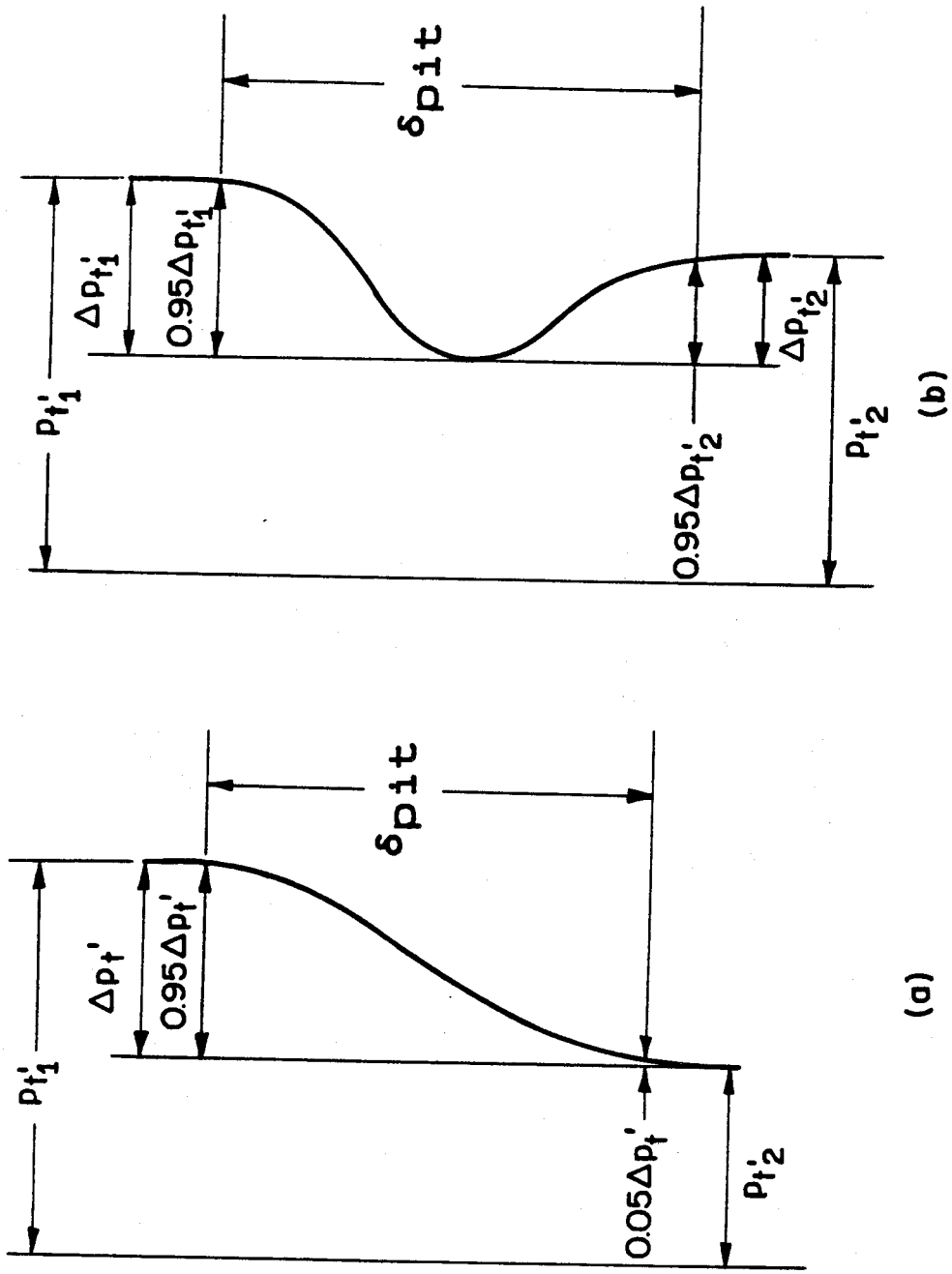


Figure 2.10 Measurement of pitot thickness from pitot pressure profiles,
(a) Monotonic profile,
(b) Profile with defect.

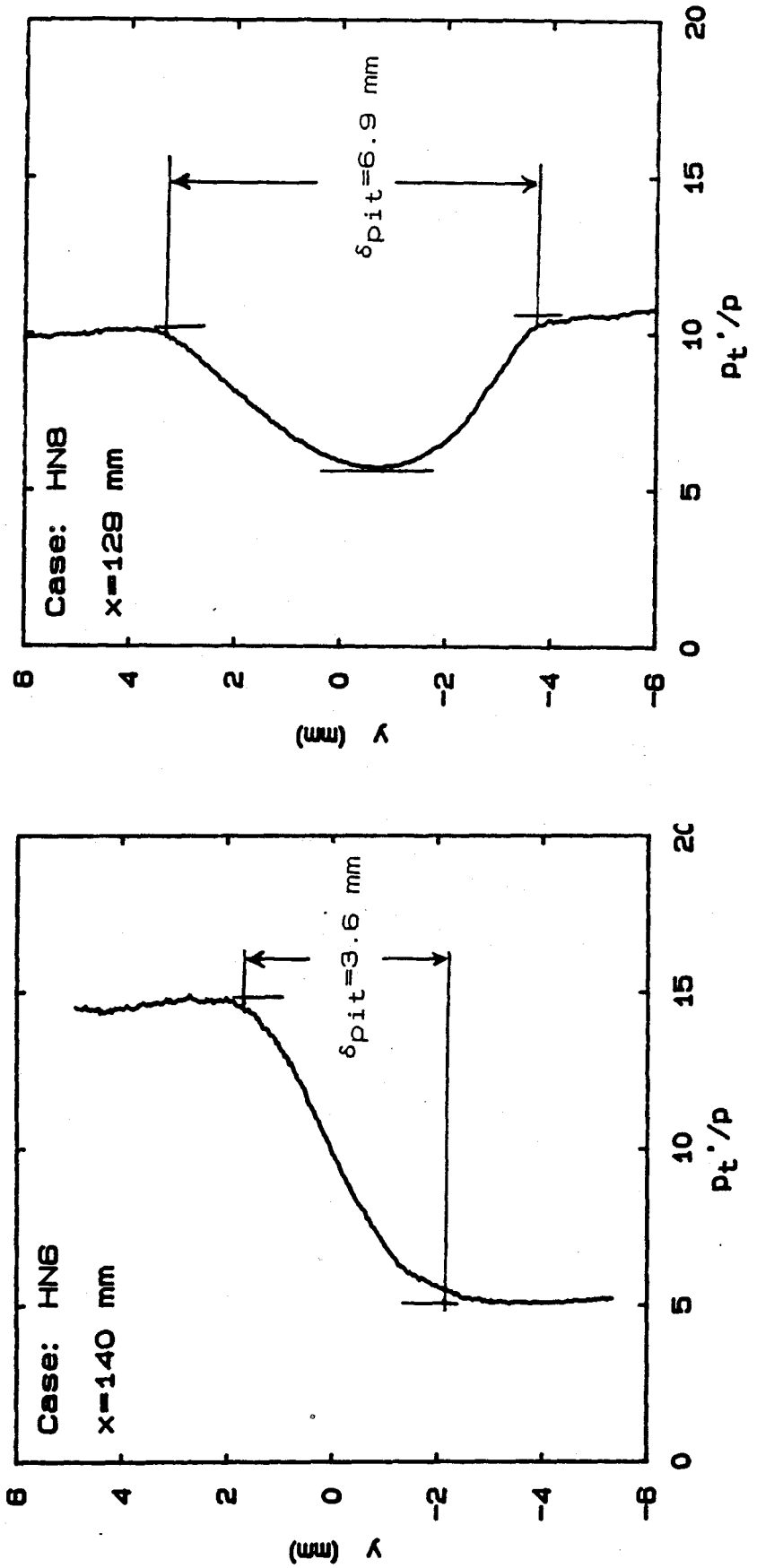


Figure 2.11 Examples of pitot thickness measurement from current pitot pressure profiles.

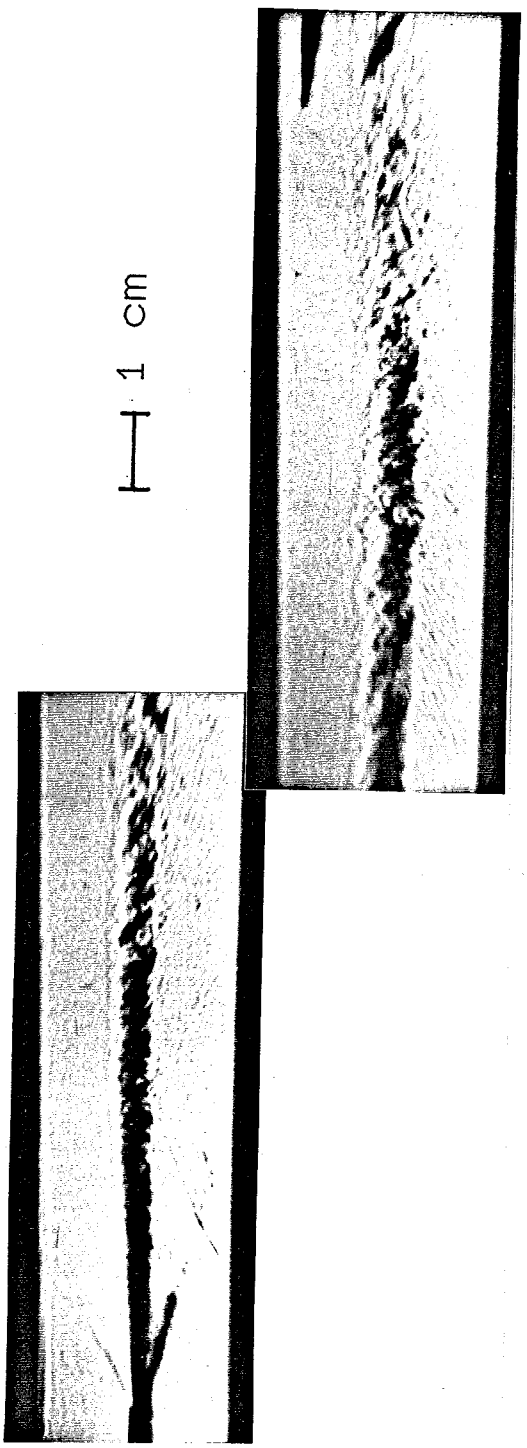


Figure 3.1(a) Schlieren photograph of case NA1.

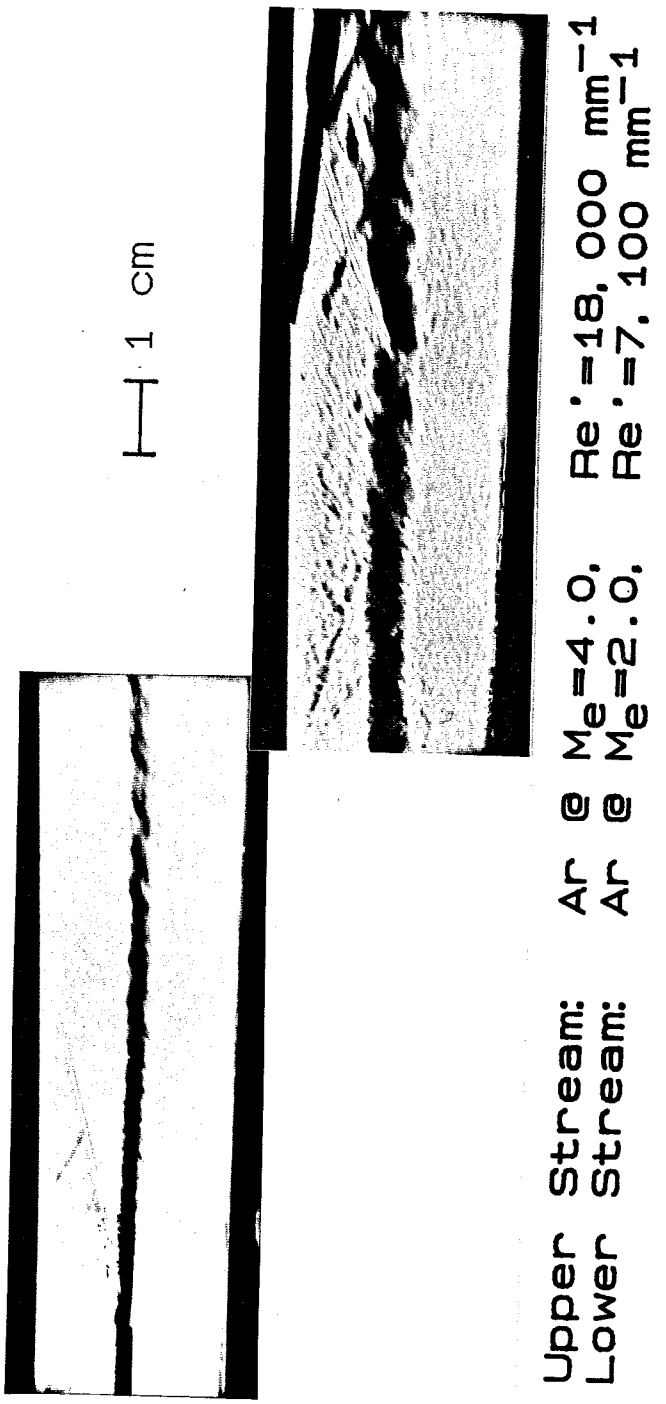


Figure 3.1(b) Schlieren photograph of case AA2.
Pitot probe is visible at right.

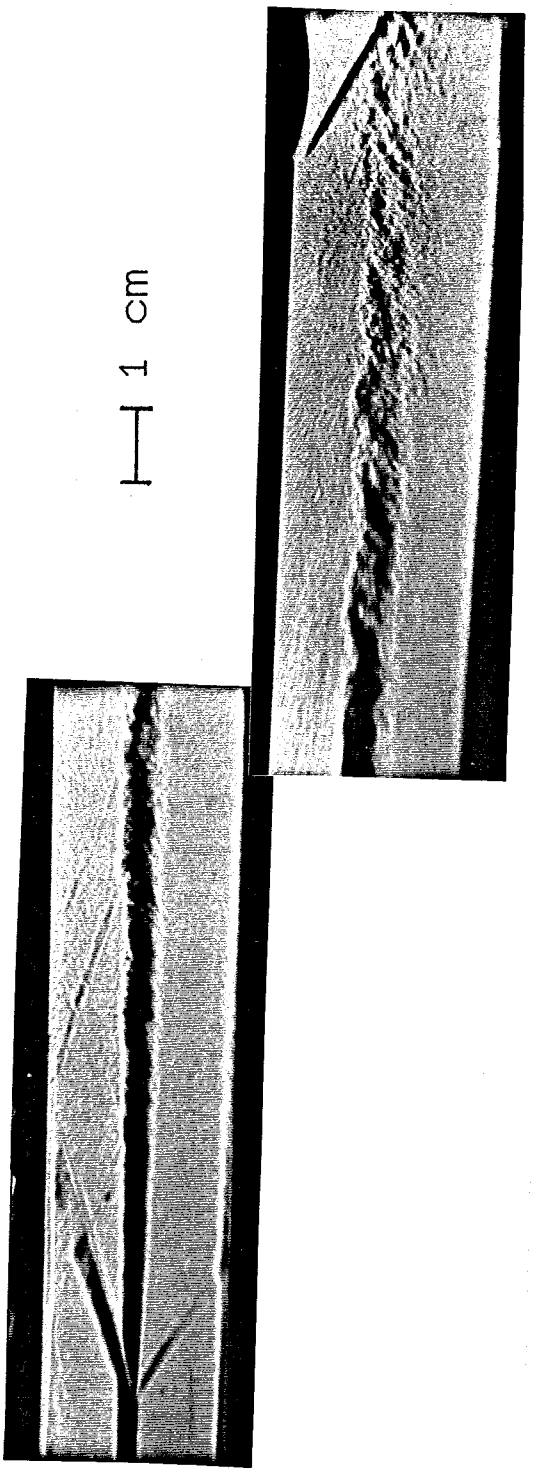


Figure 3.1(c) Schlieren photograph of case NN3.

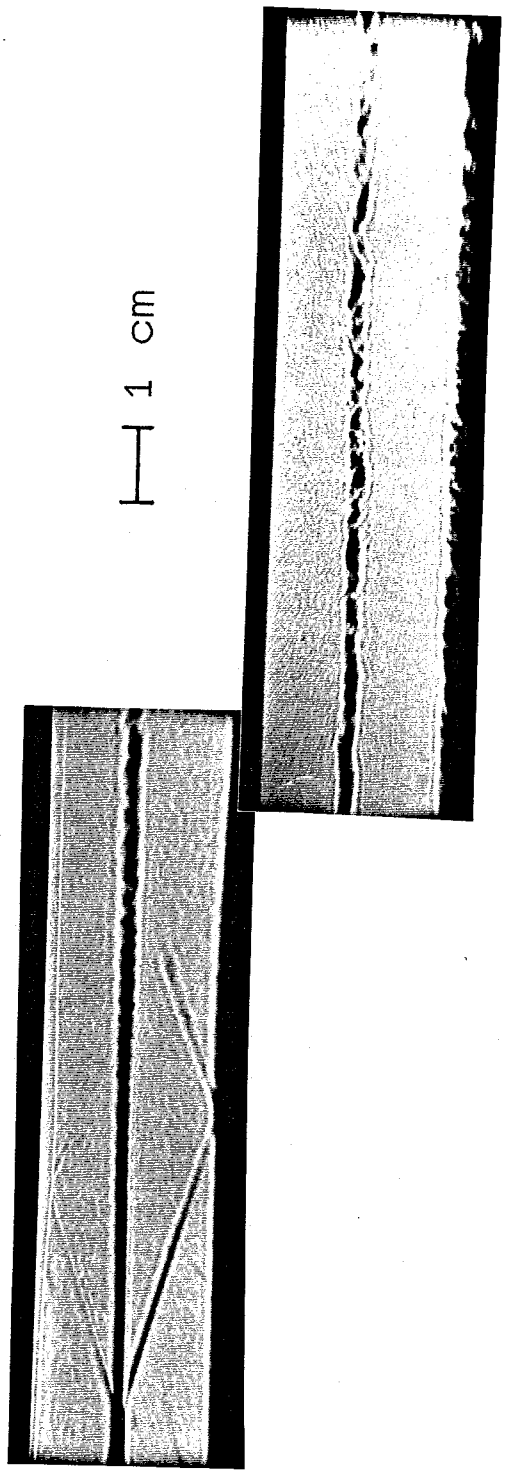


Figure 3.1(d) Schlieren photograph of case NA4.

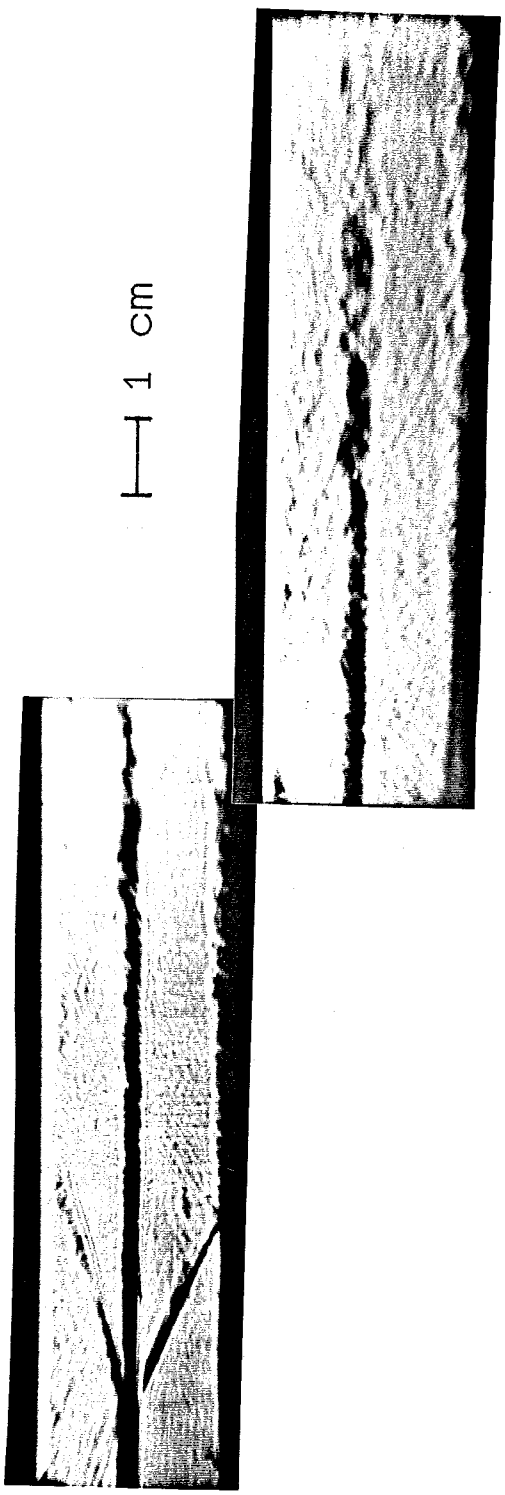


Figure 3.1(e) Schlieren photograph of case NA5.

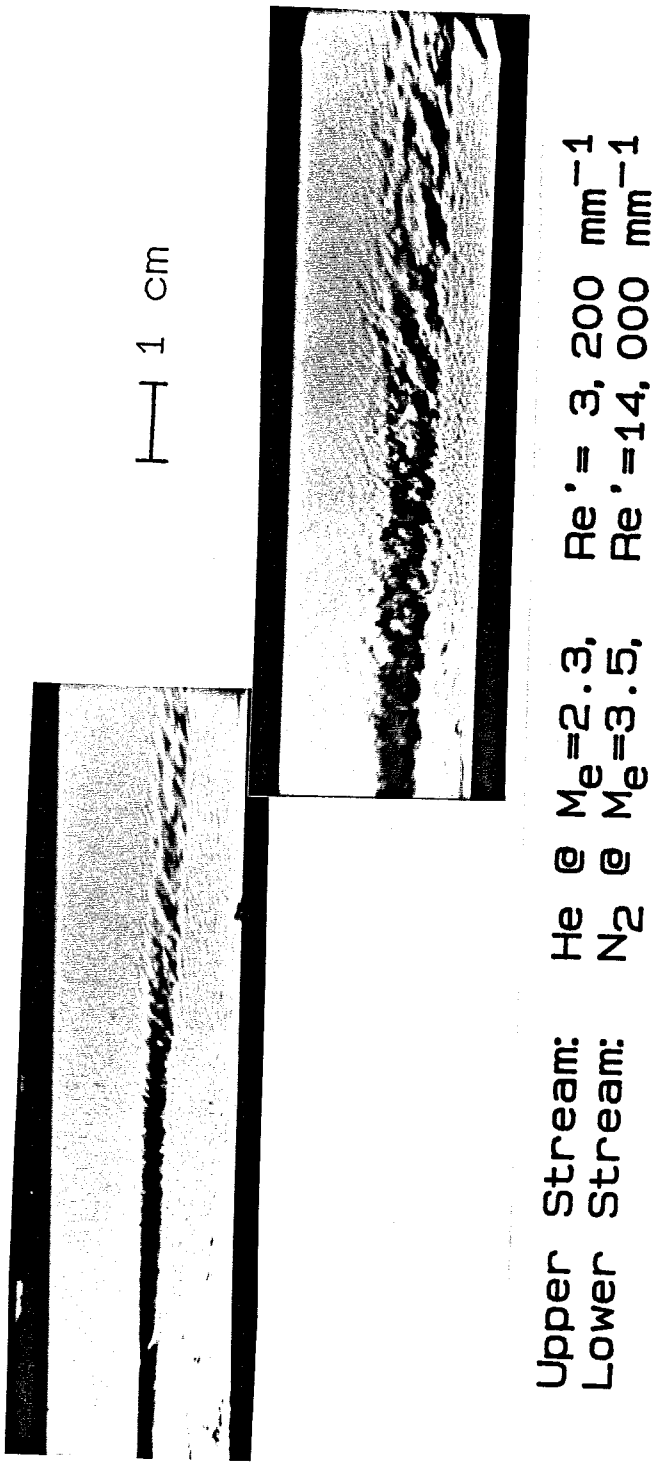


Figure 3.1(f) Schlieren photograph of case HN6.

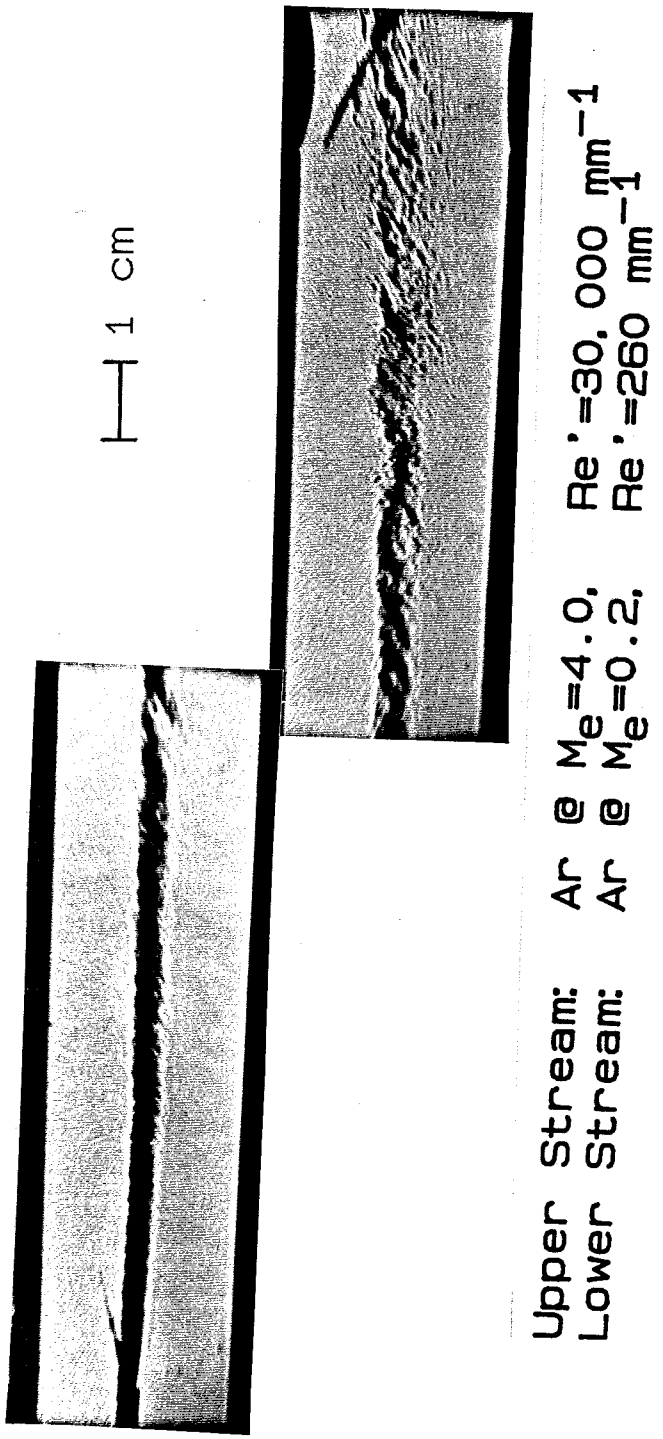


Figure 3.1(g) Schlieren photograph of case AA7.

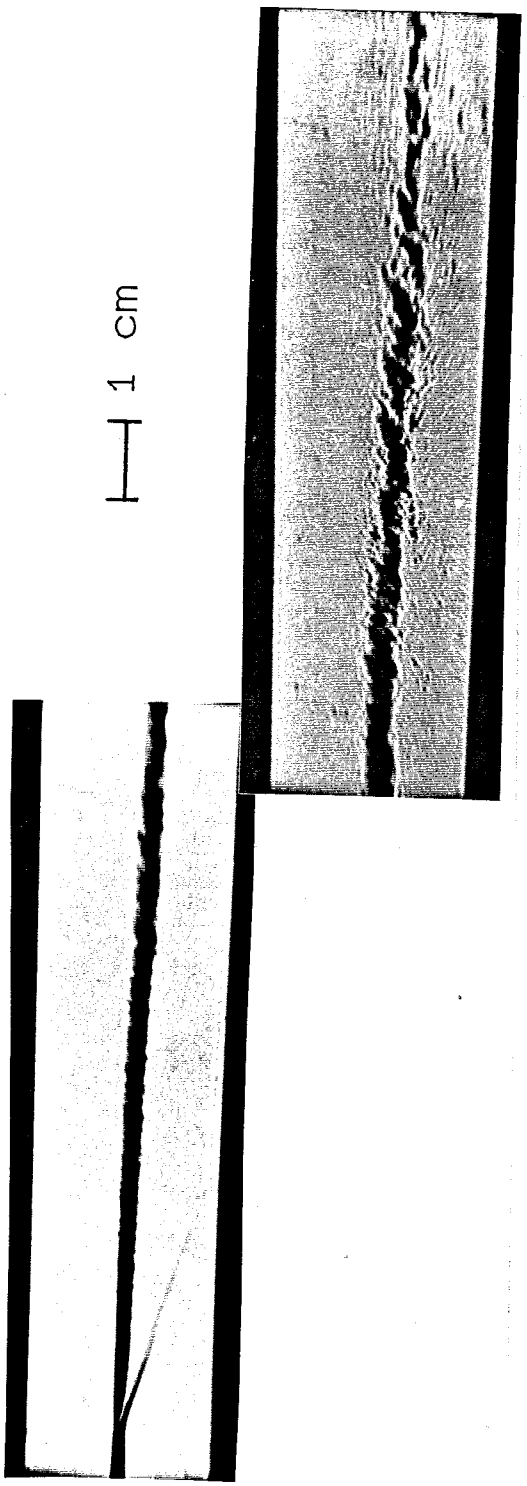


Figure 3.1(h) Schlieren photograph of case HN8.

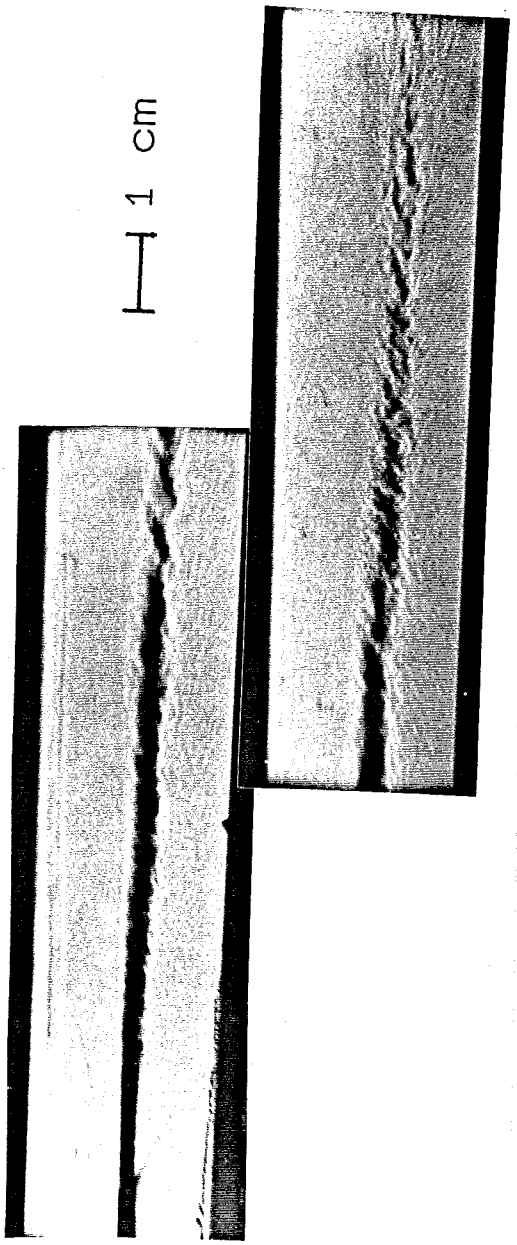


Figure 3.1(i) Schlieren photograph of case HN9.
Overlap is 2 inches.

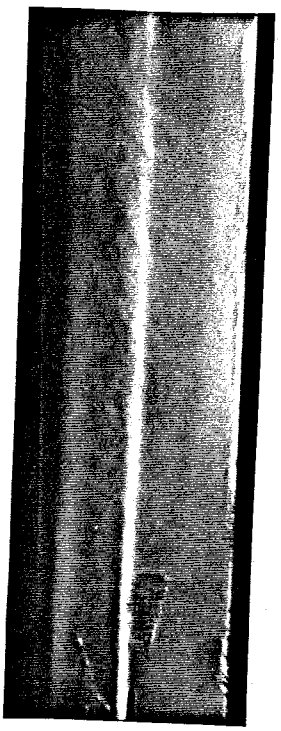

1 cm

Upper Stream: He @ $M_e$=4.0, Re'=8,200 $mm^{-1}$
Lower Stream: Ar @ $M_e$=0.3, Re'=380 $mm^{-1}$

Figure 3.1(j) Schlieren photograph of case HA10.

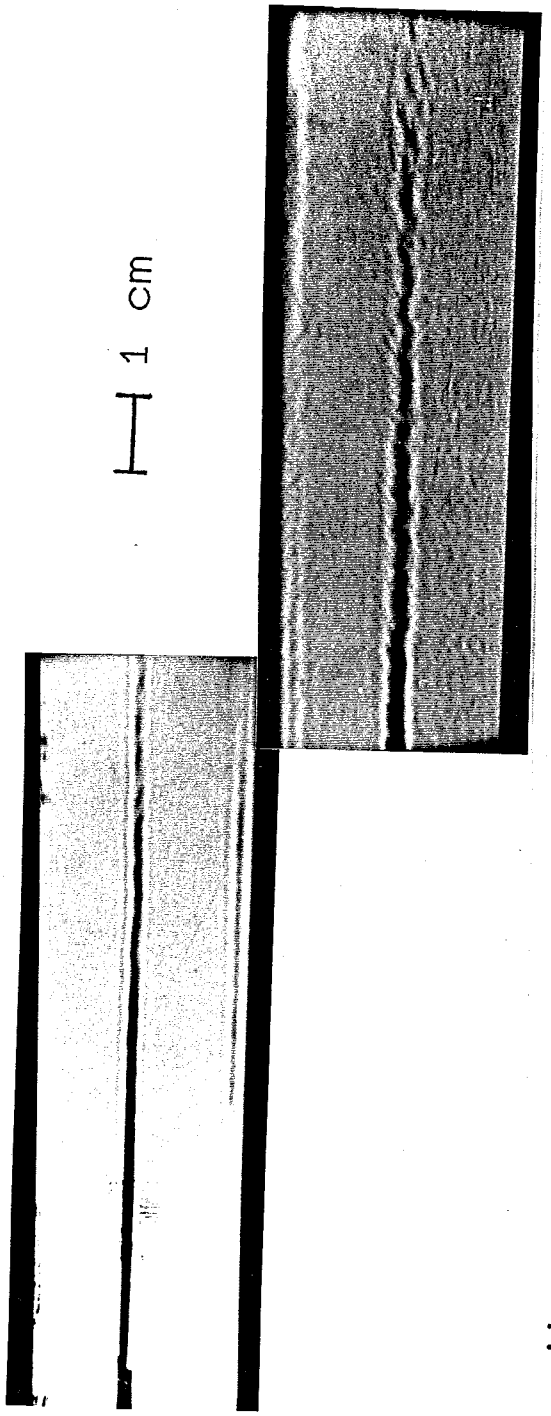


Figure 3.2(a) Schlieren photograph of case NA4 at low pressure.

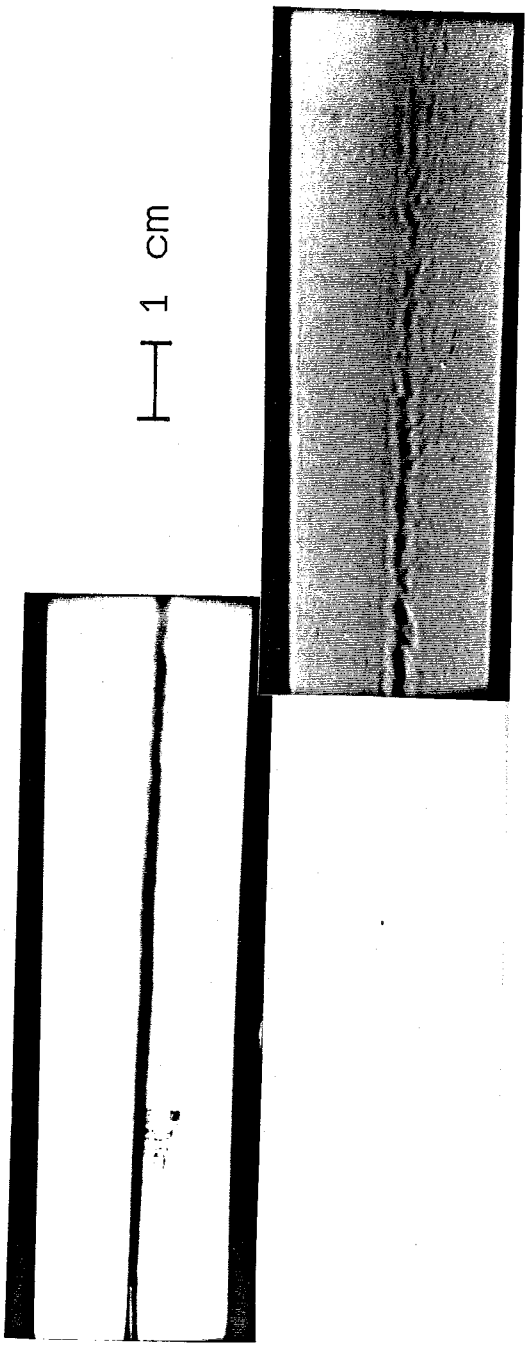


Figure 3.2(b) Schlieren photograph of case HN8 at low pressure.

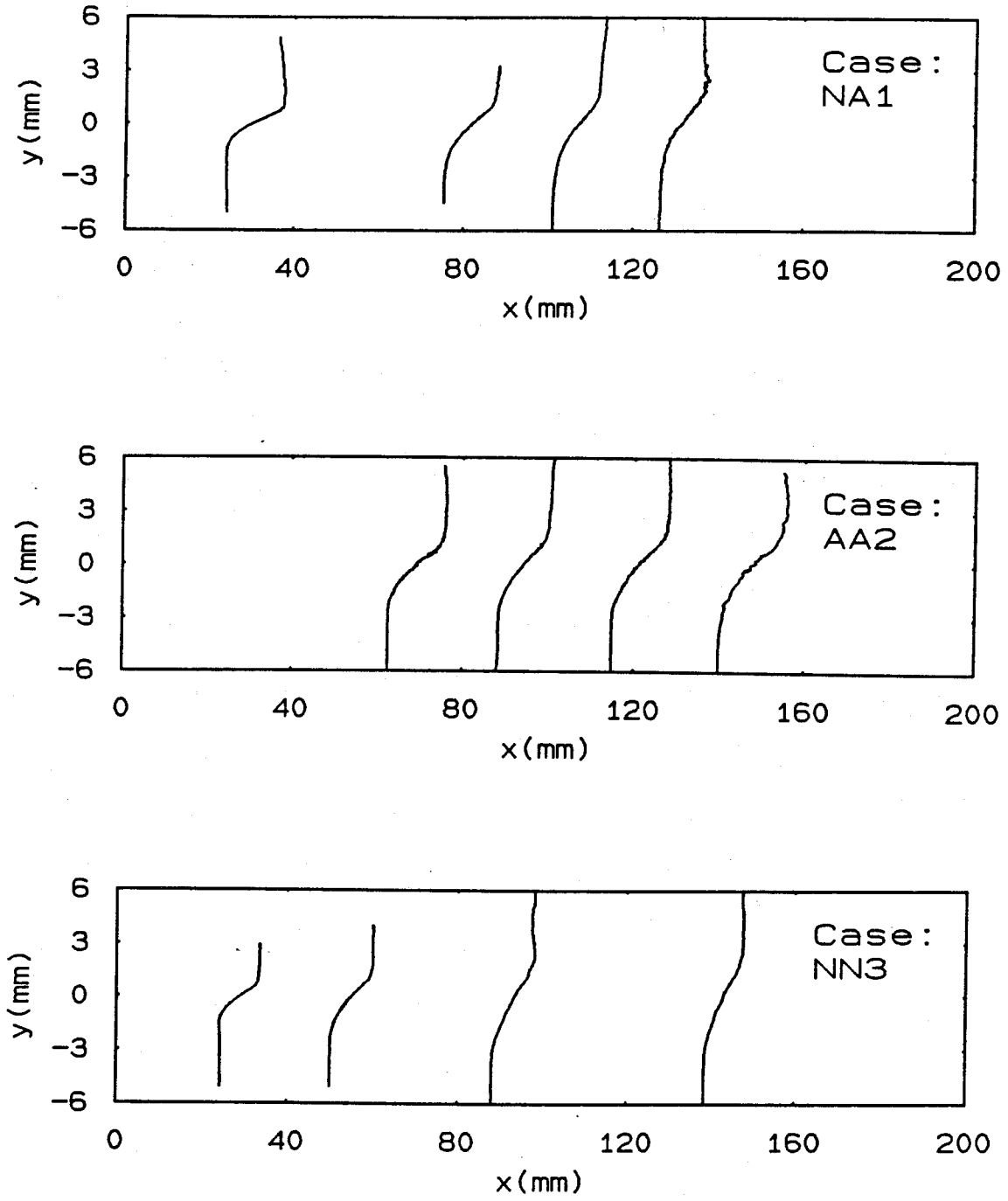


Figure 3.3 Selected pitot pressure profiles.

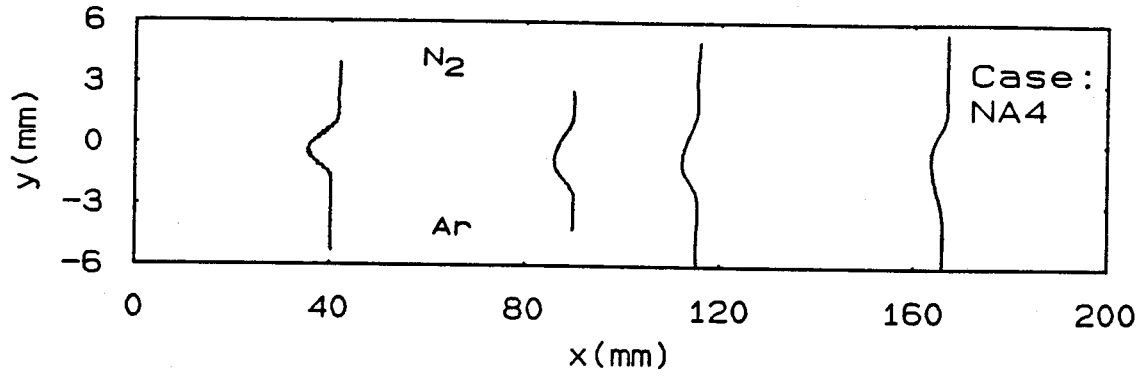


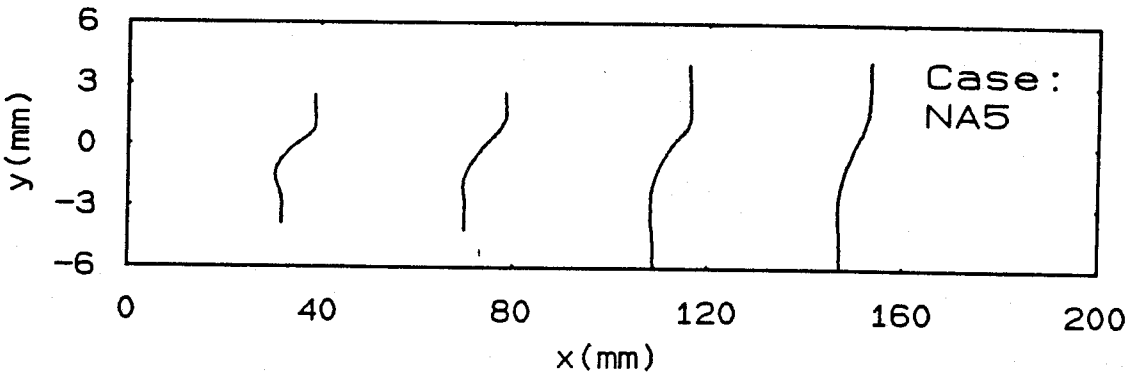


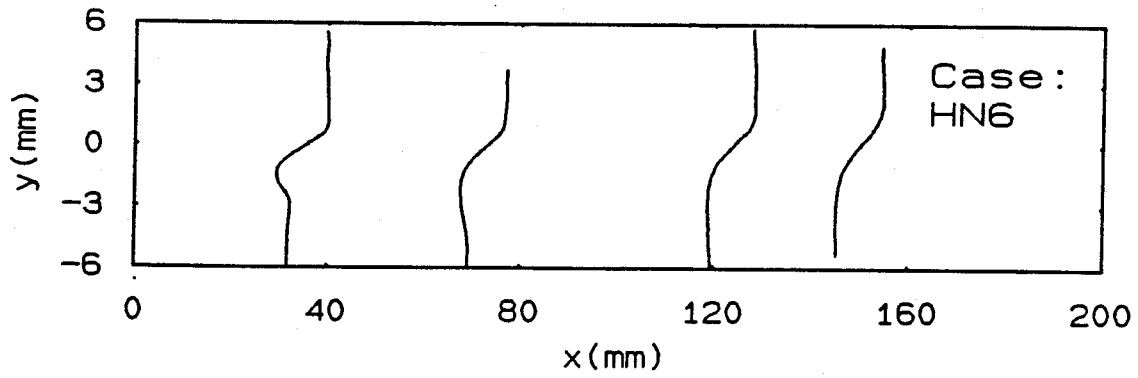


Figure 3.3 Continued.

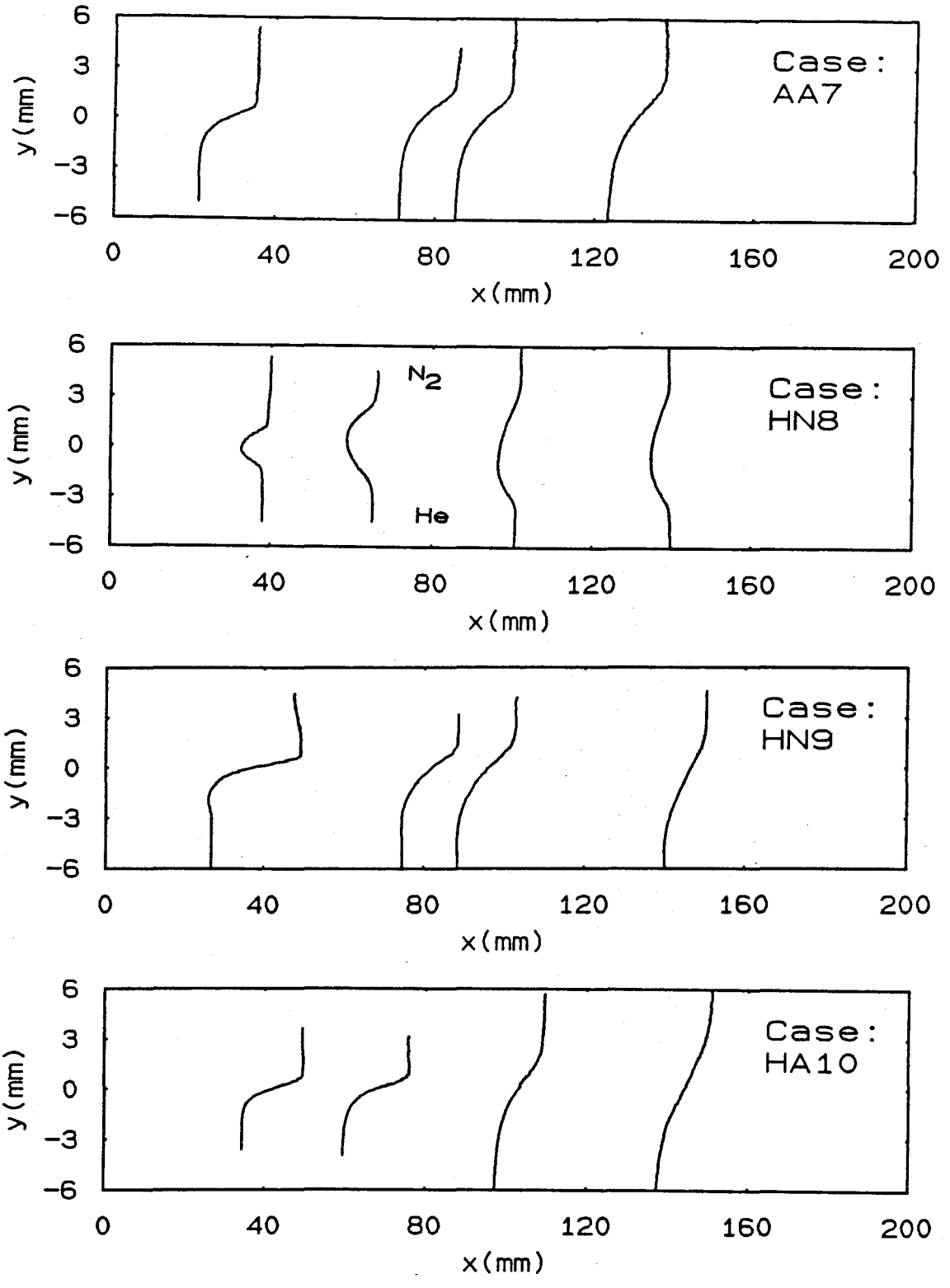


Figure 3.3 Continued.

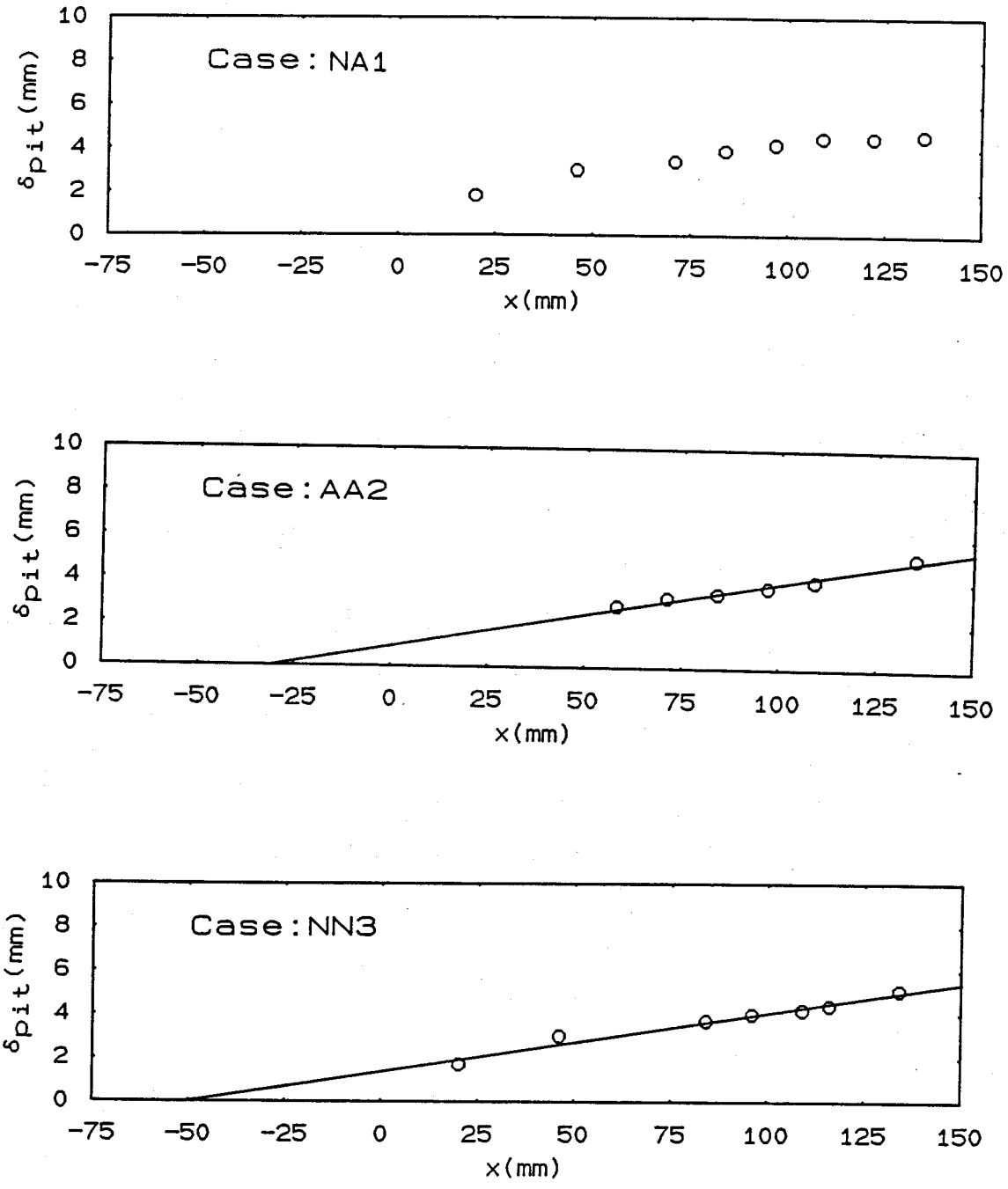


Figure 3.4 Measurements of pitot thickness with least-squares fit to data points downstream of x=75 mm.

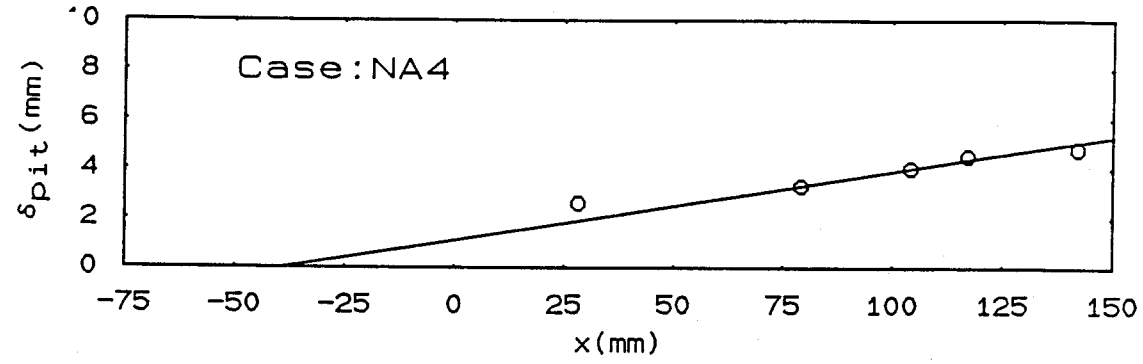


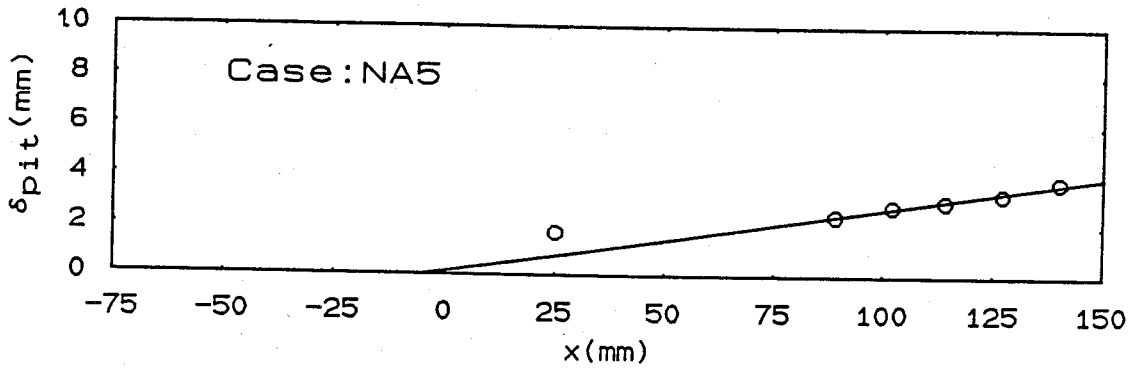


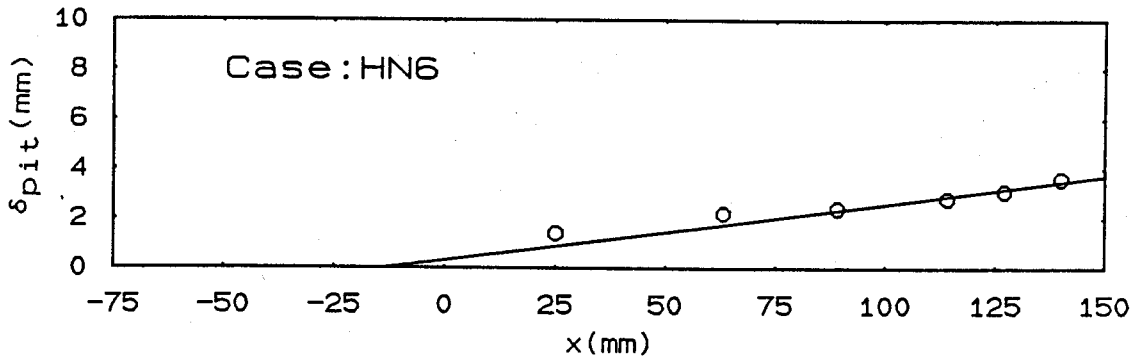


Figure 3.4 Continued.

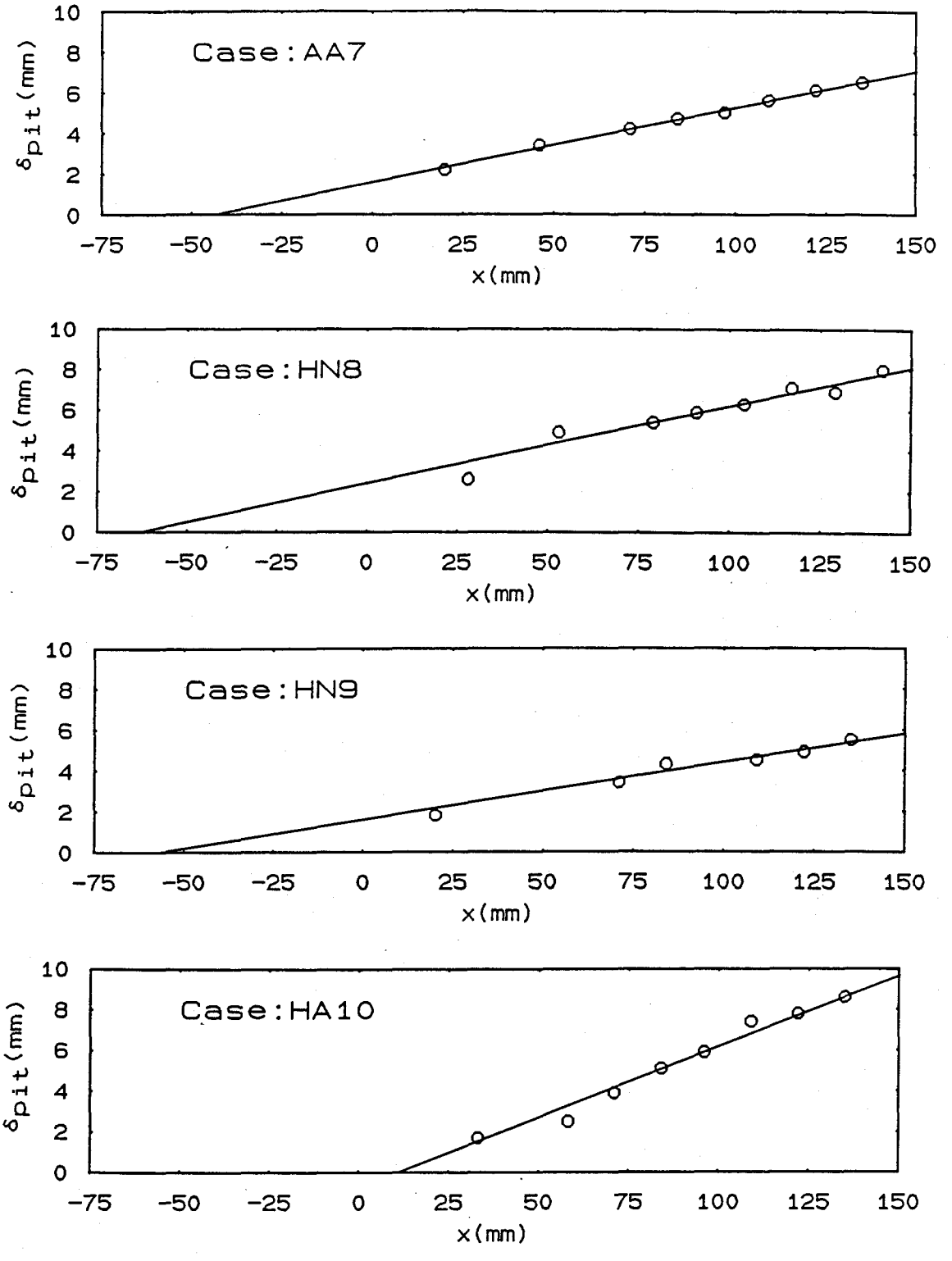


Figure 3.4 Continued.

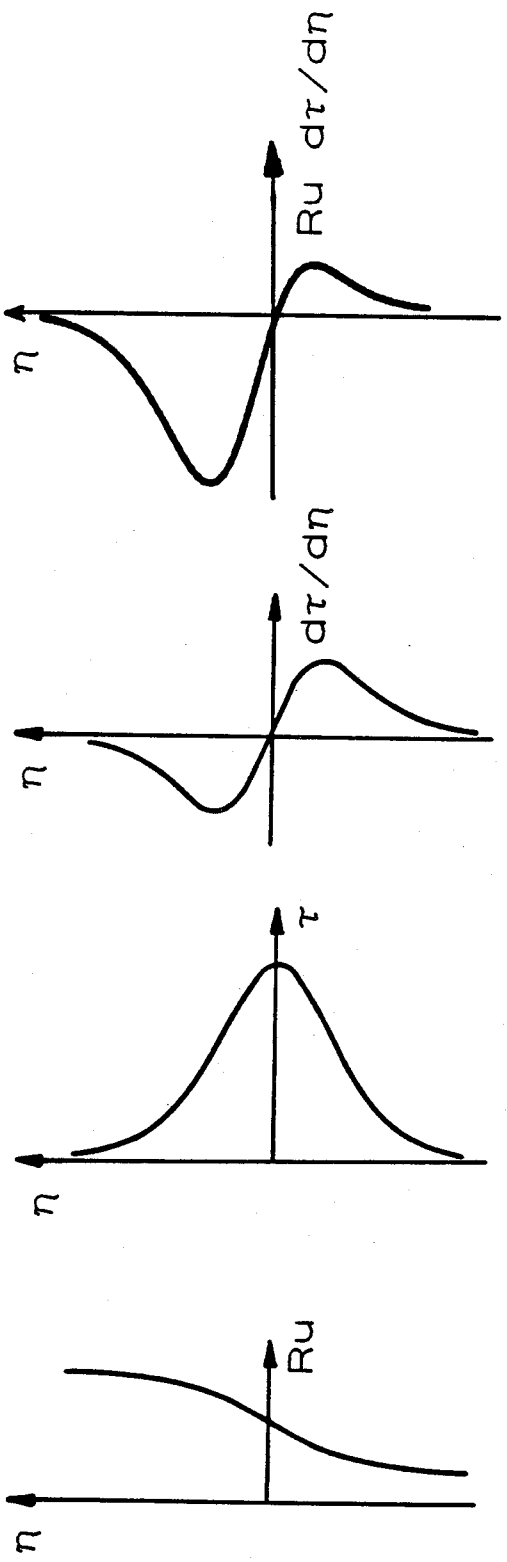


Figure 3.5 Distribution of right-hand side of (3.3)

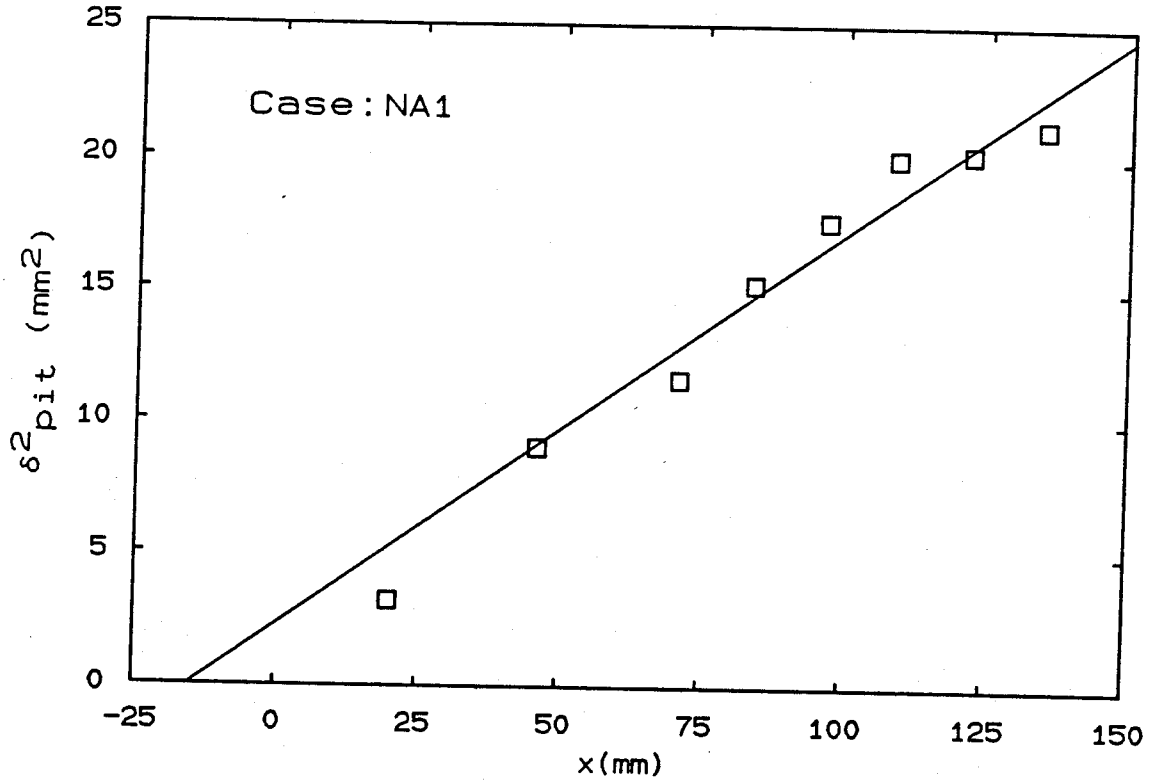


Figure 3.6 Growth of wake case.

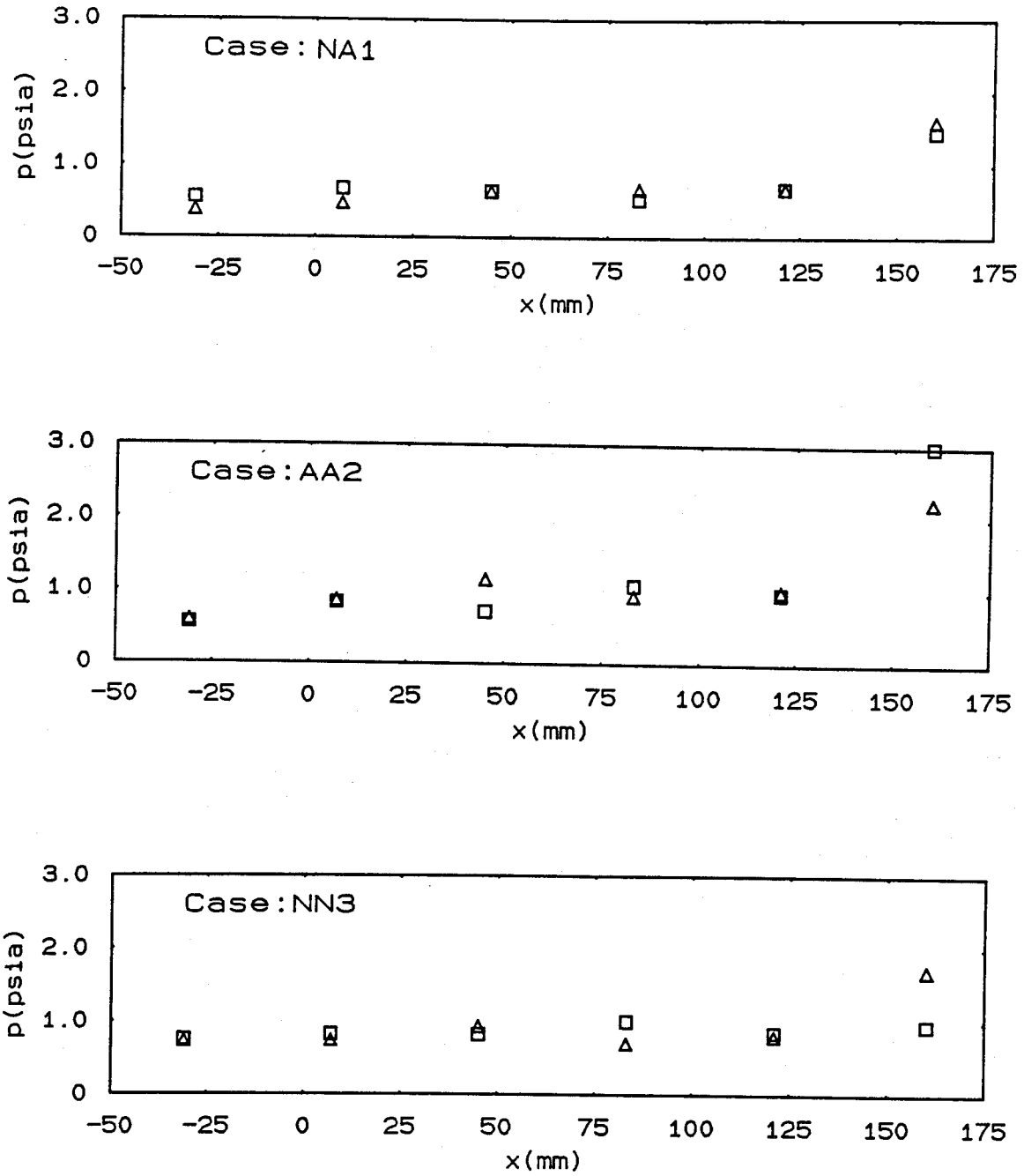


Figure 3.7 Typical sidewall static pressure measurements.
Squares: high speed side; triangles: low speed side.

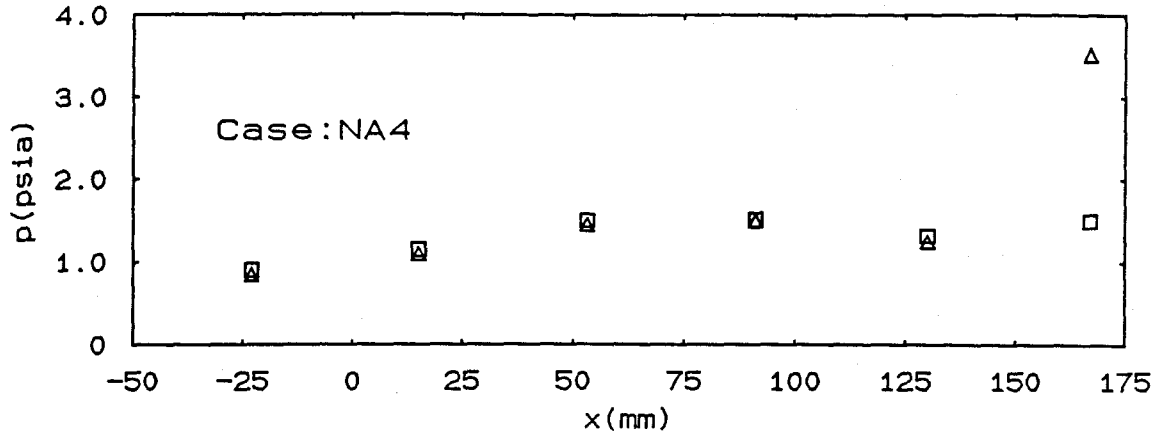


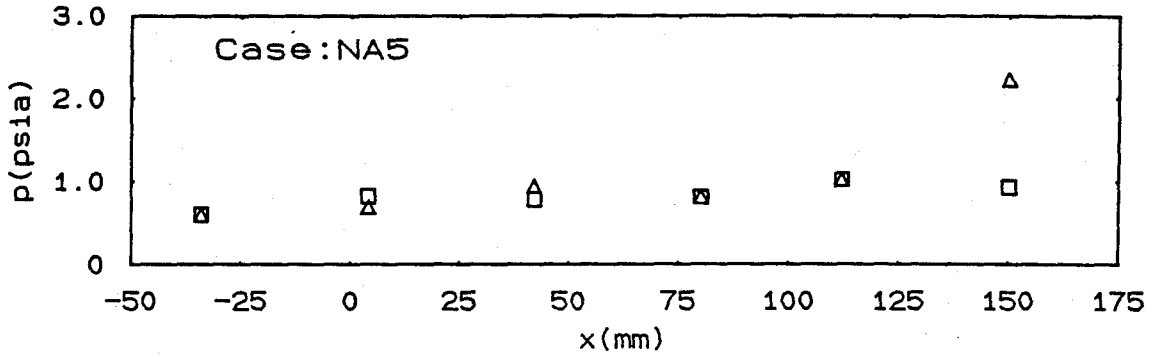


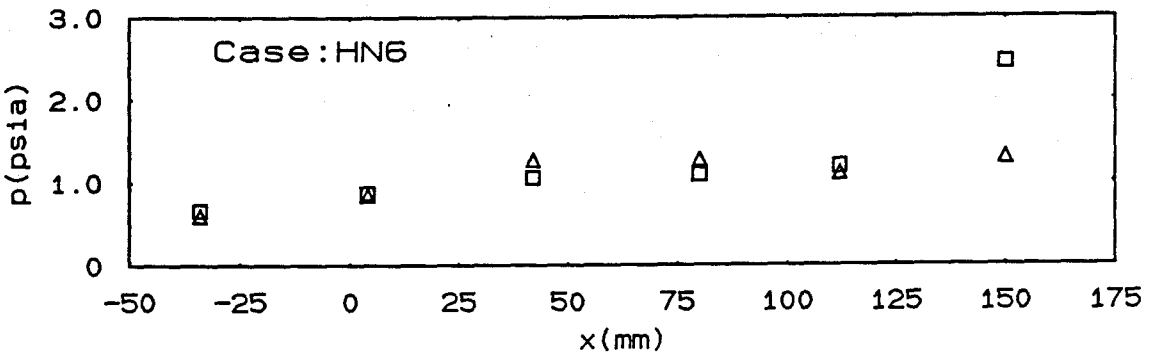


Figure 3.7 Continued.

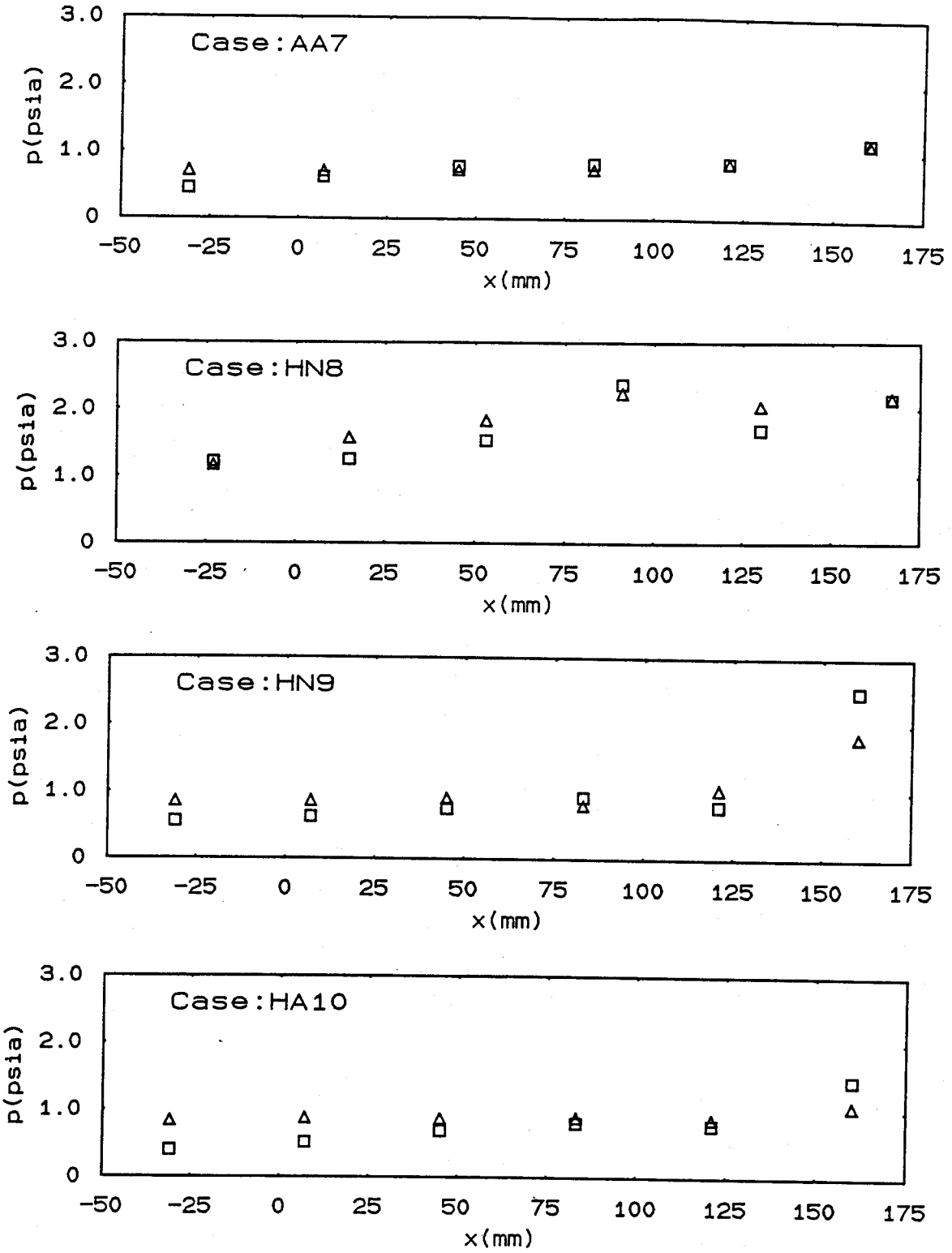


Figure 3.7 Continued.

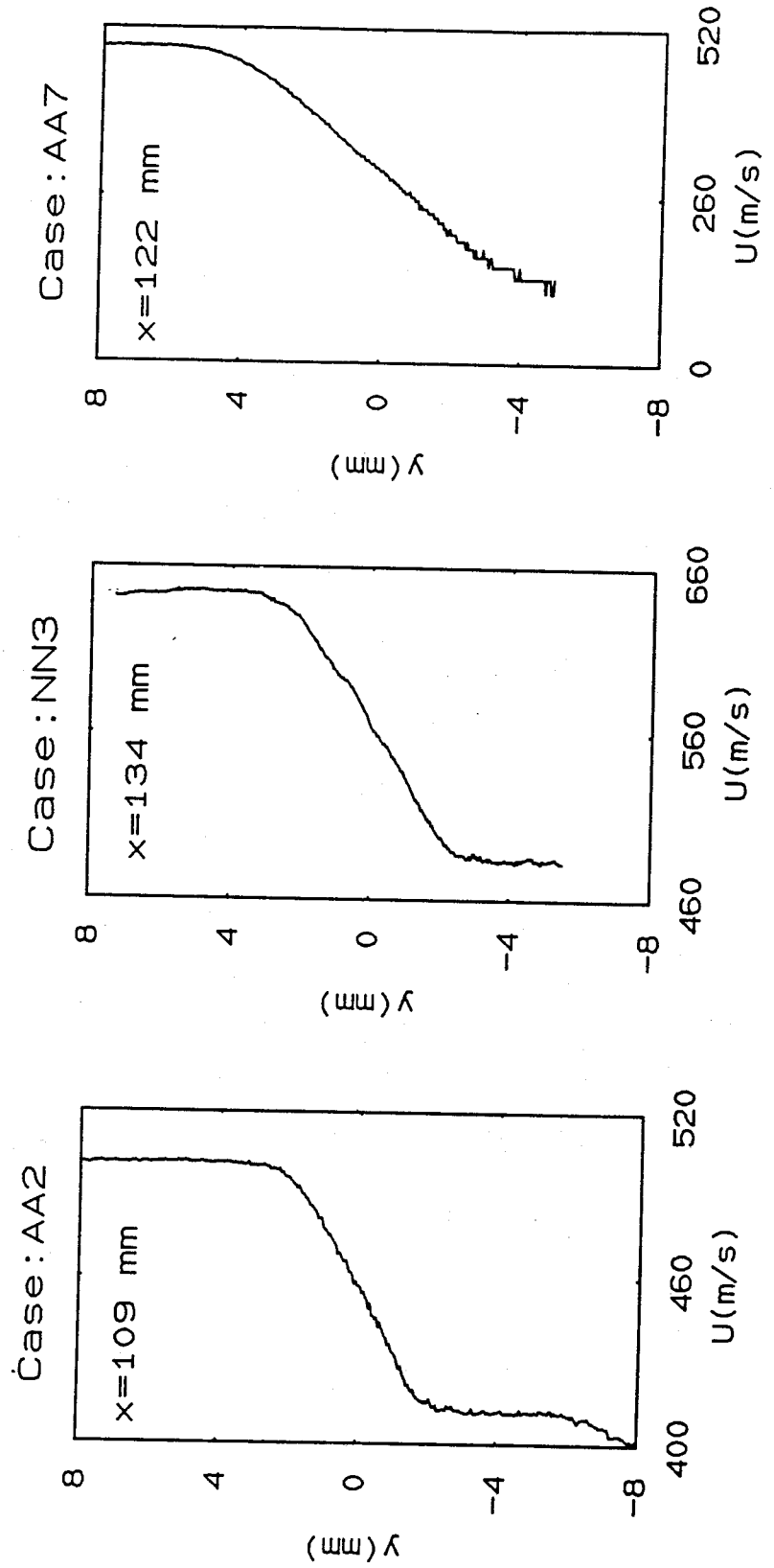


**Figure 3.8 Velocity profiles for the homogeneous cases.**

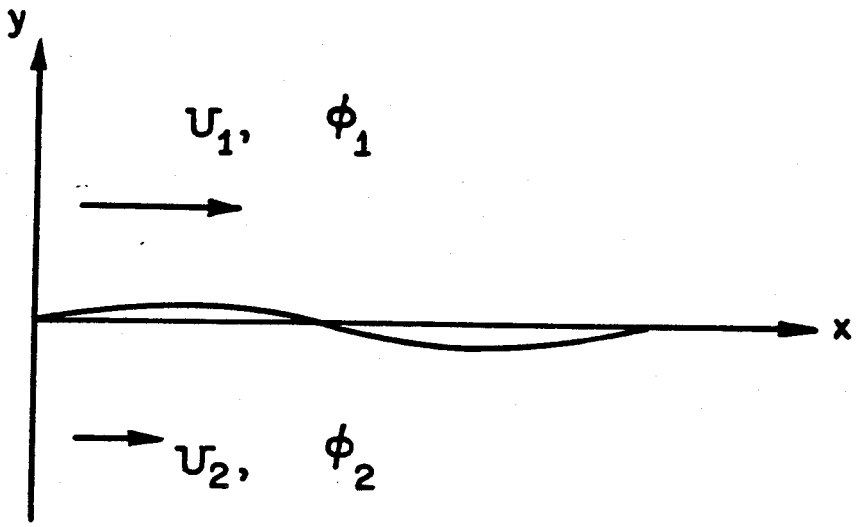


Figure 4.1 Vortex sheet in compressible fluid.

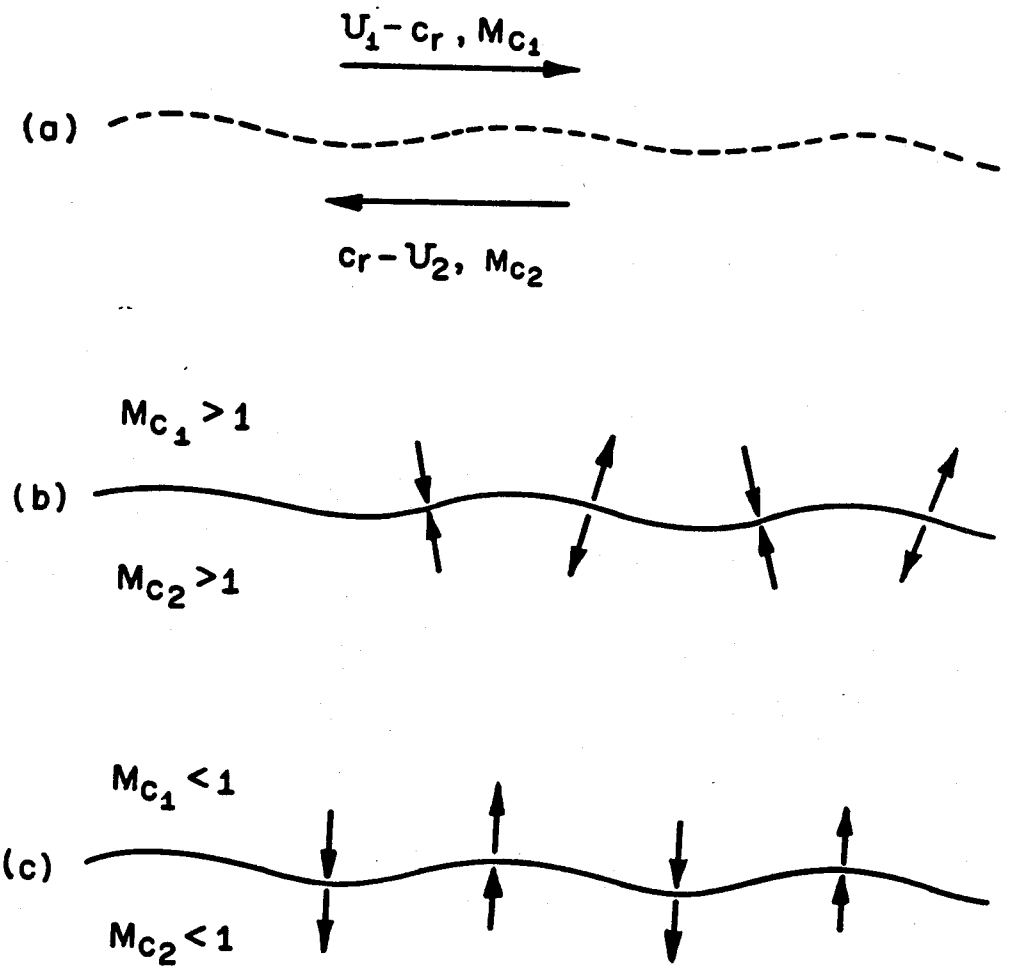


Figure 4.2 Ackeret's stability argument.

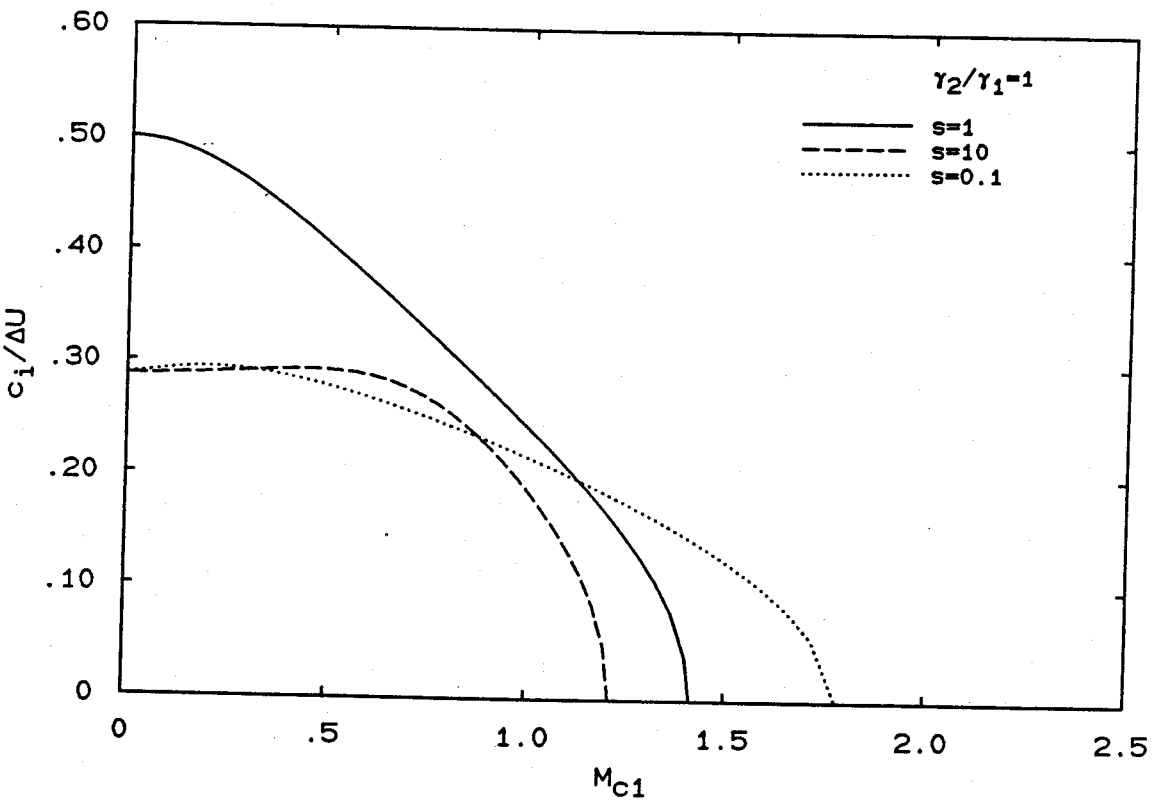


Figure 4.3 Normalized imaginary phase speed of compressible vortex sheet as a function of $M_{c_1}$ and s for $\gamma_2=\gamma_1$.

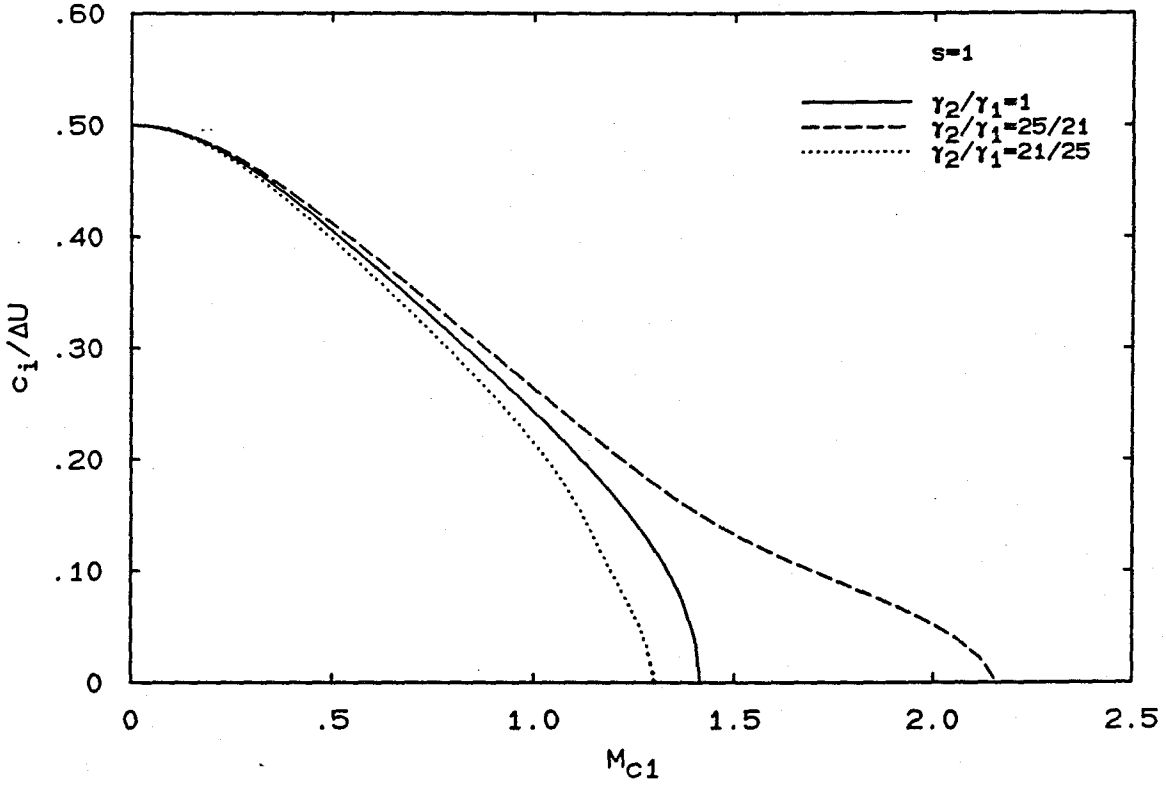


Figure 4.4 Normalized imaginary phase speed of compressible vortex sheet as a function of $M_{c_1}$ and $\gamma_2/\gamma_1$ for s=1.

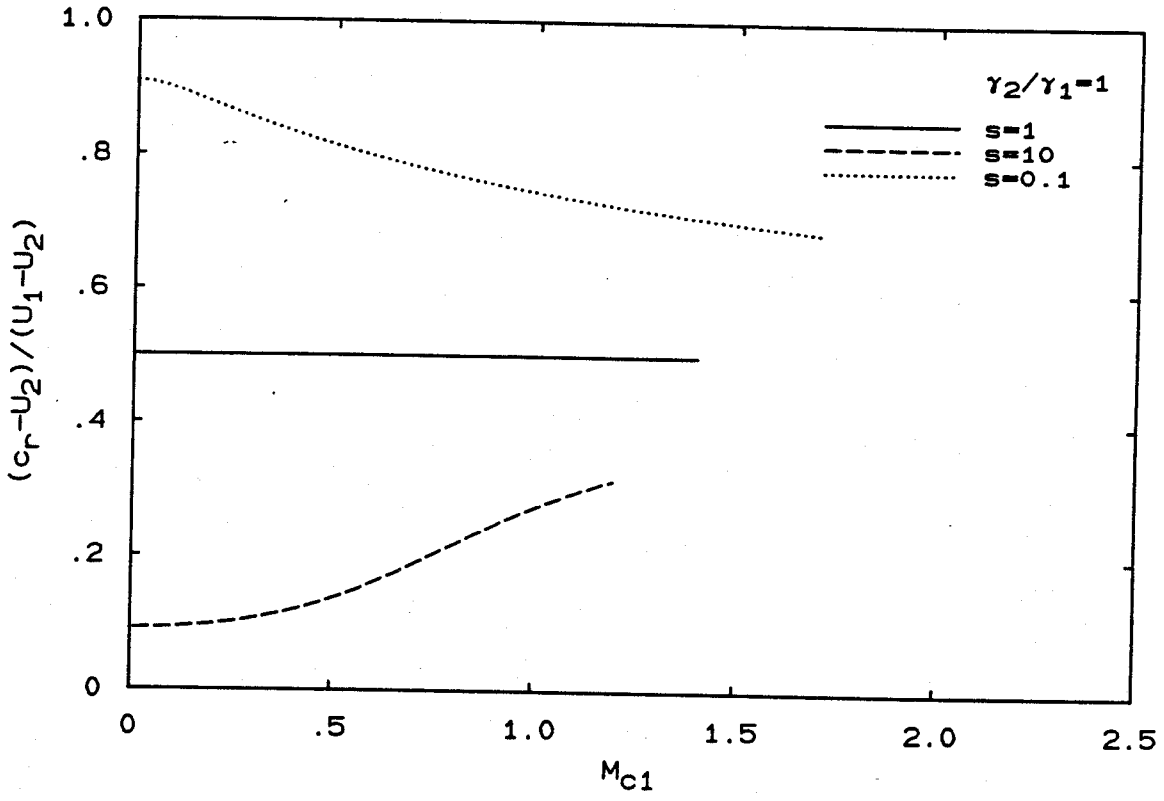


Figure 4.5 Normalized real phase speed of compressible vortex sheet as a function of $M_{c_1}$ and s for $\gamma_2=\gamma_1$.

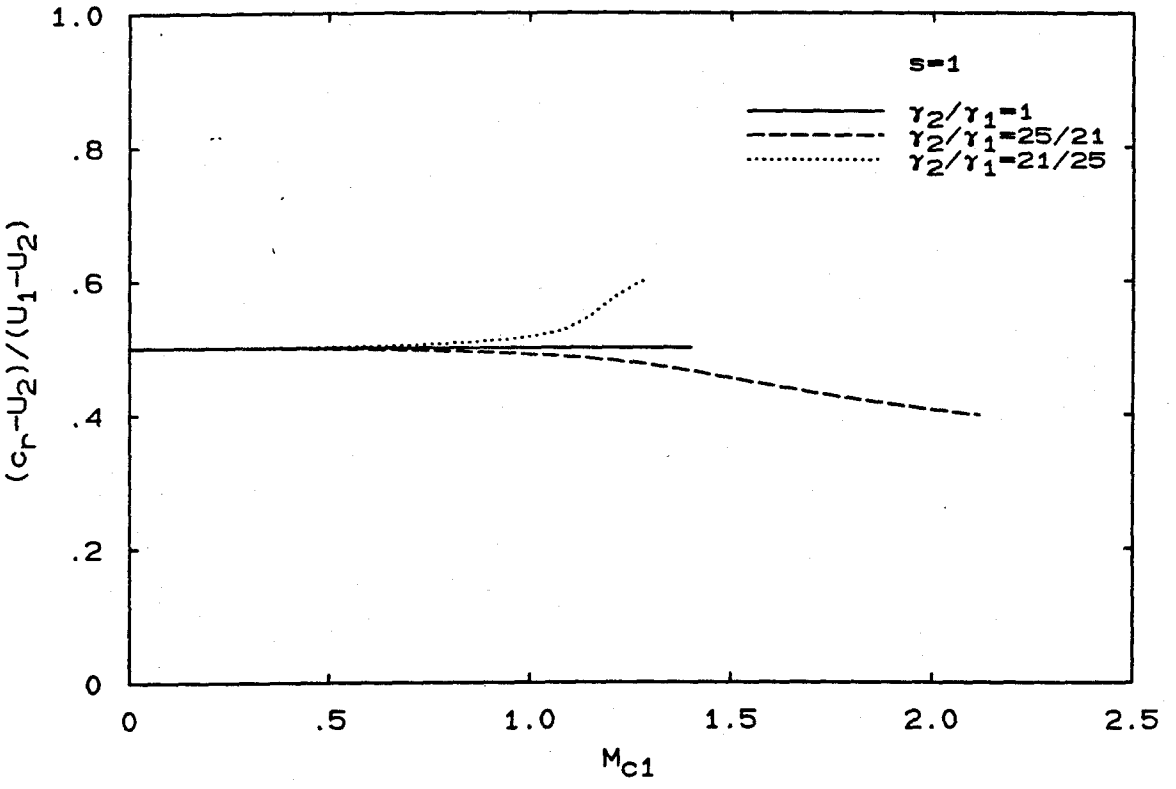


Figure 4.6 Normalized real phase speed of compressible vortex sheet as a function of $M_{c_1}$ and $\gamma_2/\gamma_1$ for s=1.

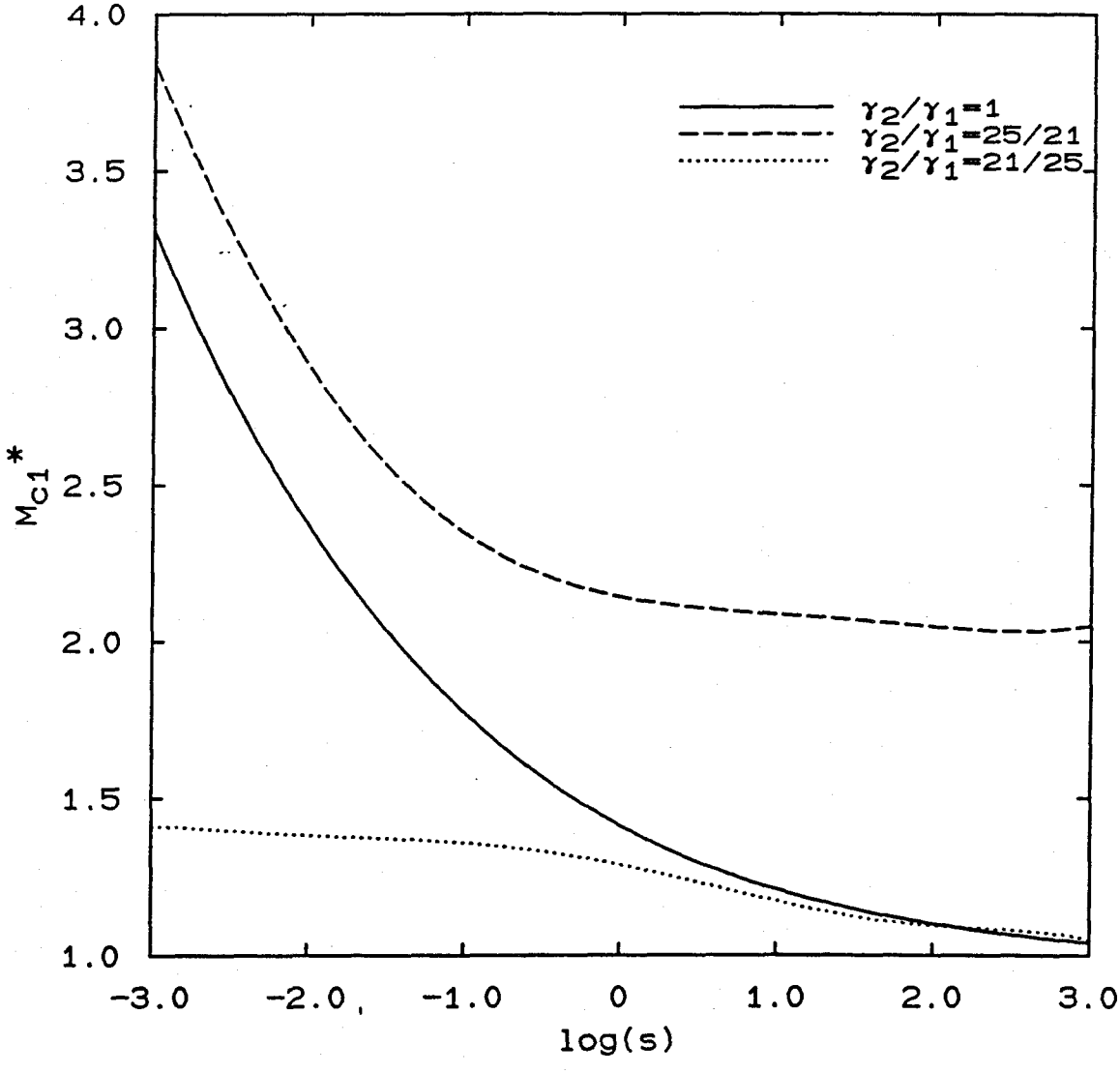


Figure 4.7 Neutral stability curves for compressible vortex sheet as a function of $M_{c_1}$, s, and $\gamma_2/\gamma_1$.

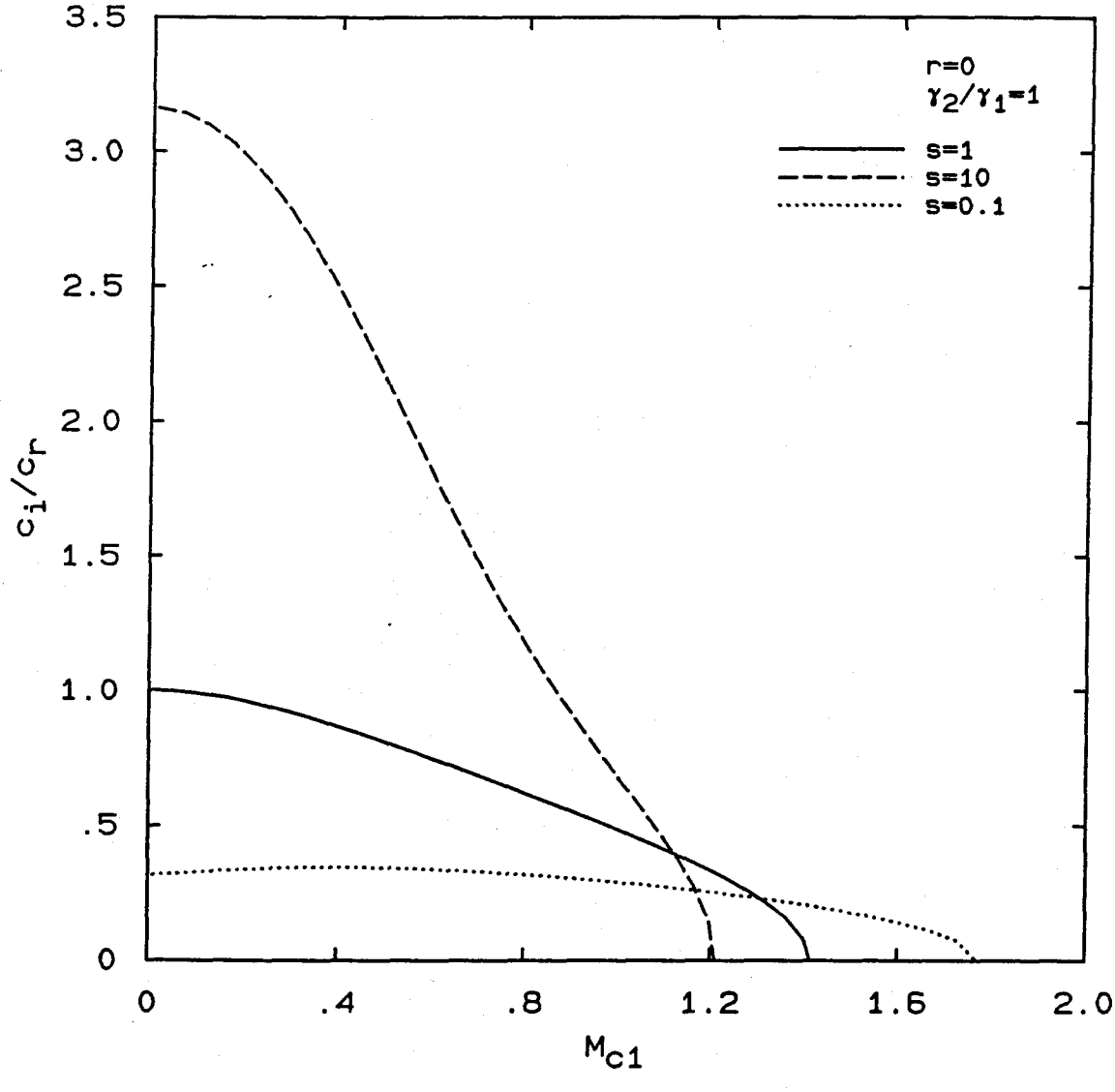


Figure 4.8 Transformed spatial amplification rate $c_i/c_r$ versus $M_{c_1}$ and s for $\gamma_2=\gamma_1$ and r=0.

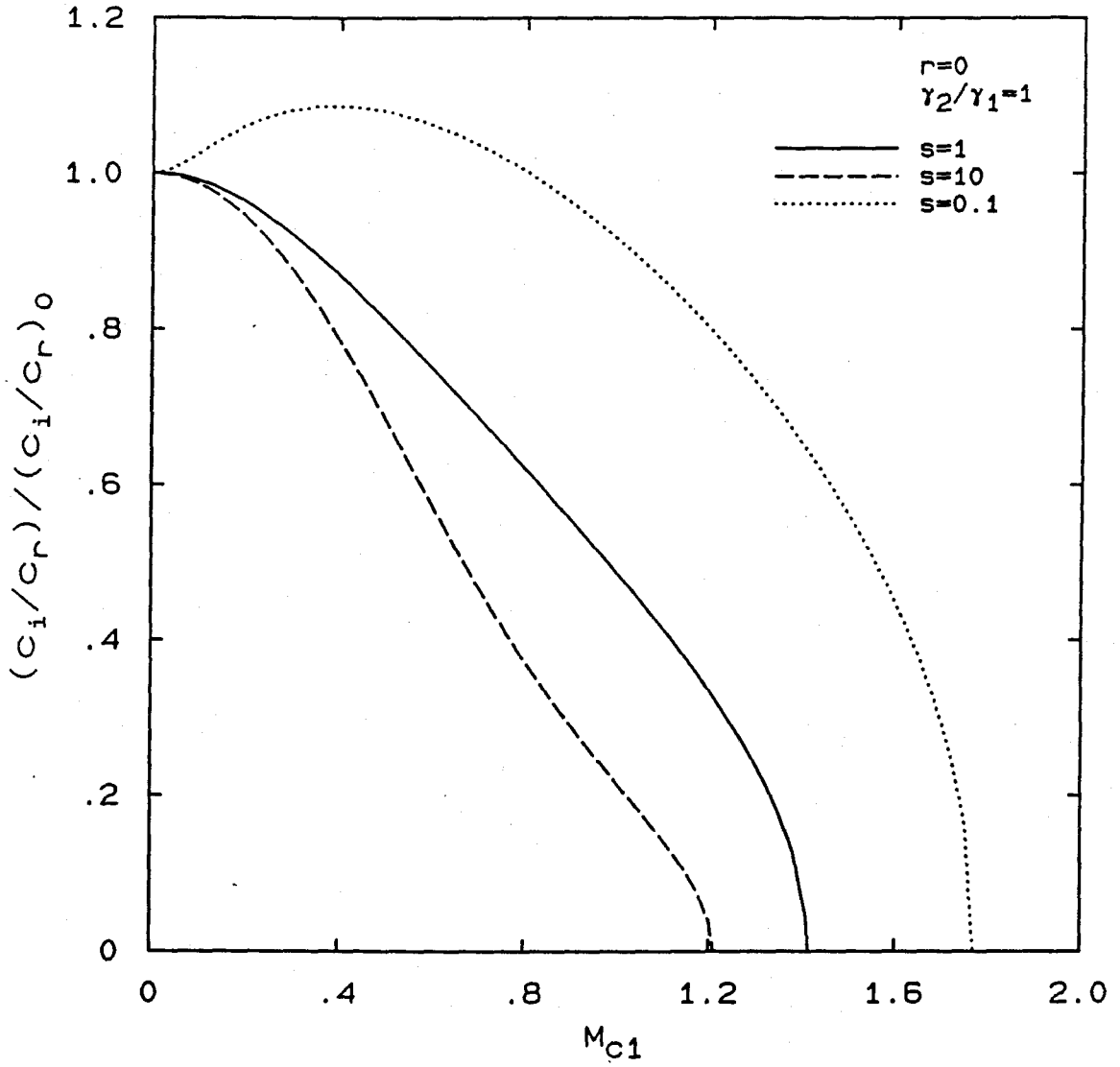


Figure 4.9 $c_i/c_r$ normalized by its value at $M_{c_1}=0$ versus $M_{c_1}$ and s for $\gamma_2=\gamma_1$ and r=0.

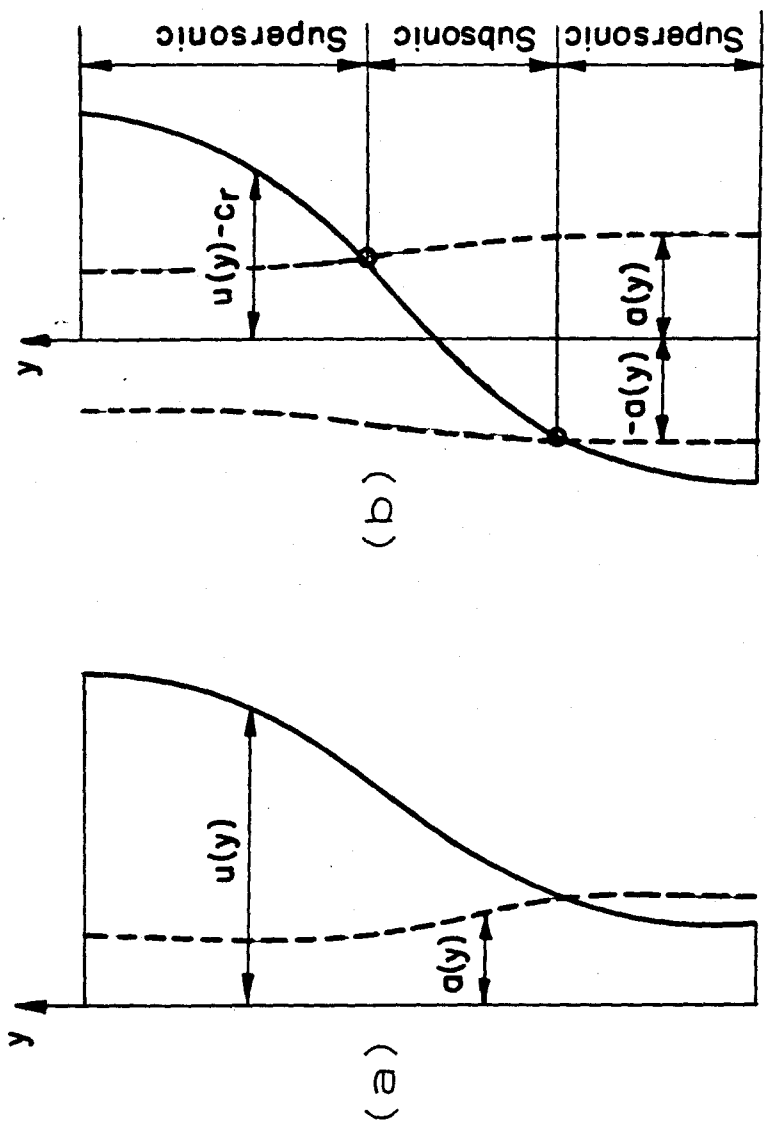


Figure 4.10 Disturbance classification in compressible shear layer,
(a) Stationary frame of reference,
(b) Frame of reference convecting with $c_r$.

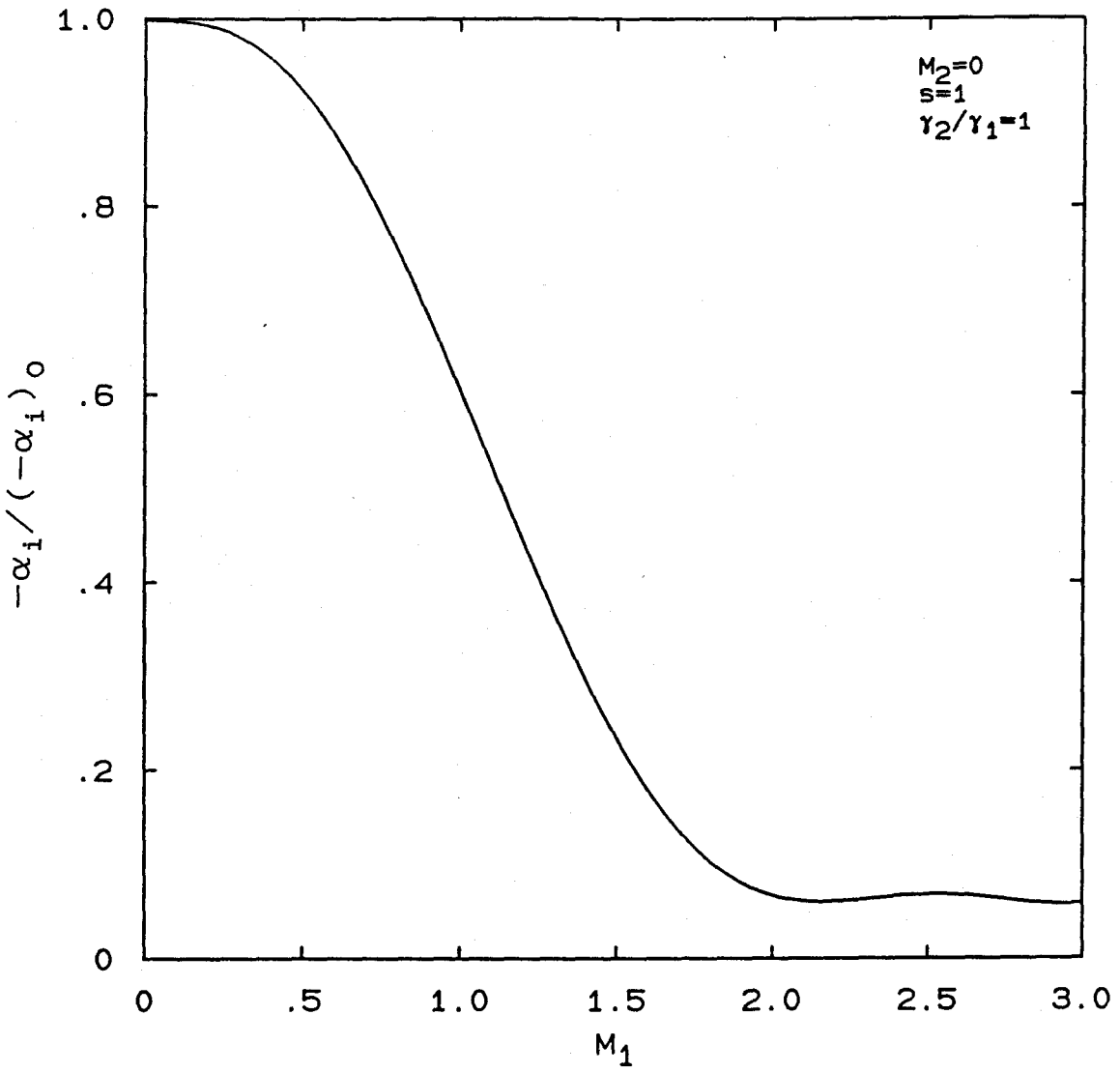


Figure 4.11 Maximum amplification rate for a compressible shear layer with a Lock velocity profile, as computed by Gropengiesser [1969].

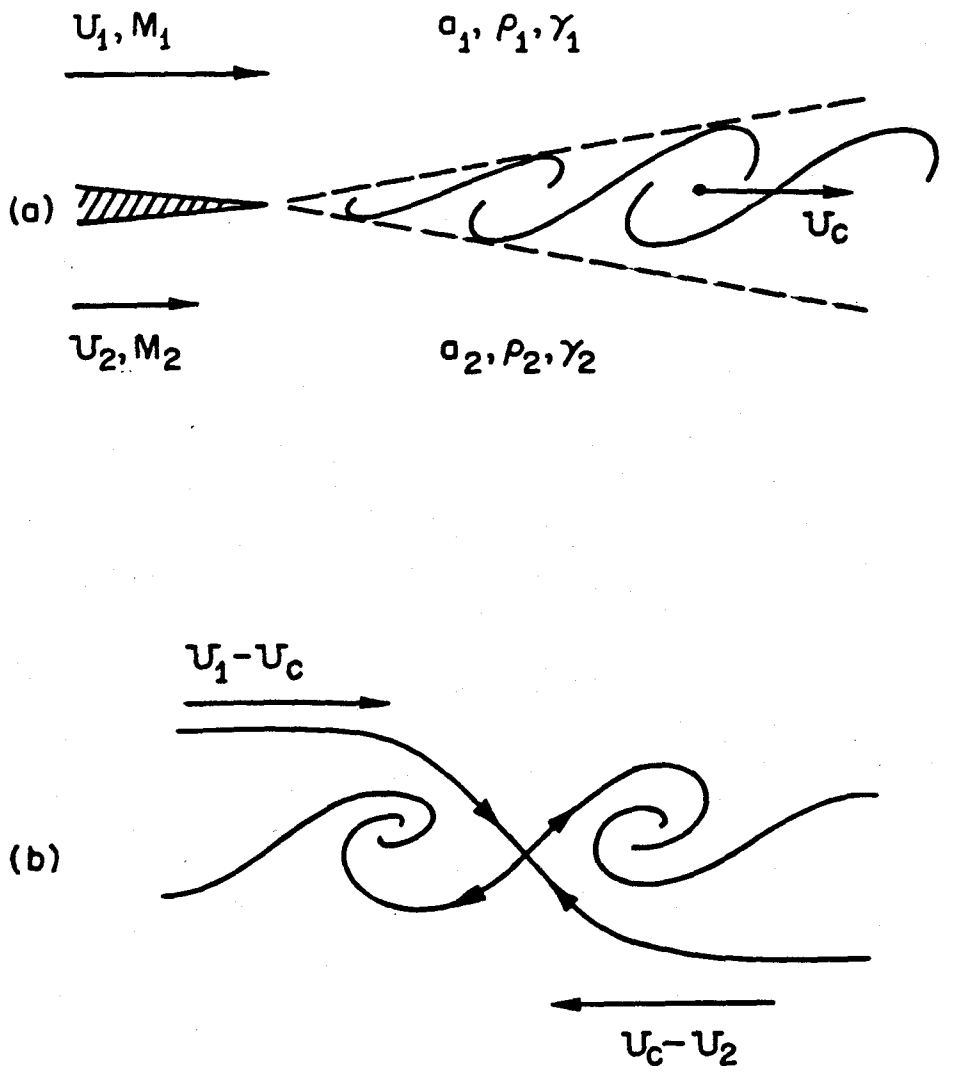


Figure 4.12 Turbulent shear layer,
(a) Stationary frame of reference,
(b) Convective frame of reference with sketches of streamlines after Coles [1981].

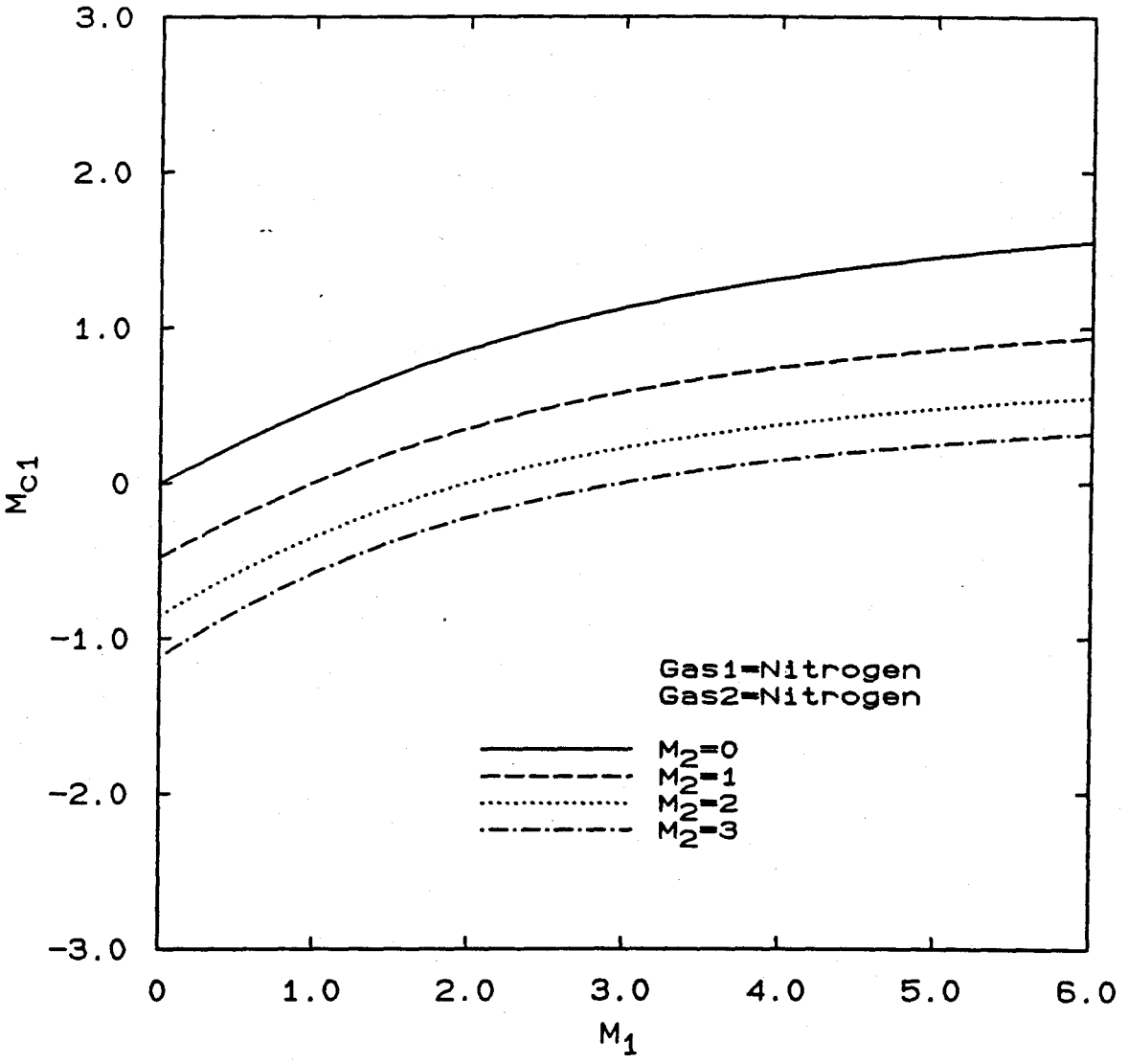


Figure 4.13 Convective Mach number $M_{c_1}$ as a function of $M_1$ and $M_2$ for various gas combinations assuming uniform total temperature.

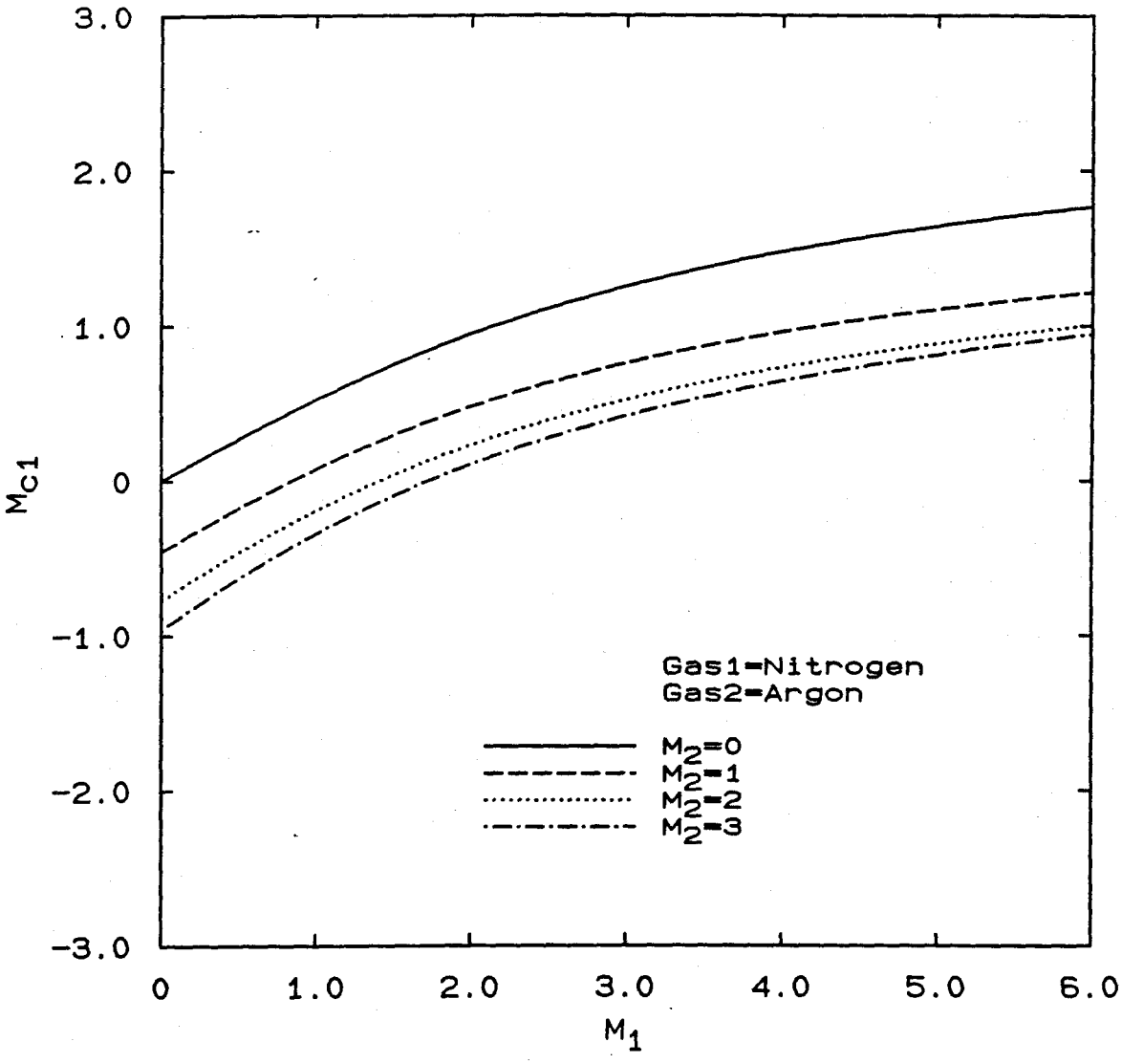


Figure 4.13 Continued.

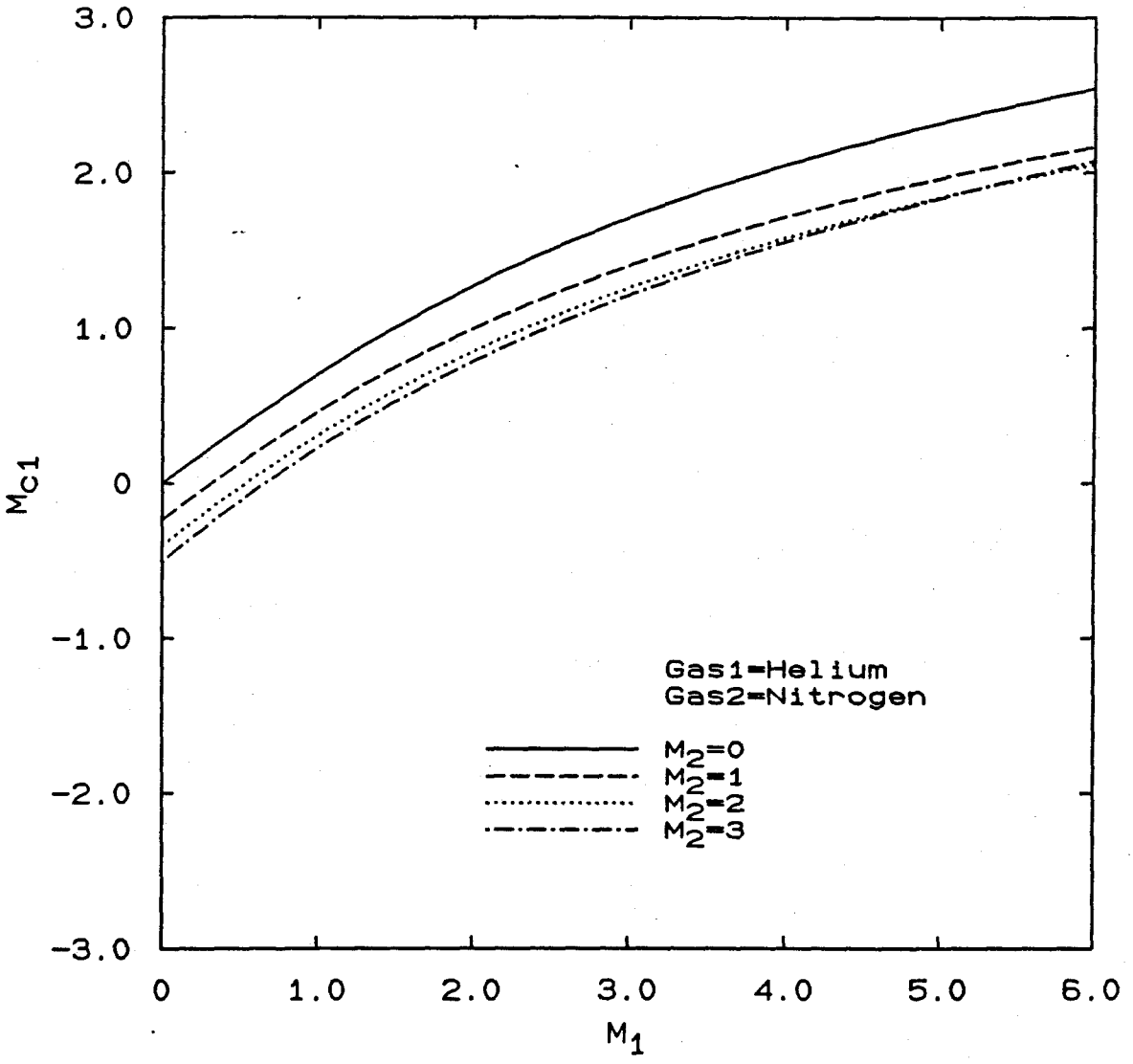


Figure 4.13 Continued.

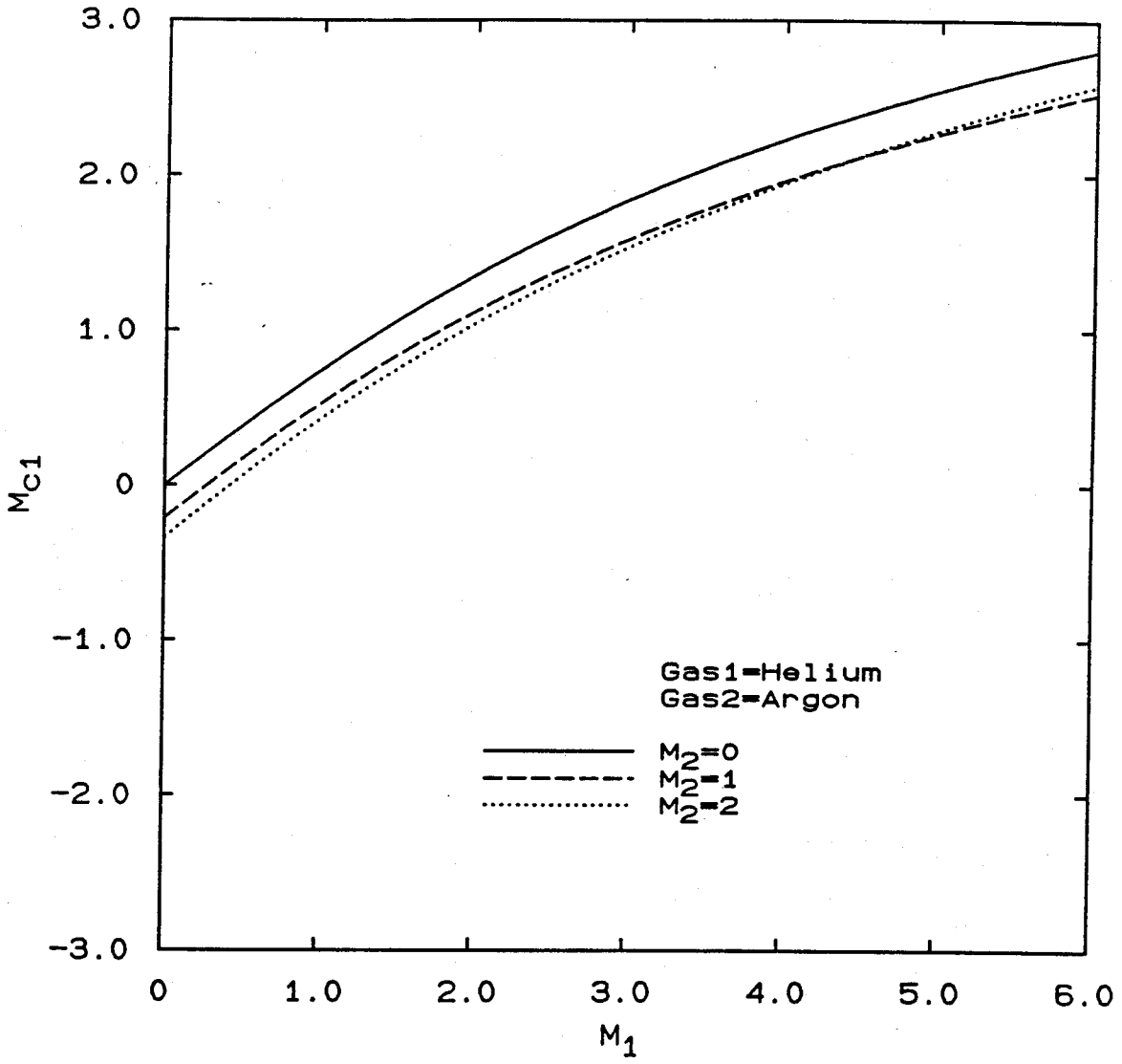


Figure 4.13 Continued.

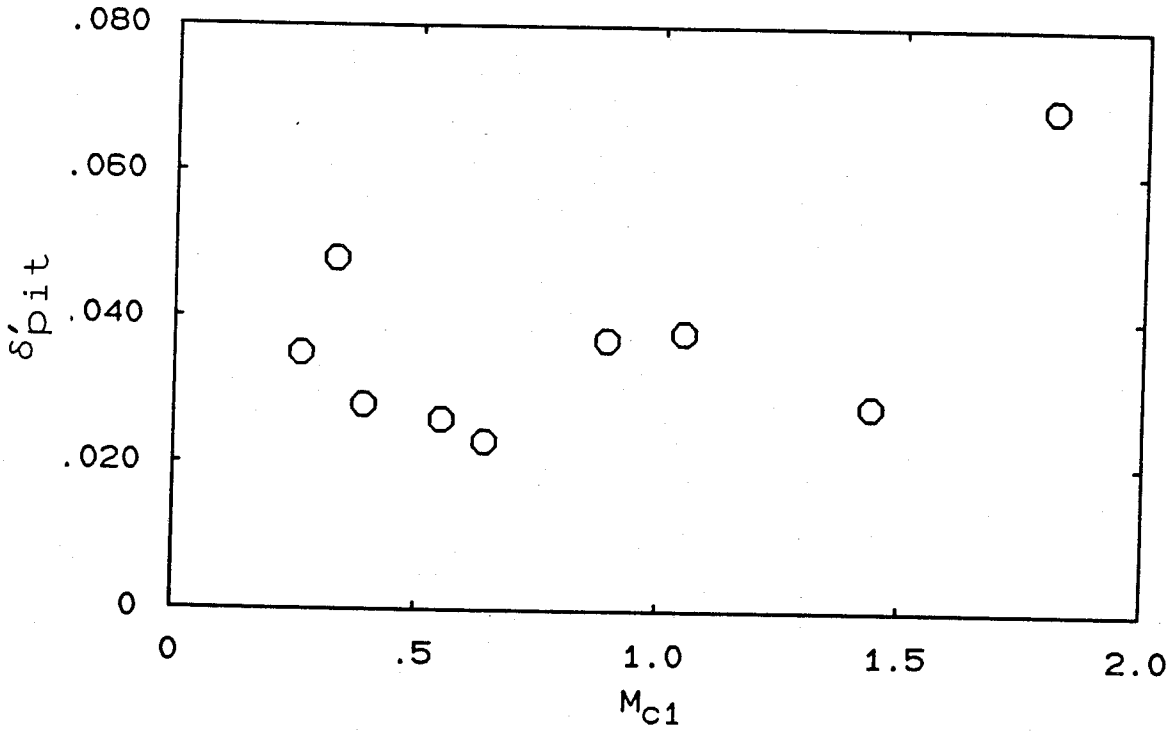


Figure 5.1 Pitot thickness growth rate versus $M_{c_1}$.

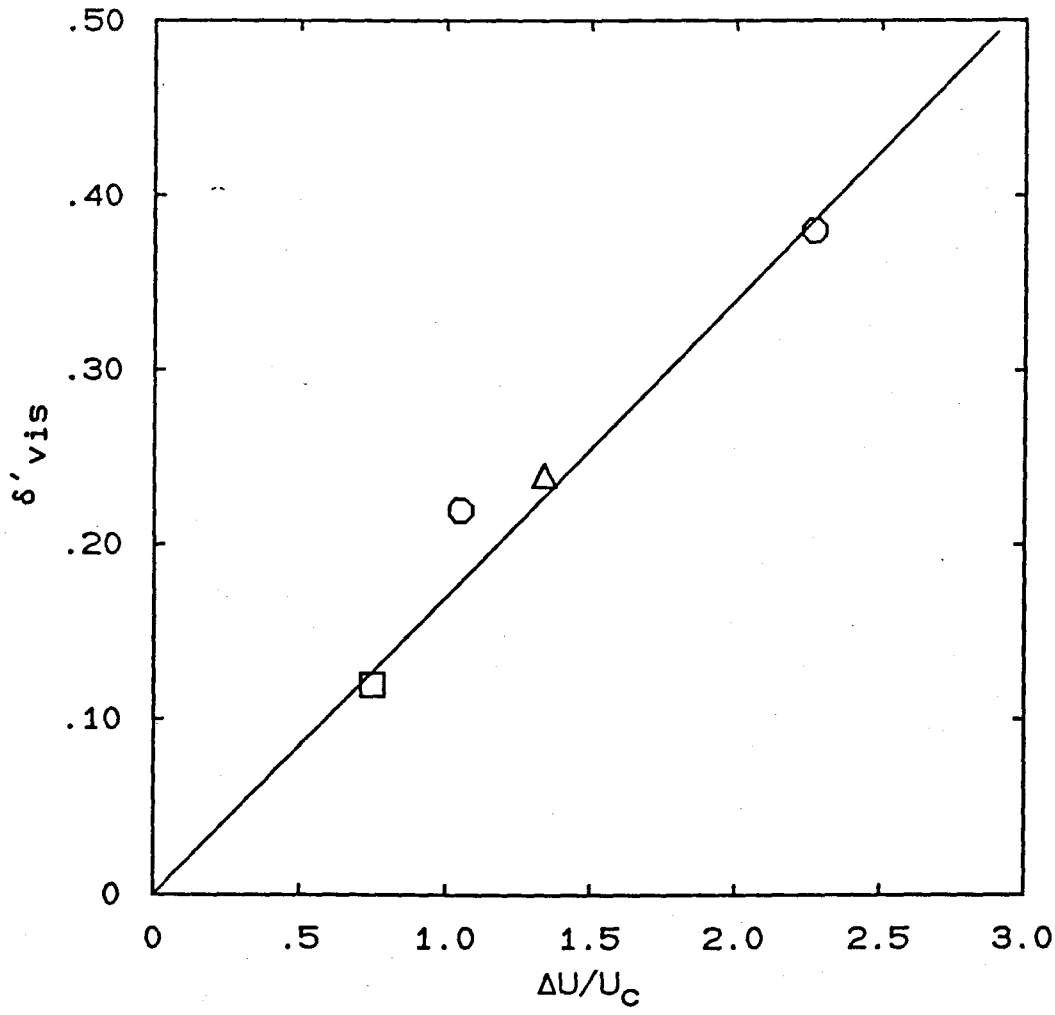


Figure 5.2 Model for visual growth of incompressible shear layer. Circle and square data points from Brown and Roshko [1974] for s=7 and s=1/7 respectivelly, triangle from Dimotakis and Brown [1976] for s=1.

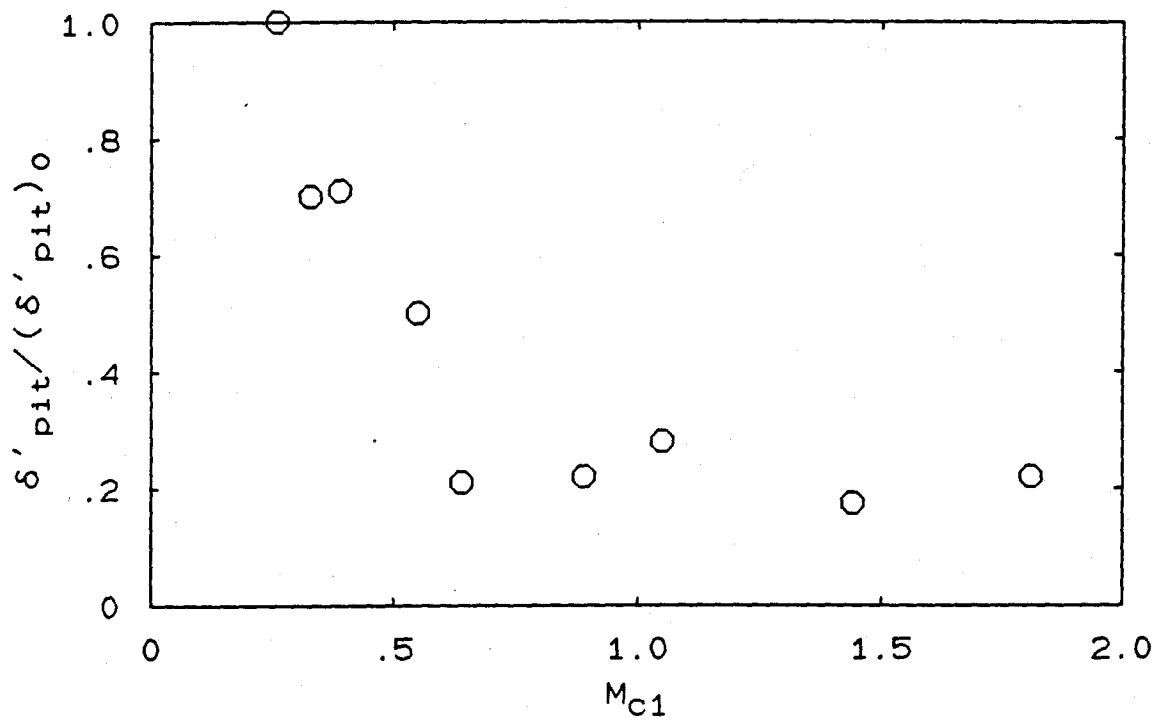


Figure 5.3 Normalized pitot thickness growth versus $M_{c_1}$.

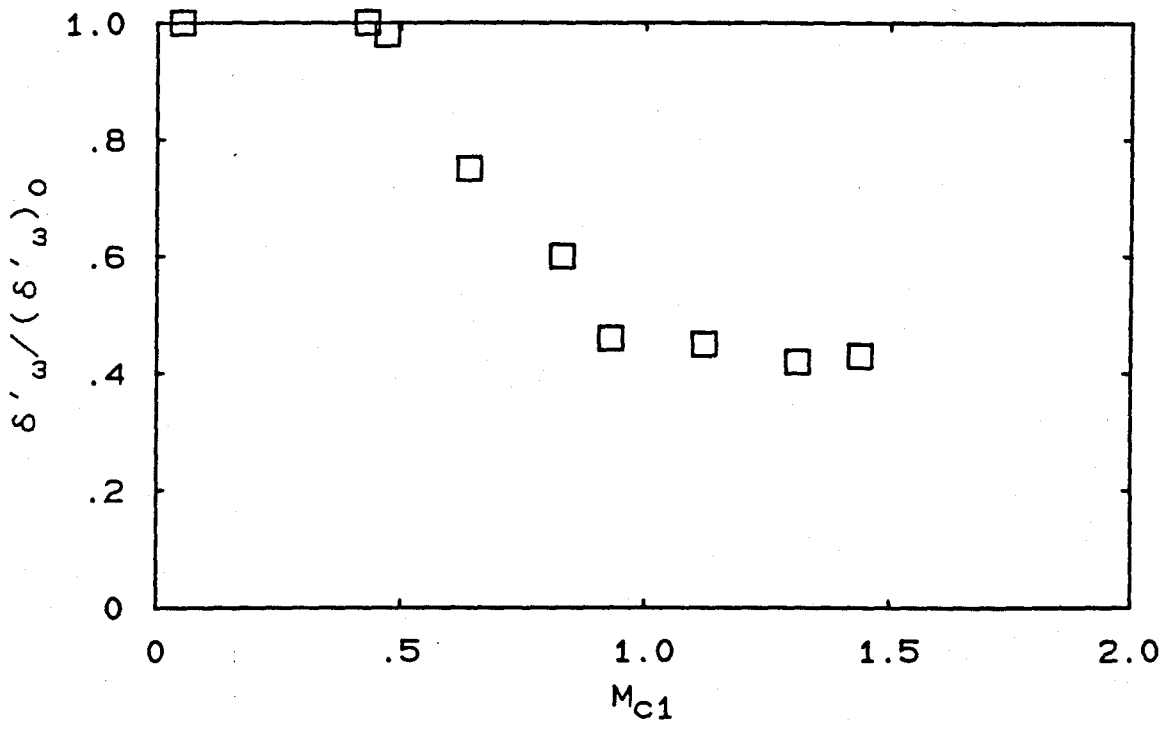


Figure 5.4 Normalized vorticity thickness growth versus $M_{c_1}$. Original data obtained by other investigators as compiled in Fig.1 of Bogdanoff [1982].

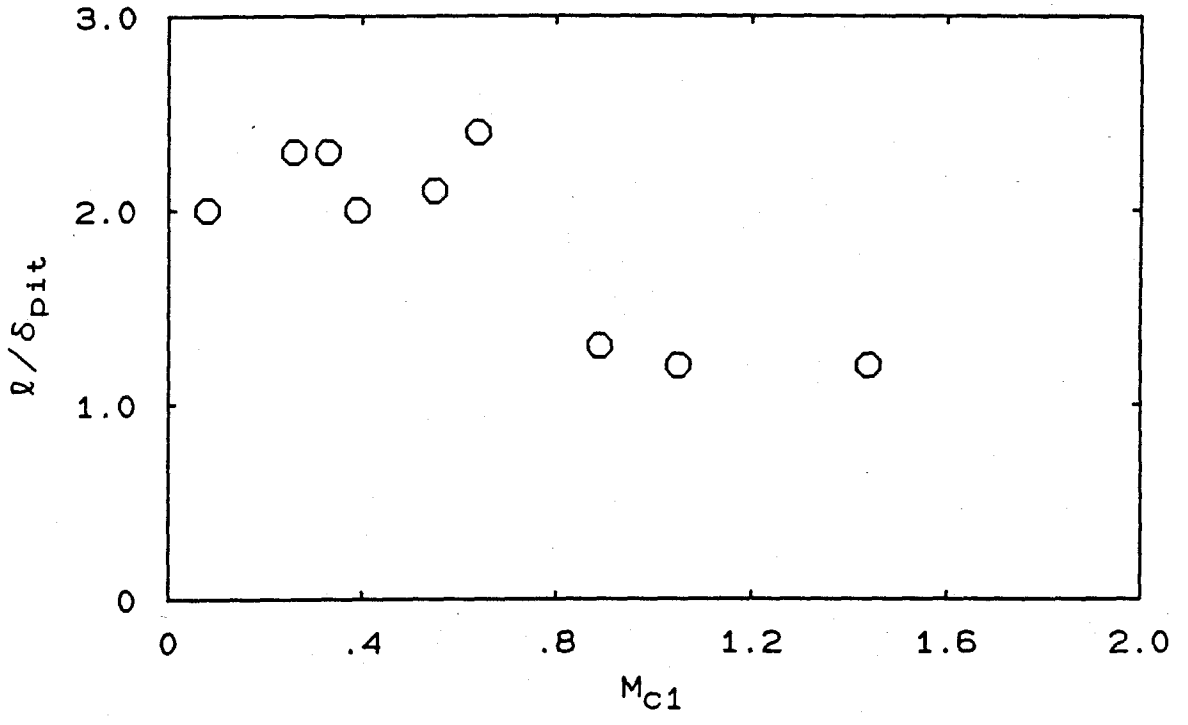


Figure 5.5 Structure spacing normalized by pitot thickness versus $M_{c_1}$.

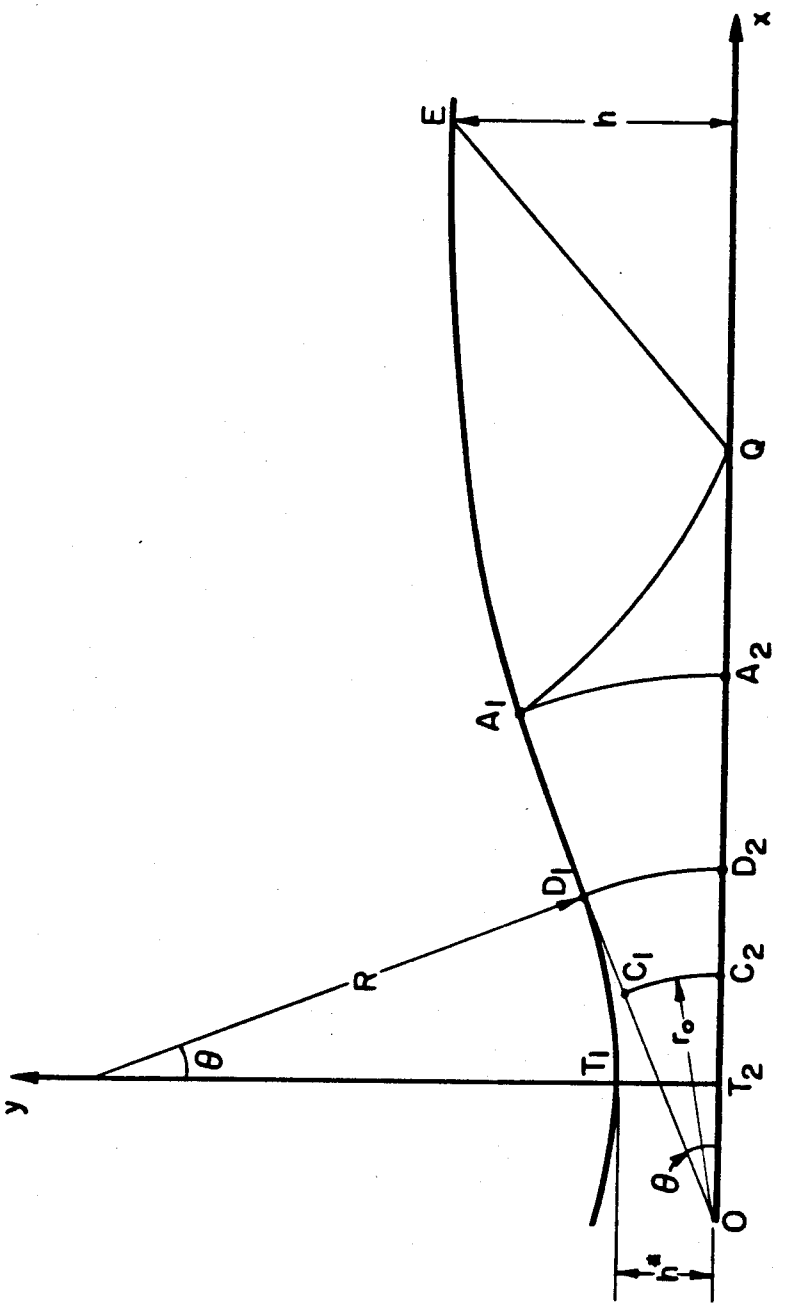


Figure A.1 Foelsch nozzle design.